

國立交通大學

材料科學與工程學系

博士論文

中孔洞材料在二氧化碳捕獲與藥物釋放之研究

Mesoporous Materials on CO₂ Capture and Drug Delivery

研究生：張彥博

指導教授：陳三元 博士

中華民國一零一年七月

中孔洞材料在二氧化碳捕獲與藥物釋放之研究

Mesoporous Materials on CO₂ Capture and Drug Delivery

博士生：張彥博

Student : Yen-Po Chang

指導教授：陳三元博士

Advisor : Dr. San-Yuan Chen

國立交通大學

材料科學與工程研究所

博士論文

A Thesis

Submitted to Department of Materials Science and Engineering

College of Engineering

National Chiao Tung University

In partial Fulfillment of the Requirements

For the Degree of

Doctor of Philosophy

in

Materials Science and Engineering

July 2012

Hsinchu, Taiwan, Republic of China

中華民國一零一年七月

中文摘要

本論文中，使用各種不同的合成技術，其中包括溶膠-凝膠法、水熱尿素反應、微波輔助合成法以及固態反應開發出多功能性中孔洞奈米結構材料 (CaO/CaAlO, $C_{12}Al_{14}O_{33}$, Gd_2O_3 , TiO_2)。使用粉末 X 光繞射儀(PXRD)、穿透式電子顯微鏡/電子能量損失光譜 (TEM/EELS)、掃描式電子顯微鏡/X 光能量分散光譜儀(SEM/EDS)、傅氏轉換紅外線光譜(FTIR)、氮氣吸附等溫線(N_2 adsorption isotherm) 詳細地鑑定這些材料的組成、形貌、化學結構以及多孔結構。這些中孔洞奈米結構材料的合成機制將於各章節中被討論。本研究的中孔洞材料的孔徑大小為 2-50 奈米範圍內。由於它們具有高表面積與奈米孔洞結構的諸多優點，在二氧化碳捕獲與藥物釋放領域分別可以被設計為一種高溫吸附劑或藥物載體。

在先期研究發現 (如附錄-1)，首先採用水熱共沉法合成出二種不同金屬混合之金屬氧化物(MgAlO、CaAlO、SrAlO)，並且在高溫(200-850 °C)二氧化碳補捉實驗證實，CaAlO 金屬氧化物最適合作為高溫二氧化碳吸附劑(600-700 °C)。因此，使用水熱尿素法來合成中孔洞金屬氧化物(CaO/CaAlO)，此材料具有高表面積、均一孔洞結構及均勻的奈米氧化鈣分佈，經由熱重分析(TGA)或固定床反應器(fixed-bed reactor)同時進行二氧化碳補捉實驗，結果證實中孔洞奈米材料具有高二氧化碳吸附容量，快速吸附性和長循環壽命。更進一步，使用微波輔助合成法進行中孔洞 CaAlO 金屬氧化物合成，由粉末 X 光繞射與電子顯微鏡證明，在低於 600 °C 的固態反應後可以形成結晶性 $C_{12}Al_{14}O_{33}$ 奈米棒成長在奈米孔洞 CaAlO 基質表面上。此材料具有多孔結構與高熱穩定性，未來可以作為催化劑或二氧化碳吸附劑之載體。

另外，本研究採用溶膠-凝膠法合成出中孔洞氧化釷(Gd_2O_3)奈米管及中孔洞二氧化鈦(TiO_2)奈米薄膜，兩者材料可作為藥物載體並使用於藥物釋放控制。此材料鑑定具有高表面積、多孔洞結構與高結晶性的奈米骨架。中孔洞氧化釷奈米管表現出微弱的超順磁特性，能夠攜帶布洛芬(IBU)藥物，並且通過外部磁場控制方式進行藥物釋放。另外，二氧化鈦薄膜具有蠕蟲狀中孔洞結構，使用布洛芬(IBU)和萬古黴素(VAN)

作為藥物模型分子，測定與薄膜化學相關持續藥物釋放。除此之外，體外骨細胞的黏附行為和氫氧基磷灰石形成，證明此薄膜也具有細胞相容性和生物活性表現。



Abstract

In this dissertation, multi-functionalized mesoporous nanostructured materials (such as CaO/CaAlO, $C_{12}Al_{14}O_{33}$, Gd_2O_3 , and TiO_2) have been prepared through various synthesized routes, which include sol-gel method, hydrothermal urea reaction, microwave-assisted synthesis, and solid-state reaction. The composition, morphology, chemical structure, and porous structure of these materials were identified in detail using powder X-ray diffraction (PXRD), transmission electron microscopy/electron energy loss spectroscopy (TEM/EELS), scanning electron microscopy/energy-dispersive X-ray spectroscopy (SEM/EDS), Fourier transform infrared spectroscopy (FTIR), and N_2 -adsorption isotherm. The synthesized mechanisms of these materials are discussed in respective chapter. In this study, the obtained mesoporous materials exhibit pore diameter in the range of 2-50 nm. Due to many advantages of its high surface area and nanopores structure, these mesoporous nanostructured materials can be designed as high-temperature CO_2 sorbents and drug carriers in the fields of carbon dioxide capture and drug delivery, respectively.

A preliminary study (see Appendix-1) can be found that hydrothermal coprecipitation method was first used to synthesize the metal oxide compounds ($MgAlO$, $CaAlO$, and $SrAlO$), and experiments for carbon dioxide capture at high temperatures (200-850 °C) have proved that the $CaAlO$ metal oxide is the most suitable as a high-temperature carbon dioxide sorbent (600-700 °C). Therefore, mesoporous metal oxides ($CaO/CaAlO$) were prepared by a hydrothermal urea method and this material demonstrates high surface area and uniform pore structure and nano-sized calcium oxide distribution. The results of carbon dioxide capture experiment by thermal gravimetric analysis (TGA) or fixed-bed reactor show that mesoporous nanomaterials has high carbon dioxide adsorption capacity, fast adsorption and long cycle life. Furthermore, the use of microwave-assisted synthesis to synthesize mesoporous $CaAlO$ metal oxides, which can be identified by powder X-ray

diffraction and electron microscopy. The results showed that the growth of the crystalline $C_{12}Al_{14}O_{33}$ nanorods on the surface of nanoporous CaAlO matrix can be formed in the solid-state reaction of less than 600 °C. In the future, this material with pore structure and high thermal stability can be used as a support for the catalyst or CO_2 sorbent.

In addition, the study is also focused on the mesoporous gadolinium oxide (Gd_2O_3) nanotubes or mesoporous titanium dioxide (TiO_2) nano-thin film, which was fabricated by the sol-gel routes, both materials can be used as a drug carrier for controlled drug release. The characterization of the material in this study has been identified to exhibit a high surface area, porous structure and high crystalline nano-frameworks. Mesoporous Gd_2O_3 nanotubes exhibited weak superparamagnetic property and was found to be able to carry and elute a model molecule, i.e. ibuprofen (IBU), in a controllable manner via an external magnetic field. Further, the worm-like mesoporous architecture associated with the chemistry of the TiO_2 film, a sustained drug release using ibuprofen (IBU) and vancomycin (VAN) as model molecules from the film also was determined. Beside, adhesion behavior of osteoblast cells, together with an in vitro apatitic formation substantiated the cytocompatibility and bioactivity of the mesoporous TiO_2 films.

Keywords: mesoporus materials, nanostructure, metal oxides, CO_2 capture, controlled drug release.

Acknowledgments

首先我感謝我的父親世潤、母親寶環、老婆佳倫、弟弟彥熙、妹妹曉芬、三個寶貝女兒(郡瑀、雋峻、妤崢)、岳父連宗和岳母秀吉，謝謝你們在我辛苦奮鬥的五年中，給了我全部的支持與鼓勵。

本論文的付梓，最要感謝恩師陳三元教授與劉典謨教授對我的指導與提攜，並給了我許多跨領域前瞻性的研究。在研究團隊中，我感謝劉昆和博士、劉彥好博士、趙志欣學妹、董維琳學妹在藥物釋放研究上的幫忙與討論以及感謝張博學博士候選人、陳俞君學妹、李岱容學妹、李沅澤學弟在二氧化碳實驗上的協助與分享。我感謝陳三元教授研究室助理楊翊筠小姐與全體學弟妹在生活上的協助與支持。我感謝碩士班指導教授趙桂蓉博士在中孔洞材料研究上的啟發與指導。

我感謝過去在工研院同事(陳金銘博士、葉定儒博士、廖世傑博士、林秀芬博士、鄭季汝小姐)在生活上與研究上給予許多的支持與啟發，感謝在工研院電子顯微鏡團隊(郭行健博士、陳素梅小姐、范嘉雯小姐)在電子顯微鏡理論與實務操作技術上給予的指導與協助。

我感謝從小一起長大的弟妹們(宗智、鳳凰、山凱、景徽、蘭嫻、至鍵、佳佳、宗浩、閔煌、易峻、佩玲、健銘、明俊)，在這十五年來的日子裡，你們的情義相挺，讓我的生活變得更多采多姿。

最後，我僅將這論文獻給我的父母，謝謝你們的養育之恩。老爸、媽~我辦到了!我畢業了!終於取得博士學位了!你的教誨“**做人要誠信，承諾的事情一定要做到**”我會永遠記得的。

Table of Contents

中文摘要	I
Abstract	III
Acknowledgments	V
Table of Contents	VI
Figure Captions.....	X
Scheme Captions.....	XIV
Table Captions	XIV
Chapter 1. Introduction	1
Chapter 2. Literature Review	4
2-1 Mesoporous materials	4
2-1.1 Evolution of mesoporous materials.....	4
2-1.2 Formation mechanism of mesoporous materials.....	5
2-1.3 Formation method of Mesophase.....	7
2-1.3.1 Sol-gel process	7
2-1.3.2 Hydrothermal synthesis.....	7
2-1.3.3 Microwave assisted synthesis.....	7
2-1.4 Synthesis routes of mesoporous materials	8
2-1.5 Synthesis routes of mesoporous films.....	11
2-1.6 Functionalized mesoporous materials	12
2-2 Sorbent for CO₂ capture	14
2-2.1 Greenhouse effect and Greenhouse gas	14
2-2.2 Carbon capture technologies	17
2-2.2.1 Post-combustion capture	18
2-2.2.2 Pre-combustion capture.....	18

2-2.2.3 Oxy-combustion	18
2-2.3 High-temperature CO ₂ sorbents	20
2-2.4 Low-temperature CO ₂ sorbents	22
2-3 Mesoporous materials for drug delivery	23
2-3.1 Drug delivery of mesoporous materials	24
2-3.2 Bioactivity and release system of mesoporous materials.....	30
Chapter 3. Synthesis, Characterization, and CO₂ Adsorptive Behavior of Ordered Mesoporous AlOOH-Supported Layered Hydroxides	34
3-1 Introduction	34
3-2 Experiments	36
3-2.1 Synthesis of mesoporous metal oxides	36
3-2.2 Characterization of mesoporous metal oxides	37
3-3 Results and discussion.....	39
3-3.1 Characteristics of mesoporous metal oxides	39
3-3.2 Formation mechanism of mesoporous metal oxides	47
3-3.3 CO ₂ adsorptive behavior of mesoporous metal oxides	49
3-4 Conclusion.....	56
Chapter 4. Microwave Assisted In Situ Synthesis of Mesoporous Calcium Aluminate Nanocomposites	57
4-1 Introduction	57
4-2 Experiments	58
4-2.1 Preparation of mesoporous calcium aluminate nanocomposites.....	58
4-2.2 Characterization of materials	59
4-3 Results and discussion.....	60
4-3.1 Mesoporous Al ₂ O ₃	60
4-3.2 Mesoporous calcium aluminate nanocomposites.....	62

4-3.3 Formation mechanism of mesoporous calcium aluminate nanocomposites ...	70
4-4 Conclusion	73
Chapter 5. Synthesis and Characterization of Mesoporous Gd₂O₃ Nanotube and Its	
Use as a Drug-Carrying Vehicle	74
5-1 Introduction	74
5-2 Experiments	76
5-2.1 Synthesis of Gd ₂ O ₃ nanotube	76
5-2.2 Characterization	77
5-2.3 Loading of drug ibuprofen (IBU).....	77
5-2.4 Drug-release behavior under high-frequency magnetic field (HFMF)	78
5-2.5 Cell culture test	78
5-3 Results and discussion	79
5-3.1 Characteristics of Gd ₂ O ₃ nanotube.....	79
5-3.2 Formation mechanism of Gd ₂ O ₃ nanotube	85
5-3.3 IBU loading and release from Gd ₂ O ₃ nanotubes.....	86
5-3.4 Magnetically triggered IBU release from the nanotube	89
5-3.5 Cytotoxicity of Gd ₂ O ₃ nanotube	90
5-4 Conclusion	91
Chapter 6. Bioactive TiO₂ Ultrathin Film with Worm-like Mesoporosity for Controlled	
Drug Delivery	93
6-1 Introduction	93
6-2 Experiments	94
6-2.1 Preparation of the mesoporous TiO ₂ ultrathin films	95
6-2.2 Characterization of the mesoporous TiO ₂ ultrathin films	95
6-2.3 Loading and release behavior of IBU	96
6-2.4 Cell culture test of the mesoporous TiO ₂ ultrathin films.....	96

6-2.5 Bioactivity of the mesoporous TiO ₂ ultrathin films	97
6-3 Results and discussion	97
6-3.1 Characteristics of mesoporous TiO ₂ ultrathin film.....	97
6-3.2 Drug loading and release behavior from mesoporous TiO ₂ ultrathin film	100
6-3.3 Cell culture of mesoporous TiO ₂ film	107
6-3.4 Bioactivity of mesoporous TiO ₂ ultrathin film.....	108
6-4 Conclusion	111
Chapter 7. Conclusions	112
References	114
Appendix-1 Structure Identification and CO₂ Adsorption Behavior of Metal Oxides by Hydrothermal Coprecipitation Route	129
A.1-1 Introduction	129
A.1-2 Experiments	130
A.1-2.1 Preparation of metal oxides.....	130
A.1-2.2 Characterization and CO ₂ sorption analysis.....	131
A.1-3 Results and discussion	131
A.1-3.1 Structure Characterization.....	131
A.1-3.2 CO ₂ adsorption property of metal oxides.....	136
A.1-4 Conclusion	139
A.1-5 References	140
Appendix-2 Crystal Structure of Layered Double Hydroxides (LDHs)	141
A.2 References	142
Appendix-3 Crystal Structure of Mayenite Ca₁₂Al₁₄O₃₃	143
A.3 References	144
Curriculum Vitae	145
Publications	146

Figure Captions

Figure 2. 1 Structure of ordered mesoporous materials.....	5
Figure 2. 2 Mechanism for the synthesis of mesoporous silica under basic condition in the presence of cationic surfactant.....	6
Figure 2. 3 Scheme of the four synthesized routes of mesoporous materials: (a) precipitation, (b) TLCT, (c) EISA and (d) casting	10
Figure 2. 4 Structure evolution during mesoporous film preparation via the EISA process....	10
Figure 2. 5 Synthesis of mesoporous film.....	12
Figure 2. 6 An idealized model of the natural greenhouse effect.....	16
Figure 2. 7 Global average abundances of the major, well-mixed, long-lived greenhouse gases - carbon dioxide, methane, nitrous oxide and CFCs.....	16
Figure 2. 8 Comparing CO ₂ to global temperatures over the past century.....	17
Figure 2. 9 The illustration of post-combustion, pre-combustion, and oxy-combustion systems.....	19
Figure 2. 10 Mechanism of “close configuration of the ferrogels due to the aggregation of Fe ₃ O ₄ nanoparticles under “on” magnetic fields causes the porosity of the ferrogels to decrease.	30
Figure 3. 1 (a) small-angle XRD patterns, (b) large-angle XRD patterns of the MA, LDH/MA, and M-CaAl samples.	41
Figure 3. 2 (a) N ₂ adsorption isotherms of the MA, LDH/MA, and M-CaAl samples and (b) the corresponding pore size distribution.....	42
Figure 3. 3 The SEM images of (a) the synthesized M-AlOOH, (b) LDH/MA, and (c) M-CaAl samples.	43
Figure 3. 4 (a), (b), (d), (e) the TEM images and (c) EDS analysis of the LDH/MA sample. .	45
Figure 3. 5 (a) TEM image of the M-CaAl sample, the qualitative element mapping for Ca	

(b) and for Al (c) of the TEM image by EELS analysis, (d) the overlap image of the (b) and (c) resulting images, (e) the high resolution TEM image including its ED pattern, and (f) TEM image including nanotubes and ED pattern of the M-CaAl sample.....	46
Figure 3. 6 (a) CO ₂ adsorption capacity of M-CaAl sample by absorbed at 600 °C, inset includes the rate of CO ₂ sorption, (b) CO ₂ adsorption capacity of the sample at various temperature (200 °C, 400 °C, 600 °C, 700 °C, 800 °C), and (c) Comparison of CO ₂ adsorption curve in TGA and fixed bed, where the weight (%) calculation was divided by the total weight change of the sample.....	52
Figure 3. 7 (a) CO ₂ adsorption/desorption cycles of the M-CaAl sample adsorbed at 700 °C, (b) SEM image of the M-CaAl after 30 cycles, and (c) FTIR spectra of the M-CaAl after adsorption and desorption.....	55
Figure 4. 1 (a) small-angle XRD patterns of calcined mesoporous materials; (b) TEM images including the high resolution TEM image, (c) N ₂ adsorption isotherm and (d) pore size distribution of calcined mesoporous Al ₂ O ₃ (M-Al)	61
Figure 4. 2 (a) Large-angle XRD patterns and N ₂ adsorption isotherms including pore size distribution of calcined mesoporous materials.	62
Figure 4. 3 SEM images of calcined samples (M-CaAl sample (a) and (b) including EDS (c) for Spot 1) and (M-2CaAl sample (d))	65
Figure 4. 4 TEM images of calcined mesoporous materials (M-CaAl sample (a), (b)) and (M-2CaAl sample (c)); (d) showing the high resolution TEM image and FT pattern of the cubic area in the image (b)	67
Figure 4. 5 TEM image of the M-CaAl sample, the qualitative element mapping for Al (b) and for Ca (c) of the TEM image by EELS analysis, (d) the overlap image of the (b) and (c) resulting images. (Note: green dot indicating Ca; red dot incicating Al).....	68

Figure 4. 6 (a) X-ray Photoelectron and (b) FTIR Spectroscopy of the M-CaAl sample prepared by microwave hydrothermal treatment for 1h and calcined at 600 °C ..	70
Figure 4. 7 (a) Large-angle XRD patterns of calcined samples (M-CaAl) with different reactive time at 80 °C during microwave hydrothermal (MH) reaction and then calcined at 600 °C.; (b) and (c) SEM images of calcined samples (M-CaAl-MH-2h) with analyzing in two different areas.	71
Figure 5. 1 TEM images of the Gd ₂ O ₃ nanotube of (a) along [100] and (b) along [110].	80
Figure 5. 2 (a) Large-angle XRD pattern of the Gd ₂ O ₃ nanotube; the indexing is based on a ₀ = 1.08 nm (cubic symmetry, Ia3) and (b) small-angle XRD pattern of the Gd ₂ O ₃ nanotube; the indexing is based on a ₀ = 6.54 nm (p6 mm).	81
Figure 5. 3 (a) TEM images, (b) high-resolution TEM (HRTEM) image, (c) ED pattern and (d) EDS of the Gd ₂ O ₃ nanotube.	83
Figure 5. 4 (a) N ₂ sorption isotherms of the Gd ₂ O ₃ nanotube; (b) showing the corresponding pore size distribution and (c) TEM image of the Gd ₂ O ₃ nanotube showing order and larger pores.	84
Figure 5. 5 FTIR spectra of (a) the neat Gd ₂ O ₃ nanotube and (b) the Gd ₂ O ₃ nanotube after IBU uptake and IBU.	88
Figure 5. 6 (a) IBU release profiles from the Gd ₂ O ₃ nanotube under the magnetic field switching on and off and (b) hysteresis loop analysis of the Gd ₂ O ₃ nanotube.	89
Figure 5. 7 Cell viability of ARPE-19 cells incubated for 48 h with different concentrations (1000 µg ml ⁻¹ , 500 µg ml ⁻¹ , 100 µg ml ⁻¹ , 50 µg ml ⁻¹ , and 10 µg ml ⁻¹) of the samples.	91
Figure 6. 1 Large-angle XRD pattern of the mesoporous TiO ₂ ultrathin film.	98
Figure 6. 2 Small-angle XRD pattern of the mesoporous TiO ₂ ultrathin film (a) before and (b) after calcinations.	99
Figure 6. 3 TEM image of the mesoporous TiO ₂ ultrathin film after calcinations.	100

Figure 6. 4 FTIR spectra of (a) the mesoporous TiO ₂ ultrathin film, (b) the IBU loaded mesoporous TiO ₂ ultrathin film, (c) pure IBU, (d) pure VAN, and (e) the VAN loaded mesoporous TiO ₂ ultrathin film.	102
Figure 6. 5 Mean cumulative ibuprofen release behavior from the mesoporous TiO ₂ ultrathin film with different immersed concentration.	103
Figure 6. 6 The molecular structure of ibuprofen and vancomycin drugs (a), the illustration of drug loading method for various molecular size (b) and those drugs delivery profile during 30 h (c).....	106
Figure 6. 7 Microscopic images (a-c) and cell number calculation (d) of osteoblastic cell incubated for 48 h on the different substrate (glass as control (a), TiO ₂ ultrathin film for before (b) or after calcination (c)). For cell counting, the results were averaged and presented as mean \pm SD, and analyzed by Student's t-test (p value <0.05).....	108
Figure 6. 8 (a) SEM, (b) LA-XRD and, (c) EDS analysis of the calcined mesoporous TiO ₂ ultrathin film soaked in SBF for 10 days.....	110

Scheme Captions

Scheme 3. 1 Illustration of the formation mechanism of ordered mesoporous metal oxide materials.....	48
Scheme 4. 1 The formation mechanism of mesoporous calcium aluminate nanocomposites.	73
Scheme 5. 1 The formation mechanism of Gd ₂ O ₃ nanotube.....	86

Table Captions

Table 2. 1 A comparison of high-temperature CO ₂ sorbents.	22
Table 2. 2 A comparison of low-temperature CO ₂ sorbents.	22
Table 6. 1 Composition of calcium phosphate on mesoporous TiO ₂ thin films soaked in SBF for 10 days.....	110

Chapter 1

Introduction

Mesoporous materials usually have high surface area and large pore volume. The pore diameters are narrowly centered at 2-50 nm. Hence, novel mesoporous materials with nanostructured morphology have been developed by different synthesized routes, which include sol-gel route, microwave-assisted synthesis, co-precipitation, solid-state reaction, and hydrothermal urea reaction in our lab. One of the objectives of this thesis study is to extend this synthesized approach to develop nanostructured porous materials, and to explore some new potential applications, such as carbon dioxide capture and controlled drug delivery.

Chapter 2 presents literature review focused on the synthesis of mesoporus materials and a potential application of these materials in the carbon dioxide capture or drug delivery is also included in this chapter.

A pre-study on the sorbents for CO₂ capture, in the Appendix-1, which presents a study focused on the synthesis of the metal oxides (M-Al-O; M=Mg, Ca, and Sr). To use hydrothermal co-precipitation route, the metal oxide precursors was fabricated by the divalent metal ion and trivalent metal ion in basic solution. These metal oxides can be use as CO₂ sorbent at various adsorption temperatures. Moreover, the structural characterization and CO₂ adsorption behavior of the metal oxide is clearly described in the Appendix-1.

Chapter 3 presents the studies on a novel mesoporous CaAl oxides, which was prepared by synthesizing and modifying AlOOH-supported CaAl layered double hydroxides (CaAl LDHs) in hydrothermal urea reaction. The mesoporous CaAl metal oxides exhibited ordered hexagonal mesoporous arrays or uniform nanotubes with a large surface area, narrow pore size distribution, and highly crystalline frameworks. The mesoporous metal oxides were used as a solid sorbent for high-temperature CO₂ capture and displayed a

maximum CO₂ capture capacity and rapid adsorption rate longer cycle life. The formation mechanism of mesoporous metal oxides also is firstly proposed and discussed in this chapter.

Chapter 4 presents the studies on the original mesoporous calcium aluminate nanocomposites. The microwave-hydrothermal (M-H) process was used to promote the synthesis of the nanocomposites. The mesoporous nanocomposites include crystalline nanorod grown on the mesoporous structure. The formation mechanism of the nanocomposites, and its application for CO₂ capture are also suggested in this study.

Chapter 5 involves the application of mesoporous Gd₂O₃ nanotubes with innovative nanostructure in controlled drug delivery. This material was prepared by combining soft template and sol-gel methods. Gd₂O₃ nanotube exhibited weak superparamagnetic property and was found to be able to carry and elute a model molecule, i.e. ibuprofen (IBU), in a controllable manner via an external magnetic field. The mechanism of IBU release from the nanotubes with and without the use of magnetic stimulus was proposed. And, the formation mechanism of nanostructured Gd₂O₃ also proposed in this chapter.

Chapter 6 deals with the application of bioactive mesoporous TiO₂ thin film in controlled drug delivery. The TiO₂ film coatings with a wormhole-like architecture were synthesized using evaporation-induced self-assembly (EISA) method. The film own ultrathin thickness and open-porous nanostructure. By taking advantage of the tortuosity of the worm-like mesoporous architecture associated with the chemistry of the TiO₂ film, a sustained drug release using ibuprofen and vancomycin as model molecules from the film was determined. Besides, adhesion behavior of osteoblast cells, together with an in vitro apatitic formation substantiated the cytocompatibility and bioactivity of the mesoporous TiO₂ films. Such combined bioactive and drug-releasing functions of the TiO₂ films ensure an improved therapeutic performance for potential applications included orthopedics, dentistry, and drug delivery.

Chapter 7 presents focused on a brief summary for these studies in this thesis.



Chapter 2

Literature Review

2-1 Mesoporous materials

2-1.1 Evolution of mesoporous materials

According to the IUPAC definition, porous materials are divided into three classes. Mesoporous materials have pore sizes between 2 and 50 nm. When pore sizes are less than 2 nm, the materials are defined as microporous. And when pore sizes are larger than 50 nm, the materials are called macroporous ^[1]. Generally, porous materials can be usually used as adsorbents, catalysts and carriers owing to their high surface areas and uniform pore size.

In 1992, a novel family of mesoporous silicate-based materials, the M41S, was fabricated through self-assembly and supramolecule templating mechanism, and invented by the researchers at Mobil company ^[2] and Toyota Research Center ^[3] simultaneously. The M41S materials with their ordered channel and interconnected pore systems, uniform apertures in the range of 2-10 nm diameter and surface area greater than 800 m²/g have expanded the pore size related application of zeolites and zeolite-like materials from the microporous to the mesoporous regime ^[4-5]. Several mesoporous structures including 2D-hexagonal MCM-41(P6mm), 3D-bicontinuous cubic MCM-48 (Ia-3d) and lamellar MCM-50 etc. have been reported in Figure 2.1 ^[6-8].

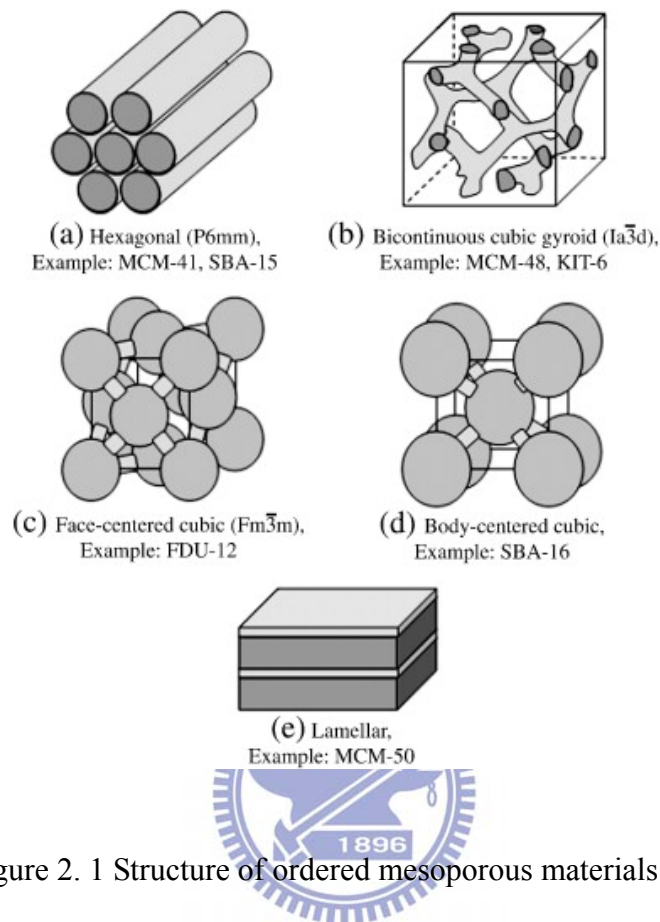


Figure 2. 1 Structure of ordered mesoporous materials ^[6-8].

2-1.2 Formation mechanism of mesoporous materials

Typical mesoporous silica material is formed by micelle-templating process, either following electrostatically driven cooperative assembly pathway or the nonionic route in the presence of surfactant as structure directing agent ^[9]. Figure. 2.2 shows the mechanism for the synthesis of mesoporous silica under electrostatic interaction pathway. The steps in the synthesis include:

- (1) displacement of the surfactant counterions by inorganic cations forming organic-inorganic ion-pairs, which self organize into a liquid crystal-like mesophase,
- (2) crosslinking of the inorganic species,
- (3) a rigid replica of the underlying liquid crystalline phase forms.

Moreover, alkyl poly(ethylene oxide) oligomeric surfactants and poly(alkylene oxide) block copolymers are the nonionic surfactant used in the nonionic route ^[10]. Hydrogen bonding is a predominant driving force for pairing the inorganic and organic species in the presence of neutral nonionic surfactant ^[9]. Generally, cationic or nonionic surfactants are utilized as the micelle template to obtain well-ordered mesoporous materials. The massive production and relatively low cost of anionic surfactants (phosphate, sulfate, carboxylate, sulfonate, etc) has attracted researcher's focus on the synthesis of ordered mesoporous materials using anionic surfactants as templates^[11]. Yokoi et al.^[12] reported the first synthesis of the anionic-templated mesoporous silica (AMS) using anionic surfactant. An organoalkoxysilane with a positively charged functional group is introduced as an additional silica source to interact with the anionic headgroup, forming the silica-micelle composite.

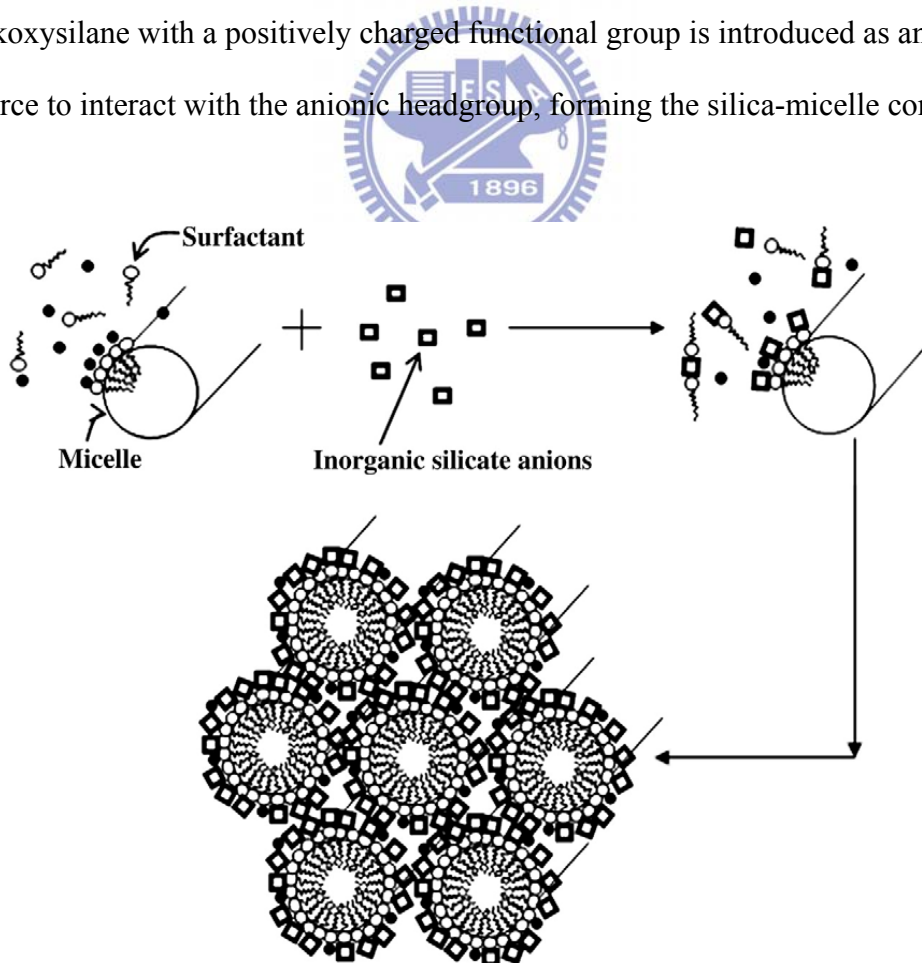


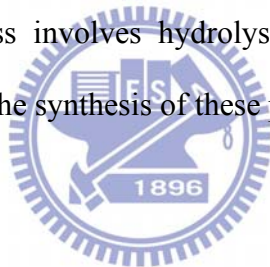
Figure 2. 2 Mechanism for the synthesis of mesoporous silica under basic condition in the presence of cationic surfactant^[9].

2-1.3 Formation method of Mesophase

Ordered mesoporous materials in micelle-templating system can be synthesized by following the conditions and synthesis methods for different types. Generally, the mesophase can be synthesized through hydrothermal synthesis, microwave assisted hydrothermal synthesis and sol-gel process.

2-1.3.1 Sol-gel process

The sol-gel process is well-established route to synthesize porous inorganic materials with controlled microstructure, high thermal and chemical stability in the micro- and mesoporous range. Sol-gel process involves hydrolysis and condensation of respective precursor to form colloidal sol for the synthesis of these porous inorganic materials ^[13].



2-1.3.2 Hydrothermal synthesis

Hydrothermal crystallization is the common method used for crystallizing substances from aqueous solutions at moderate temperature and pressure. This method has been widely used for synthesis from inorganic microporous materials ^[14-15] to mesoporous materials ^[16].

2-1.3.3 Microwave assisted synthesis

Microwave assisted hydrothermal synthesis is also reported for the formation of porous material. Microwave assisted synthesis offers many distinct advantages over conventional synthesis methods. These include rapid heating to crystallization temperature, homogeneous nucleation, fast supersaturation by the rapid dissolution of precipitated gels and much shorter crystallization time ^[17-20]. Thus, microwave heating mode provides a better way to control the crystallinity and morphology ^[21].

2-1.4 Synthesis routes of mesoporous materials

According Soler-Illia and Azzaroni have recently reported literature, the four synthesized routes of mesoporous materials included precipitation, true liquid crystal templating, evaporation-induced self-assembly and casting in Figure 2.3(a)-(d) [22].

- (a) Precipitation (Figure 2.3(a)): this route is the cooperative assembly of the inorganic species and the template material that occurs upon hydrolysis and condensation of the inorganic species. During the process, the mesophase with local order is formed first; and aging can cause rearrangement of that mesophase which leads to highly ordered mesostructured materials. In order to obtain highly ordered pores, it is crucial to control the inorganic hydrolysis and condensation. However, precipitation methods are straightforward and large quantities are obtained at the same time, mesoporous phases obtained from precipitation can only be processed as powders, which blocks the further application of these materials.
- (b) True liquid crystal templating (TLCT) (Figure 2.3(b)): this route is developed by Attard et al. which included the formation of a liquid crystalline mesophase, infiltration of this mesophase with the mineral precursor, and the formation of the mineral walls in the aqueous regions between the micelles by inorganic condensation (oxides, sulfides) or electrodeposition (metals). This method is majorly used for producing the mesoporous metal electrodes.
- (c) Evaporation-induced self-assembly (EISA) (Figure 2.3(c)): the EISA process was first designed for the preparation of mesostructured thin films (MTFs) by Brinker et al.; which is based on the solvent evaporation from dilute solutions containing inorganic precursors, templating materials and other additives, thus further forming the mesoporous materials. The evaporation of solvent will drive the self-assembly of inorganic species-surfactant micelles as presented in Figure 2.4, and further organized into ordered mesostructures. The EISA procedure has been the most

widely-used method for the preparation of mesoporous nanocomposites or other organic-inorganic nanocomposites in the forms of films, filters, fibers, powders or ordered porous structure; which can be used in continuous membrane-based separation and catalysis, protective coatings, optical films, and sensors.

- (d) Casting (Figure 2.3(d)): this route is hugely different from the routes presented above; which uses the porous material act as “hard template” in the synthesis instead of uses the organic surfactants for soft templating to get the pore system. A mesoporous matrix is used as precursors for the desired phase, and then removing the exotemplate to obtain the continuously porous solid or finely divided particles. This method is extremely useful in synthesis of mesoporous carbons and low-valence transition metal oxides.



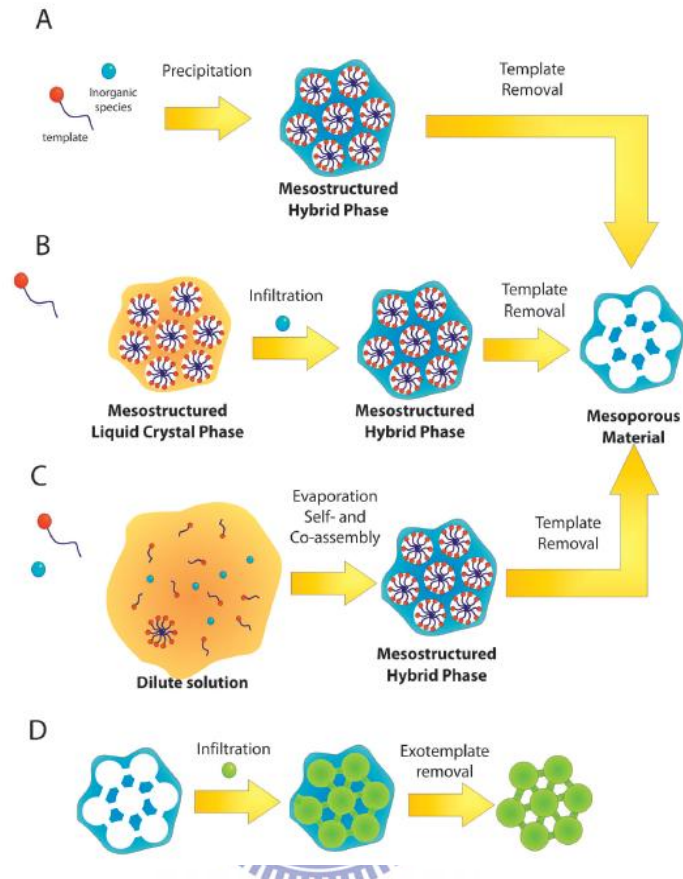


Figure 2. 3 Scheme of the four synthesized routes of mesoporous materials: (a) precipitation, (b) TLCT, (c) EISA and (d) casting [22].

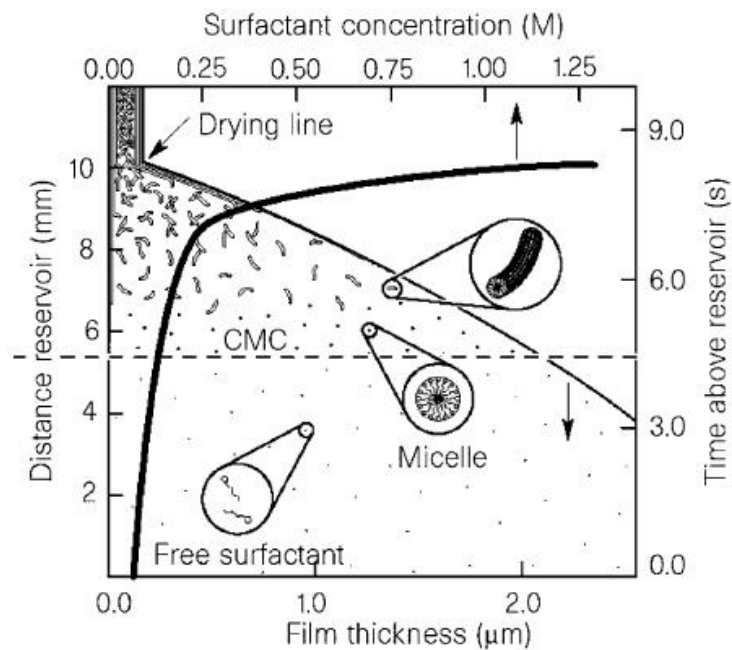


Figure 2. 4 Structure evolution during mesoporous film preparation via the EISA process [23].

2-1.5 Synthesis routes of mesoporous films

The morphologies of mesoporous materials cover powder, fiber, film, hard sphere, hollow, rod and monolith ^[24-26]. Besides powder, film has attracted the most attention because of their potential uses in chemical sensor, membrane separation, optical devices, electronic devices and biomatrix ^[5, 27-33].

Figure 2.5 presents the general method for the synthesis of mesoporous thin films. The most common methods to prepare films from a synthesis solution or precursor sol are growth from solution and solvent evaporation methods. In the growth from solution method, the synthesis solution is brought to contact with a second phase. The second phase could be solid support where the film is deposited, air or liquid (oil) where the film is self-supporting ^[34]. Generally solid support submerged in the synthesis solution is subjected to hydrothermal synthesis at required temperature and time to allow formation of membrane at the solid support interface ^[35]. In the solvent evaporation method, a liquid film containing silica precursor, solvent and surfactant is formed on a substrate followed by evaporation of the solvent ^[34]. The solvent evaporation method for ordered mesoporous films is generally conducted following three routes: (a) dip-coating ^[36], (b) spin-coating ^[37] or (c) slip-casting ^[38]. Dip-coating is a method where the substrate is dipped into and withdrawn from a precursor solution. In the spin-coating method, liquid precursor is deposited on the surface of the substrate followed by the application of centrifugal force to flow the liquid radially outward. Slip-casting is another method where the precursor solution is dropped on the substrate followed by its solidification, leaving a membrane on the substrate ^[34]. Slow evaporation of the solvent during dip-coating, spin-coating or slip casting induces self-assembly of the inorganic species and micelles at the solid-liquid interface, leaving a film on the surface of the substrate ^[10]. Generally, the removal of surfactant from the mesoporous silica materials is achieved via calcinations ^[39] or solvent extraction ^[40].

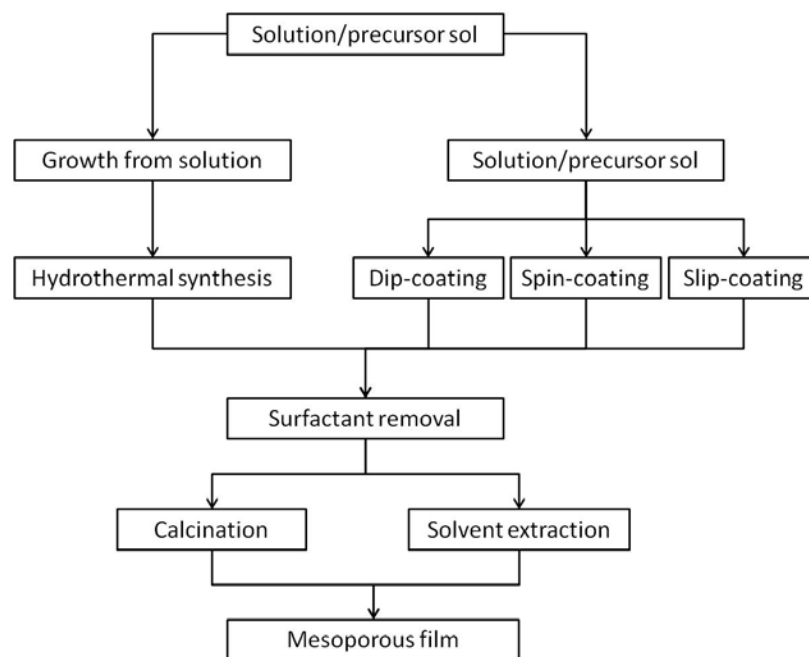


Figure 2. 5 Synthesis of mesoporous film.

2-1.6 Functionalized mesoporous materials

Functionalization with amine groups can be done through several ways: (a) impregnation, (b) post-synthesis grafting, (c) direct cocondensation and (d) anionic surfactant template method.

- (a) Impregnation is one method to load high amount of amines on the mesoporous silicas ^[41]. Impregnation of the mesoporous silica with organosilane or polymer-containing amino group was performed by adding amine to solvent, followed by addition of the mesoporous silica. The excess solvent is evaporated to dryness ^[41-42]. The disadvantage exhibited by impregnation is the amines loaded tend to conglomerate ^[43].
- (b) Post-synthesis grafting is a reaction between surface hydroxyl groups (on silanol groups) on the mesoporous silicas and the alkoxy ligands of the silane, formatting a layer of tethered amine groups on the surface of mesoporous silicas ^[44].
- (c) Direct co-condensation of amine groups is a method where amine groups are covalently bonded into the silica matrix, unlike the surface modification of

post-synthesis grafting ^[45]. In the direct co-condensation method, the aminosilane, surfactant and silica precursor were mixed together and subjected to aging to allow hydrolysis and condensation of silica precursor ^[46]. The direct co-condensation method is simpler than the postsynthesis grafting in terms of reduction in number of synthesis steps and it also allows the uniform distribution of various functional groups without pore blocking ^[47-48].

(d) Anionic surfactant template route: Yokoi et al. ^[12] reported the synthesis of anionic-surfactant-templated mesoporous silica (AMS), based on anionic surfactants as templates. Aminosilane or quaternized aminosilane used in the study, serve as costructure-directing agent (CSDA) and functional group for CO₂ adsorption at the same time. The anionic-surfactant-templated route involves condensation of the CSDA with the inorganic precursors, followed by attachment of the ammonium sites of CSDA to silicon atoms incorporated into the wall and electrostatic interaction between the ammonium sites with the anionic surfactants, producing well-ordered AMS ^[49].

Lim and Stein ^[50] prepared the vinyl-functionalized MCM-41 samples by post-synthesis grafting and direct co-condensation synthesis methods. It was found that vinyl groups were distributed uniformly in vinyl-functionalized MCM-41 via direct co-condensation method, however, non-uniformly distributed vinyl groups appeared in MCM-41 via the post-synthesis grafting.

2-2 Sorbent for CO₂ capture

2-2.1 Greenhouse effect and Greenhouse gas

An idealized model of the natural greenhouse effect is shown in Figure 2.6 ^[51]. The Sun powers Earth's climate, radiating energy at very short wavelengths, predominately in the visible or near-visible (e.g., ultraviolet) part of the spectrum. Roughly one-third of the solar energy that reaches the top of Earth's atmosphere is reflected directly back to space. The remaining two-thirds is absorbed by the surface and, to a lesser extent, by the atmosphere. To balance the absorbed incoming energy, the Earth must, on average, radiate the same amount of energy back to space. Because the Earth is much colder than the Sun, it radiates at much longer wavelengths, primarily in the infrared part of the spectrum. Much of this thermal radiation emitted by the land and ocean is absorbed by the atmosphere, including clouds, and reradiated back to Earth. This is called the greenhouse effect. The glass walls in a greenhouse reduce airflow and increase the temperature of the air inside. Analogously, but through a different physical process, the Earth's greenhouse effect warms the surface of the planet. Without the natural greenhouse effect, the average temperature at Earth's surface would be below the freezing point of water. Thus, Earth's natural greenhouse effect makes life as we know it possible. However, human activities, primarily the burning of fossil fuels and clearing of forests, have greatly intensified the natural greenhouse effect, causing global warming.

Greenhouse gas (GHGs) are defined as the atmospheric gases that can trap the outgoing radiation and re-radiate the radiation to the planetary surface in the thermal infrared range. This is how the greenhouse effect caused and results the temperature higher than it would be. The main GHGs are carbon dioxide, methane, nitrous oxides, halogenated compounds (mainly CFCs) and ozone, the kind of gas molecule with dipole moment which would be affected by infrared radiation and also with long life time; that takes years to leave the atmosphere and causes significantly contribution to the greenhouse effect. According to

the report of the Annual greenhouse gas index (AGGI) from National Oceanic & Atmospheric Administration (NOAA) in 2011 ^[52], the actual contributions of these GHGs are displayed in Figure 2.7. The growth rate of CO₂ has averaged about 1.68 ppm per year over the past 31 years (1979-2010). The CO₂ growth rate has increased over this period, averaging about 1.43 ppm per year before 1995 and 1.94 ppm per year thereafter. The growth rate of methane declined from 1983 until 1999, consistent with an approach to steady state. Superimposed on this decline is significant interannual variability in growth rates. The approach to steady state may have been accelerated by the economic collapse of the former Soviet Union and decreased emissions from the fossil fuel sector. From 1999 to 2006, the CH₄ burden was about constant, but since 2007, globally averaged CH₄ has begun increasing again. Causes for the recent increases are warm temperatures in the Arctic in 2007 and increased precipitation in the tropics in 2007 and 2008. Nitrous oxide continues to increase at a relatively uniform growth rate, while radiative forcing from the sum of observed CFC changes ceased increasing in about 2000 and is now declining. The latter is a response to decreased emissions related to the Montreal Protocol on substances that deplete the ozone layer.

Among the GHGs, CO₂ is believed as the control knob of the greenhouse effect ^[53], since the concentration of CO₂ in atmosphere is much more than other GHGs. Some physical evidences also show that CO₂ is the most significant climate-relevant greenhouse gas that induces severe climate change. The major source of CO₂ is the combustion of fossil fuels or gas by power stations leading a continuing high rate of CO₂ increase. The recent data is shown in Figure 2.8 ^[54]. While CO₂ concentration is rising from 1970 to 2010, global temperatures obviously increased by the rate of 0.015 °C per year.

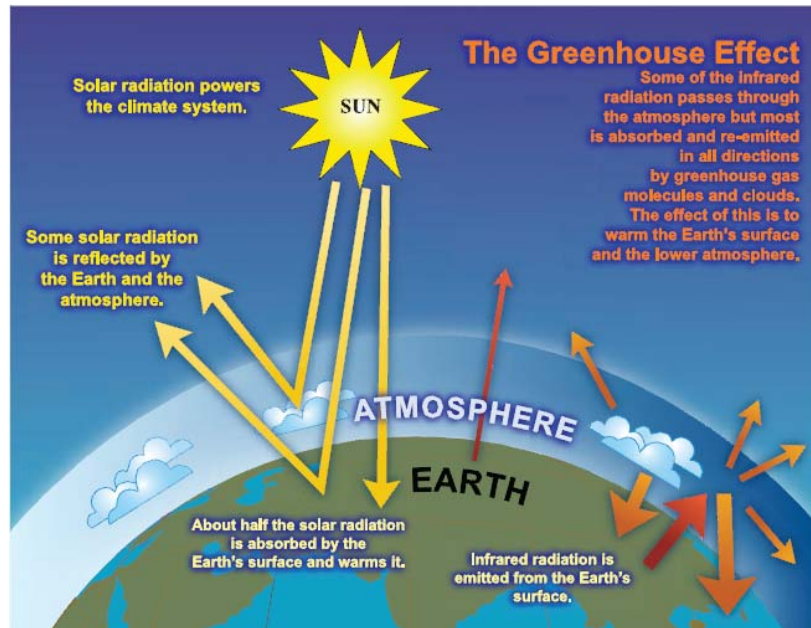


Figure 2. 6 An idealized model of the natural greenhouse effect ^[51].

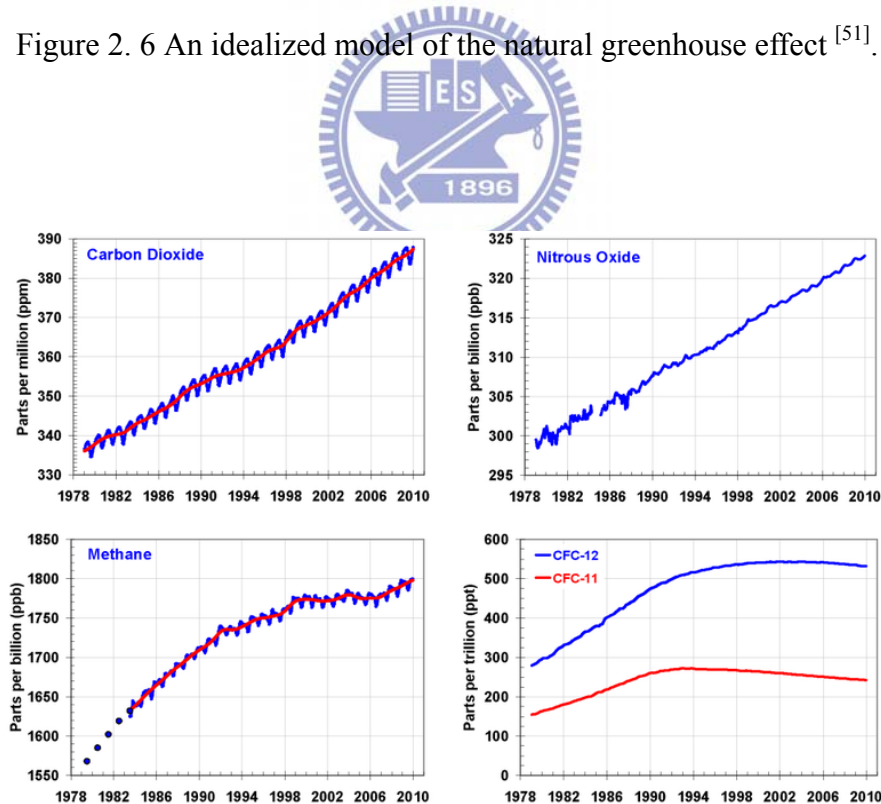


Figure 2. 7 Global average abundances of the major, well-mixed, long-lived greenhouse gases - carbon dioxide, methane, nitrous oxide and CFCs ^[52].

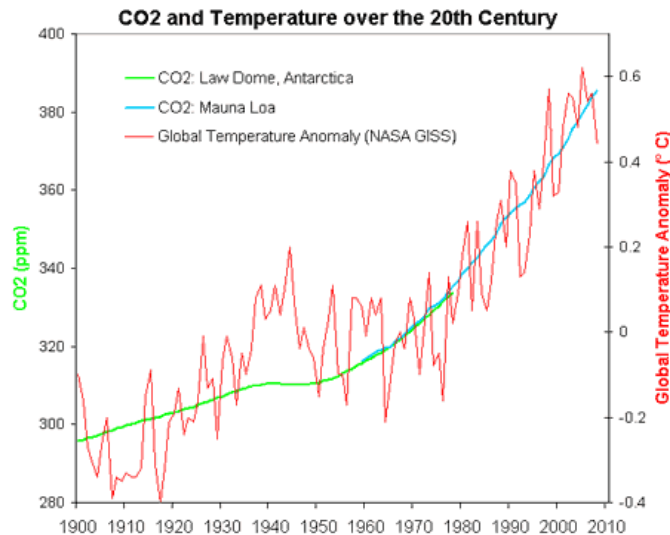


Figure 2. 8 Comparing CO₂ to global temperatures over the past century ^[54].

2-2.2 Carbon capture technologies ^[55]

Although there is not universal agreement on the cause, there is a growing consensus that global climate change is occurring, and many climate scientists believe that a major cause is the anthropogenic emission of greenhouse gases (GHGs) into the atmosphere. Due to their low cost, availability, existing reliable technology for energy production, and energy density, fossil fuels currently supply over 85% of the energy needs of the United States and a similar percentage of the energy used worldwide ^[56-57]. The combustion of fossil fuels produces carbon dioxide (CO₂), a GHG with an increasing potential for by-product end-use in the industrial and energy production sectors. The use of CO₂ as a by-product would not only have economic benefits but would simultaneously mitigate global climate change concerns.

However, In consideration of how best to improve CO₂ capture, there are three technological pathways that can be pursued for CO₂ capture from coal-derived power generation: post-combustion capture, pre-combustion capture, and oxy-combustion, as illustrated in Figure 2.9 ^[55]. All three of these pathways are under investigation, some at an early stage of development.

2-2.2.1 Post-combustion capture

Post-combustion capture involves the removal of CO₂ from the flue gas produced by combustion. Existing power plants use air, which is almost four-fifths nitrogen, for combustion and generate a flue gas that is at atmospheric pressure and typically has a CO₂ concentration of less than 15%. Thus, the thermodynamic driving force for CO₂ capture from flue gas is low (CO₂ partial pressure is typically less than 0.15 atm), creating a technical challenge for the development of cost effective advanced capture processes. In spite of this difficulty, post-combustion carbon capture has the greatest near-term potential for reducing GHG emissions, because it can be retrofitted to existing units that generate two-thirds of the CO₂ emissions in the power sector.



2-2.2.2 Pre-combustion capture

In pre-combustion CO₂ capture, the CO₂ is recovered from some process stream before the fuel is burned. To the extent that the concentration and pressure of the CO₂ containing stream can be increased, then the size and cost of the capture facilities can be reduced. This has led to efforts to develop combustion technologies that inherently produce concentrated CO₂ streams or CO₂ containing streams at high pressure, for which there are existing capture processes.

2-2.2.3 Oxy-combustion

An alternative to capturing carbon from fuel gas or flue gas is to modify the combustion process so that the flue gas has a high concentration of CO₂. A promising technology for accomplishing this is oxy-combustion, in which the fuel is burned with nearly pure oxygen (greater than 95%) mixed with recycled flue gas. In the most frequently proposed version of this concept, a cryogenic air separation unit (ASU) is used to supply high purity oxygen to a PC-fired boiler. This high purity oxygen is mixed with recycled flue

gas prior to combustion or in the boiler to maintain combustion conditions similar to an air fired configuration. This is necessary because currently available materials of construction cannot withstand the high temperatures resulting from coal combustion in pure oxygen. For a new unit, it should be possible to use smaller boiler equipment due to increased efficiency. The main attraction of this process is that it produces a flue gas which is predominantly CO₂ and water. The water is easily removed by condensation, and the remaining CO₂ can be purified relatively inexpensively. Conditioning of the flue gas consists of drying the CO₂, removal of O₂ to prevent corrosion in the pipeline, and possibly removal of other contaminants and diluents, such as Ar, N₂, SO₂, and NO_x.

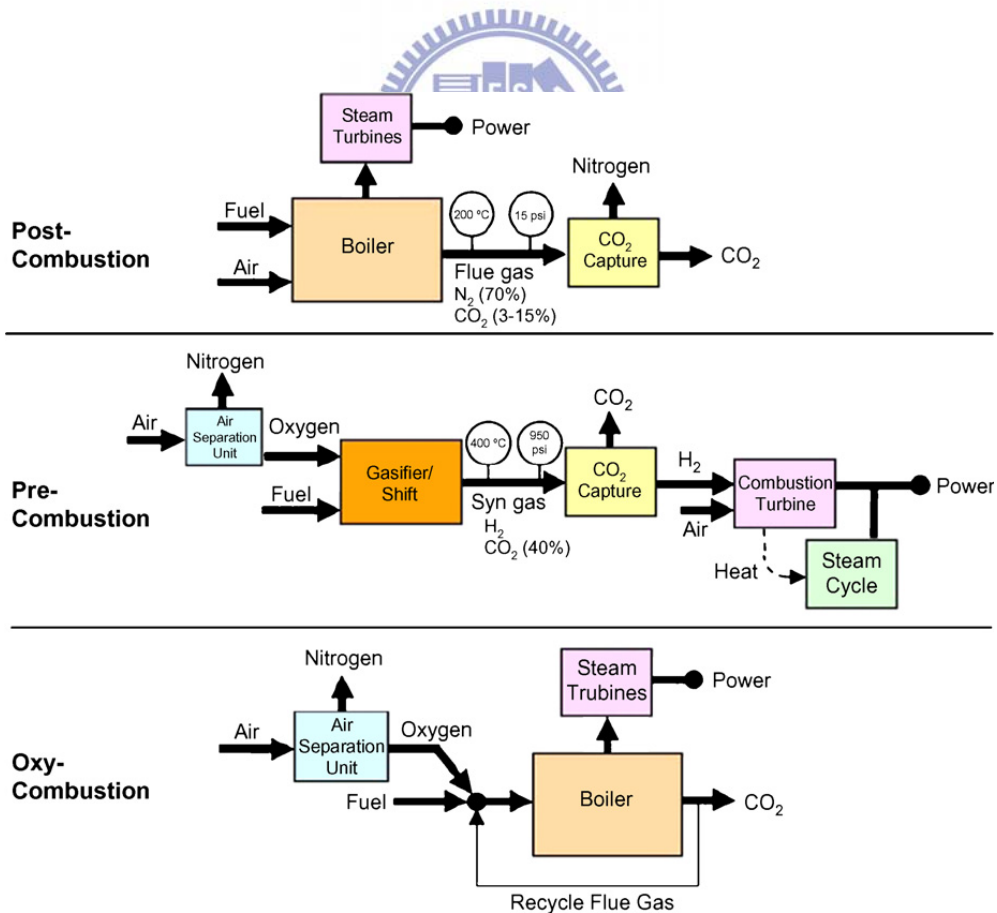


Figure 2. 9 The illustration of post-combustion, pre-combustion, and oxy-combustion systems ^[55].

The CO₂ produced is captured prior to combustion, while transferring the energy content of the fuel to hydrogen. Various pre-combustion routes for electricity production have been investigated, using a membrane reactor ^[58-59] or the sorption-enhanced reaction process (SERP) ^[60-61]. Hence, for using in a steam reforming reactor, the sorbent materials should own to the following requirements:

- (a) It should be able to remove sufficient CO₂ at the temperature range of 400-600 °C and in the pressure range of 1-40 bar.
- (b) It should be able to withstand the high $P_{\text{steam}}/P_{\text{CO}_2}$ ratios at the steam reforming conditions in a SERP reactor (> 20), where P_{steam} and P_{CO_2} are the partial pressures of respectively steam and CO₂ gas.
- (c) It should be mechanically and chemically stable for extended periods at these conditions.
- (d) The kinetics of adsorption and desorption should be sufficiently fast.

2-2.3 High-temperature CO₂ sorbents

Recently, for CO₂ capture at high temperature, the attractive materials which applied to a fuel-processing step for SERP can be divided in the following four types:

1. Metal oxides: the basic metal oxide (MgO or CaO) can react chemically with acidic CO₂ to form CaCO₃ at high temperature (200-600°C) ^[62]. Recently, aluminum oxide is also studied since it is a weak basic material and with chemical modification by adding some other metal oxides composing stronger basicity, the CO₂-uptake capacity at high temperature can be greatly increased ^[63].
2. Hydrotalcites ^[64]: LDHs belong to a large class of anionic and basic clays, which is also known as the hydrotalcite-like compounds (HTlcs). And the derivatives of LDHs (calcined material) also show the ability as the appropriate CO₂ sorbents at high temperature. LDH is presented by the general formula

$[(M(II)_{1-x}M(III)_x(OH)_2)]^{x+}[A^{n-}_{x/n} \cdot mH_2O]^{x-}$, where M(II) is usually Mg^{2+} , Ni^{2+} , Zn^{2+} , Cu^{2+} , M(III) is usually Al^{3+} , Fe^{3+} , Cr^{3+} , and A^{n-} is CO_3^{2-} , SO_4^{2-} , NO_3^- , Cl^- , OH^- . The majority of studies have focused on the most common naturally existing form of LDH, Mg-Al- CO_3 (see Appendix-2). Many studies have shown that Mg-Al LDH can adsorb CO_2 at about 400° [65]; however it cannot be applied to CO_2 capture at higher temperature, which further blocks its future application. Recently some studies were carried out by replacing the Mg^{2+} by Ca^{2+} , and thus greatly raised the adsorption temperature to around $600^\circ C$.

3. Double salts: Potassium double salts were identified as the active phase in the decomposition products of K_2CO_3 -impregnated hydrotalcite using high-temperature X-ray diffraction. Synthesizing double salts directly, rather than preparing them as a side product by decomposition of hydrotalcite, resulted in sorbents having higher adsorption capacity and improved kinetics compared with promoted hydrotalcites [66].
4. Lithium metal oxides: the sorbents were discovered by Toshiba in their molten carbonate research when they added ZrO_2 to the molten electrolyte. The product, Li_2ZrO_3 , was found to be a good CO_2 sorbent, as were other lithium metal oxides [67-68]. In addition, Table 2.1 exhibits a comparison of high-temperature CO_2 sorbents.

Table 2. 1 A comparison of high-temperature CO₂ sorbents.

High Temp (200-700°C)	Properties	Sorbents	Disadvantages
<200°C	physical	Layered double Hydroxides	Less CO ₂ Capacity
200-400°C	Chemical	MgO, MgAl-LDO	Poor cyclic life
500°C-700°C	Chemical	CaO, CaAl-LDO, LiZr ₂ O ₃	Poor cyclic life
>700°C	Chemical	SrO, SrAlO, modified-LiZr ₂ O ₃	Poor cyclic life

2-2.4 Low-temperature CO₂ sorbents

The conventional technologies for removal of CO₂ are cryogenic distillation, amine absorption^[69-70] and absorbent liquid absorption through membrane contactor^[71]. Amine absorption is the widely developed commercial technology for CO₂ removal. However, there are a number of drawbacks of using amine type liquid absorbent such as high energy consumption for solvent regeneration, equipment corrosion and flow problems caused by viscosity^[72-73]. After removal of CO₂ from its source such as flue gas via capture by amine absorption, an additional step is needed to isolate and regenerate the solvent. Owing to the high cost of regeneration process^[74], regenerable solid adsorbents appear to be alternative for CO₂ adsorption over the conventional methods. Physical adsorbents based on carbons and zeolites are able to reversibly adsorb large quantity of CO₂ at room temperature^[72]. Table 2.2 displays a comparison of low-temperature CO₂ sorbents.

Table 2. 2 A comparison of low-temperature CO₂ sorbents.

Low Temp. (<200°C)	Properties	Sorbents	Disadvantages
Liquid (<120°C)	Chemical	Liquid amine	High cost (Regeneration)
(100-200°C)	Physical	Carbon, Zealite, modified-MOF	Desorption at high Temp.
(50-120°C)	Chemical	Amine-Mesoporous Material Alkali metal carbonate	Temp. Limit (CO ₂ Capture)

However, these physical adsorbents have several disadvantages such as reduced CO₂ adsorption capacity at high temperature, requirement of high temperature regeneration and poor tolerance to water ^[42]. Recently, there has been increased interest in developing mesoporous materials (molecular sieve) for adsorption of CO₂ due to their high porosity to facilitate rapid gas diffusion to and from their surface ^[75]. Their pores are large enough to be accessible for various functional groups. The introduction of functional groups such as amine groups to these mesoporous materials to create specific interactions with CO₂ has gained importance to overcome the disadvantages of the conventional amine absorption processes ^[76].

2-3 Mesoporous materials for drug delivery

In the past few years there has been an exceptional growth in research focused on drug delivery systems. This explosion has been induced by the features and possibilities that these systems offer to biomedicine, such as the possibility of several drugs to be administrated using new therapies improving efficacy and safety; the chance of delivering new complex drugs that otherwise would not be possible; the improvement of therapeutic responses with continuous drug release patterns rather than pulsatile; and the opportunity that recent advances in materials science and biotechnology offer to develop new physical and medical methods of drug delivery. Among all the new, available drug delivery technologies, mesoporous materials fulfill all the previously mentioned requirements. Mesoporous materials of various shapes, geometries, and compositions with interior and exterior surfaces decorated with organic functionalities have huge potential in a variety of bio-applications ^[77-79]. Their porosity and textural properties have fuelled their use as drug delivery systems and their chemical composition, similar to bio-glasses, make them good candidates to be employed in osseous regeneration technologies. The textural properties of ordered mesoporous silicas, such as high surface area and large internal volume, allow the

adsorption of drugs and biologically active species into their structures. The straight channels favor the diffusion of the adsorbed drugs in a controlled fashion, which depends on several factors, such as pore size, surface functionalization, and particle morphology, among others. The combination of both properties, compositional and textural, has triggered their use in bone regeneration technologies; these bio-ceramics can be loaded with specific drugs and then implanted in a damaged bone area for local release of the drugs. The reasons for such a high impact of these materials in the field of biotechnological research are based on their properties: (1) their high pore volume, which allows the confinement of a large amount of drug or biologically active species; (2) their large surface area, which means a high potential for drug adsorption; and (3) their well-ordered pore distribution, which favours the homogeneity and reproducibility on the drug adsorption and release stages.



2-3.1 Drug delivery of mesoporous materials

Mesoporous structures can be leading to controlled media for photonic reactions and organic syntheses ^[80-81]. Mesoporous materials with huge surface areas and pore volumes are appropriate media for storage of biological materials, including proteins ^[82]. The major step forward in ordered mesoporous materials as drug delivery systems is the possibility of employing their available channels as drug reservoirs with a novel quality: they can be opened and closed by different triggers, in the so-called stimuli-responsive release systems. Basically, drugs can be encapsulated inside the porous framework and then released when desired. The resulting polymer/drug composite materials usually exhibit slow rates of spontaneous drug release. Upon stimulation, the degradation of the polymer matrix is accelerated, and the release of drug molecules is thereby enhanced. There are several triggers that can activate the release of guest molecules, such as chemicals, temperature, pH, ultrasounds, light or even magnetism.

Lin and co-workers ^[83] attempted to cap the mesoporous channels of MCM-41 matrices with cadmium sulfide nanoparticles to physically block the vancomycin and adenosine triphosphate (ATP) molecules from leaching out. As release trigger agents, they used disulfide bond-reducing molecules to remove the channel caps and therefore release the loaded molecules under a chemical stimulus. Zhu and co-workers reported sonochemical synthesis of mesoporous spheres of calcium silicate hydrate constructed from nanosheets, with extremely high drug-loading capacity ^[84]. Temperature is a stimulus that can be employed to trigger the release of a certain drug from a delivery system. For this purpose, the employment of thermosensitive polymers, such as poly(N-isopropylacrylamide) (PNIPA), that open or close the channels is necessary to release or retain the loaded drug, depending on the surrounding temperature. This approach was used on L-3 phase silicates ^[85] and MCFs using rhodamine 6G ^[86] and ibuprofen ^[87] as model drugs.

The use of pH as a release trigger in stimuli responsive release systems is based on the fact that certain tissues of the body present a pH slightly more acidic than blood or normal tissue, such as tumor or inflammatory tissues. The first time that the pH effect on the molecular release was investigated was using Al-MCM-41 matrices and fluorescein as models ^[88]. Yu and co-workers prepared biocompatible hollow mesoporous silica spheres with preloaded doxorubicin (DOX) for cancer therapy due to extracellular protection and pH-sensitive release ^[89]. A similar imaginative approach was presented by Zink and co-workers, who designed a functional MCM-41 material, where the openings were regulated by supramolecules, which were controlled by pH and competitive binding ^[90]. Coating the surface of SBA-15 tablets with a pH-sensitive polymer, such as hydroxypropyl methylcellulose phthalate, allows the preparation of oral release systems, and therefore it is possible to release drugs in the stomach or in the intestine (different pHs) ^[91]. In a similar way, it is possible to graft to the external surface of a mesoporous matrix a pH-responsive polyethyleneimine/cyclodextrin (PEI/CD) polypseudoroxotane ^[92]. The mesopores of

PEI-modified silica can be filled with a guest molecule (calcein) and then blocked with CD at pH 11. At pH 5.5, the calcein molecules are released by the reversible dethreading of the CDs from the PEI chain.

Ultrasound can be used as an external trigger for the pulsatile release of a certain drug. In a research work carried out by Honma and co-workers, ordered mesoporous silica was modified with poly(dimethylsiloxane) and ibuprofen was released under the stimulus of ultrasound^[93]. An efficient, reversibly operated nanovalve, able to be turned on and off by redox chemistry, was developed by capping the mesopores with a pseudorotaxane^[94-95]. The opening of the valve was stimulated by the addition of an external reducing agent that caused the pseudorotaxane to disassemble and the drug to be released.

As with all the stimuli mentioned above, light is an external stimulus that can cause change and, therefore, a system that responds to this external stimulus can be developed. This was achieved in MCM-41 nanoparticles modified with two azobenzene derivatives that were able to retain dye molecules and then release them upon exposure to light^[96]. Besides, photocontrolled and reversible intermolecular dimerisation of coumarin derivatives attached to the pore outlets of MCM-41 have been employed to uptake, store and release organic molecules^[97]. Fujiwara and co-workers accomplished, for the first time, the photocontrolled reversible release of drug molecules from coumarin-modified MCM-41^[97-98]. In their work, a photoresponsive coumarin derivative was grafted on the pore outlet of Si-MCM-41. Irradiation of UV light longer than 310 nm of wavelength to this coumarin-modified MCM-41 induced the photodimerisation of coumarin to close the pore outlet with cyclobutane dimer. The irradiation to the dimerized-coumarin-modified MCM-41 with shorter wavelength UV light around 250 nm regenerates the coumarin monomer derivative by the photocleavage of cyclobutane dimer, and guest molecules, phenanthrene, included inside are released from the pore void. Additionally, other photoresponsive release systems

have used azobenzene molecules to release drugs from nanoparticles and deliver them inside cancer cells ^[99].

It is seen that stimuli-responsive controlled-release can be achieved by several techniques as stated above, such as light, magnetite, chemical, pH, and temperature, but not all of these techniques can be employed for drug delivery in human body. Photoinduced reversible release system under UV irradiation is also difficult to operate once the drug is inside the body. In addition, UV light can also cause potential damage to human tissue. The pH value and temperature responsive system has been shown variable applications for drug delivery and this technique will be promising due to the varying conditions of human body. Under certain conditions, magnet target will also be a good technique. The introduction of superparamagnetic iron oxide nanoparticles capping mesoporous silica nanorods allowed the materials to be attracted to specific sites of interest and release a drug under external magnetic fields ^[100]. The possibility of selectively targeting the desired organs or tissues inside the body is an important advance in the application of these matrices as biomedical devices. It is also possible to encapsulate magnetic nanoparticles with mesoporous silica microspheres to direct the material with an external magnetic field to release the drug to the specific target ^[101]. Using the same approach, it is also possible to introduce magnetic nanoparticles into the mesoporous channels of MCM matrices and hollow silica spheres by impregnation, oxidation and reduction procedures. Thus, it is possible to increase the iron content and the efficiency of the release system.

Xing et al. ^[102] proposed a dual-stimuli-responsive drug delivery system, with magnetic oriented target and pH-sensitive characters. The materials show highly ordered mesostructure, high pore volume, regular nanoparticle morphology (500 nm), and superior magnetic property. The pH-sensitive magnetic mesoporous silica nanoparticles (MMSNs) was served as a drug carrier, with ibuprofen (IBU) being the model drug. Yu et al. studied a facile synthesis to prepare Iron oxide/MCM-41 hybrid nanospheres with a large surface area

of $1334 \text{ m}^2 \text{ g}^{-1}$ and a uniform diameter of 85 nm have been synthesized via a facile sol-gel route ^[103]. The hybrid presents a ferromagnetic property that ensures them a fast response to an applied magnetic field. Moreover, they are proven to be beneficial for loading an anticancer drug-doxorubicin hydrochloride (DOX), because a considerable loading content of 6.0% and a high entrapment efficiency of 90.5% have been achieved. Yang and co-worker ^[104] published that hydrothermally synthesized Fe_3O_4 microspheres have been encapsulated with nonporous silica and a further layer of ordered mesoporous silica through a simple sol-gel process. The surface of the outer silica shell was further functionalized by the deposition of $\text{YVO}_4:\text{Eu}^{3+}$ phosphors, realizing a sandwich structured material with mesoporous, magnetic and luminescent properties. The emission intensities of Eu^{3+} in the drug carrier system increase with the released amount of drug, thus making the drug release be easily tracked and monitored by the change of the luminescence intensity. Zhu et al. ^[105] developed a site-selective controlled delivery system for controlled drug release that fabricated through the in situ assembly of stimuli-responsive ordered SBA-15 and magnetic particles. In vitro testing of IBU loading and release exhibits a pronounced transition at around 32°C , indicating a typical thermosensitive controlled release. Different from the two phase, Guo et al. ^[106] report a facile, gram-scale, low-cost route to prepare monodisperse superparamagnetic single-crystal magnetite NPs with mesoporous structure (MSSMN) via a very simple solvothermal method. It is also interestingly found that the size and morphology of mesoporous Fe_3O_4 NPs can be easily controlled and can be used as an effective drug delivery carrier. It is found that Dox molecules could be stored in the MSSMN with an uptake amount of 40 mg g^{-1} . The drug release rates are also suitable for drug delivery application, and most of the drug molecules incorporated could be released to solution in 12 h. In addition, Magnetic mesoporous carbonated hydroxyapatite microspheres have been fabricated hydrothermally by using $\text{CaCO}_3/\text{Fe}_3\text{O}_4$ microspheres as sacrificial templates ^[107]. The high drug-loading capacity and sustained drug release property suggest that the

multi-functionalized microspheres have great potentials for boneimplantable drug-delivery applications. For example, the possible mechanism of the drug release profile from the ferrogel is schematically illustrated in Figure 2.10. In the beginning when there is no magnetic force (MF), the magnetic (fields) moments existing in the ferrogel are randomly oriented. The ferrogel is subjected to zero magnetization and the drug release profile displays a normal diffusion mode. While applying MF, the magnetic moments of the particles tend to align with the magnetic fields and produce a bulk magnetic moment. This induces the Fe_3O_4 particles within the ferrogel to aggregate together instantly, leading to a rapid decrease in the porosity of the ferrogel, where the ferrogel was characterized as a “close” configuration. In other words, while the imposed field induces magnetic dipoles, mutual particle interactions occur if the particles are so closely packed that the local field can influence their neighbors. The particles attract with each other when aligned in an end-to-end configuration and thus a “pearl-chain structure” was developed ^[108] due to the attractive forces that reduced the pore size of the ferrogel. Therefore, the drugs are restrictedly confined in the network of the ferrogel, causing a rapid and significant reduction in the diffusion of the drug through the ferrogel. While turning off the field, the pores in the membrane re-open instantly, which correspondingly results in a rapid re-filling of the drug-containing solution into the membrane, drug solution as both residual amount and later re-filled was released instantly at the moment of pore re-opening, resulting in a burst-like profile; however, the release turned back to normal diffusion profile shortly after the burst ^[109].

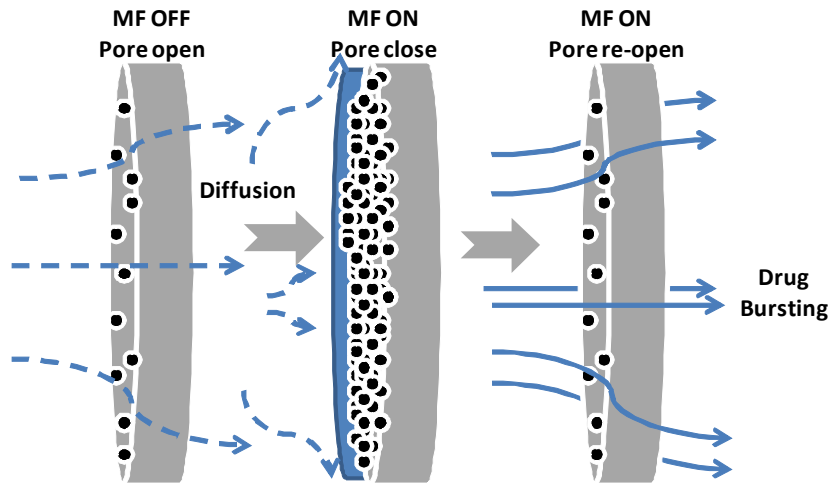


Figure 2. 10 Mechanism of “close configuration of the ferrogels due to the aggregation of Fe_3O_4 nanoparticles under “on” magnetic fields causes the porosity of the ferrogels to decrease.



2-3.2 Bioactivity and release system of mesoporous materials

It was well-known that mesoporous materials can play a double role: bioactivity and release systems for biologically active species. In the near future, it could be possible to combine both aspects thanks to the design of novel bioceramics with the added value of delivery systems. Biodegradability and biocompatibility are the fundamental requirements that determine the possible therapeutic and surgical applications of a polymeric biomaterial. Gomez-Vega et al. ^[110] first investigated the bioactivity of mesoporous silica films coated on Ti6Al4V. When tested in SBF, these coatings induced apatite formation after 7 days. Giri et al. ^[100] also investigated the biocompatibility of magnet/MSN stimuli-responsive controlled-release system with HeLa (human cervical cancer) cells. The appearance of healthy intact nuclei and the visibility of fully grown cells by transmission suggested that the magnet/MSN systems are biocompatible with HeLa cells in vitro under the experimental conditions. Previous research found that the bioactivity of silica-based ceramic materials is strongly dependent upon the phosphorous content of the glass. Thus, Vallet-Regi ^[111] investigated the bioactivity of MCM-41 mesoporous material doped with phosphorous. In

the in vitro tests, the material revealed a bioactive response only after 13 days of assay. Another strategy used in order to increase the bioactivity process is the preparation of biphasic mixtures, in which one phase acts as apatite nucleation sites, accelerating the process. Andersson et al. ^[112] reported a degradable, hierarchically porous silica/apatite composite material for drug delivery. The composite is suitable as bone filler material, and a localised, controlled drug release from osteoconductive implant. Onida et al. ^[113] reported the synthesis of an ordered mesophase within a macroporous glass-ceramic, in order to combine the bioactivity of the latter with the release properties of ordered mesoporous systems. It is demonstrated that mesoporous silicas, MCM-41, MCM-48 and SBA-15, are bioactive materials if used as substrate for drug delivery system. However, the biocompatibility is not so strong. Modification with phosphorous or active component such as apatite will significantly improve their biocompatibility.

In the past few years, the biomedical research area has shown a growing interest in ordered mesoporous materials because of their promising applicability in the context of drug delivery and tissue engineering, especially in bone tissue regeneration. The combination of both properties, compositional and textural, has triggered their use in bone regeneration technologies ^[114]; these bioceramics can be loaded with specific drugs and then implanted in a damaged bone area for local release of the drugs. The main role of bone formation must be played by specific living cells, which present dimensions of the order of hundreds of nm. Taking into account that mesoporous channel diameters range between 2 and 50 nm, it is obvious that cells need larger pores to attach into them. Consequently, the challenge then is to obtain scaffolds combining macroporosity for bone oxygenation and vascularisation, and mesoporosity for applications where drugs or biologically active molecules are loaded and then released.

Vallet-Regí and co-workers ^[115] synthesized mesoporous silica-zirconia mixed oxides with tunable acidity via spraydrying process as controlled release vectors of isphosphonates

for bone implant technologies. Gomez-Vega and co-worker ^[116] prepared mesoporous silica coatings using self-assembling organicyinorganic sol-gel systems. The resulting mesoporous silica coatings were able to induce apatite formation after 1 week of immersion in a simulated body fluid in physiological conditions, which is a sound indication of a bioactive behavior when tested in vivo. These results indicate that the coatings prepared by the methodology described in this work may be valid candidates to be used on implants. Perez et al. ^[117] reported a new type of implantable drug eluting device, consisting of a bed of mesoporous microparticles packed inside a reservoir with a porous wall. This provides two sets of variables for drug release control that can be tailored independently. Ehlert et al. ^[118] reported the material where a sulfonate-functionalized mesoporous silica layer is loaded with ciprofloxacin and then coated by an organosiloxane layer derived from bis(trimethoxysilyl)hexane showed the best results with regard to antibacterial efficacy and will further be tested in animal experiments. Li et al. ^[119] reported the mesoporous amorphous calcium silicate (MACS) using mesoporous silica SBA-15 as both the template and silicon source, and $\text{Ca}(\text{NO}_3)_2$ as the calcium source. In vitro bioactivity studies of the MACS were carried out by soaking it in simulated body fluid (SBF) solutions for 4 h up to 5 days. The MACS did develop a carbonatecontaining hydroxyapatite (HCA) layer on the surface after being immersed in SBF for 4 h with near-spherical agglomerated hydroxyapatite (HA) nanoparticles.

Common coating materials suggested for improving bioactive properties of implant materials include crystalline titanium dioxide and calcium phosphate based coatings or surfaces. However, suggested methods for improved bioactivity cannot completely eliminate the risk of obtaining infections at the implant surface. Many publications are concentrated with fabricating different roughness and specific topography of biomaterials' surfaces aimed to improve cytocompatibility of the surface. To improve the bioactivity, many surface modifying techniques, such as sol-gel coating ^[120], plasma spraying ^[121] and

electrochemical deposition ^[122], have been developed to prepare the bioactive coating on Ti alloys. Recently, many attentions have been paid to the mesoporous structure characterized having large surface area, large pore volume, and a pore size distribution among 2-50 nm. Macropores can facilitate tissues in growth and nutrient delivery to the center of their regenerate tissue. A series of mesoporous materials, such as MCM-48, SBA-15 and phosphorous-doped MCM-41, has been demonstrated that they can induce a bone-like apatite layer on their surfaces ^[123]. In vitro bioactivity is assessed by measuring the apatite forming rate in a simulated body fluid (SBF) solution, which contains inorganic ions in concentrations corresponding to those in human blood plasma. The formed apatite has several characteristics similar to the apatite in bone tissue, and is thought to be formed by an inorganic chemical reaction in vitro similar to that occurring in the bone tissue. Tang et al. ^[124] prepared the mesoporous titania films (MTFs) on Ti₆Al₄V substrates by the evaporation-induced self-assembly (EISA) process. The results showed that the MTFs have a high bone-forming ability, and is a promising method for improving the bioactivity of Ti alloys. Guo et al. ^[125] developed mesoporous titania coatings (MTCs) with a pore size of 4.75 nm on Ti₆Al₄V substrates by a sol-gel process, and then irradiated with UV light at room temperature for 2 h. The results indicate that the MTCs before and after UV irradiation exhibit a good biocompatibility and are fit for the MG63 cell proliferation. Xia et al. ^[126] reported mesoporous titanium dioxide coating for metallic implants. The bioactive mesoporous titanium dioxide (MT) coating for surface drug delivery has been investigated to develop a multi-functionalized implant coating, offering quick bone bonding and biological stability. Jiang and co-worker ^[127] reported Hierarchical porous TiO₂-bioglasses (TiO₂-BGs) with the macropore with the size of 30-50 μm and the mesopore with the diameter of 4.4-5.6 nm through the evaporation-induced self-assembly method. It took only 3 h for the TiO₂-BGs to be covered with the hydroxyapatite layer.

Chapter 3

Synthesis, Characterization, and CO₂ Adsorptive Behavior of Ordered Mesoporous AlOOH-Supported Layered Hydroxides

3-1 Introduction

Recently, CO₂ emission has become a serious problem because it has resulted in global warming and serious climate change due to the combustion of fossil fuels, which releases CO₂ into the environment when used for power plants. Therefore, it is now widely recognized as important to control CO₂ emissions. Several options have been proposed to reduce the emission of CO₂, including the substitution of nuclear power for fossil fuels, increasing the efficiency of fossil plants, substitution of natural gas for coal, and the capture and separation of CO₂ prior to emission into the environment [128-130].

Among the above-mentioned methods, CO₂ capture and storage from fossil-fuel power plants are becoming important in mitigating the long-term impact because high temperature synthesized gas (around 450-700 °C) was involved in the sorption-enhanced hydrogen production process and gasification plants with integrated gasification combine cycle (IGCC) [131]. Therefore, it is highly desirable to absorb CO₂ at high temperatures without cooling to room temperature, which makes the overall processes more feasible and more economic. In this case, a sorbent with high sorption capacity, long-term durability, rapidly adsorption/desorption rate and good mechanical strength properties plays an important role in the economic viability of CO₂ capture systems. Up to now, various solid sorbents for CO₂ capture at high temperature have been reported in the synthetic materials, including metal oxides sorbents such as calcium based sorbents [132-136], alkali ceramic based sorbents [137-138] and hydrotalcite-like compounds (HTlcs, also known as layered double hydroxides (LDHs) such as Mg-Al LDH or Ca-Al LDH [139-141]. The crystal structure of typical LDHs is shown in Appendix-2.

It is well known that CaO-based solid sorbent has been used as the first choice for CO₂ capture because it exhibits high adsorption capacity and low cost, but it still shows poor durability after several cycles for CO₂ adsorption/desorption cycles due to the sintering and aggregation of the CaO and CaCO₃ during the adsorption/desorption process, particularly CaCO₃ at high calcination temperatures (greater than 800 °C). To overcome the loss-in-capacity, many methods have been proposed for calcium oxide derivatives, such as sintering-resistant sorbents. For examples, Li and Wu reported that the CaO/Al₂O₃ sorbent has better resistance properties as a CO₂ sorbent than nonaluminum CaO-based particles [142-143]. Martavaltzi and Lemonidou prepared a CaO/Ca₁₂Al₁₄O₃₃ sorbent with a maximum conversion ratio of 85% after 45 cycles because the calcium aluminum oxide (Ca₁₂Al₁₄O₃₃) provides a stable framework that inhibits the deactivation of CaO [144].

On the other hand, in the past few years, LDHs have found potential use as sorbents that efficiently take up CO₂ at higher temperatures and dramatically improve the adsorptive capacity of CO₂. For instance, Hao et al. studied various LDHs with different divalent cations, including Mg²⁺, Co²⁺, and Ca²⁺, and reported the CaCoAlO system has the highest CO₂ captures of 1.39 mmol_{CO2} g_{sorbent}⁻¹ at 350 °C and 1 atm in a fixed-bed reactor within 20 min [145]. Luo et al. systematically studied a series of Mg-M-CO₃ (M=Al, Fe, Ga, Mn, and others) LDHs for CO₂ adsorption and suggested that the M³⁺ influences the CO₂ capture capacity of LDH derivatives, and the maximum CO₂ capture occurred at ~200 °C for all LDHs [146]. Wang et al. reported that the anions (CO₃²⁻, NO₃⁻, SO₄²⁻, and Cl⁻) have great effect on the thermal stability and morphology, as well as on the surface area of Mg-Al hydrotalcites (HTs), consequently influencing the CO₂ adsorption capacity of HT derivatives [147].

However, according to the literature, there is no systematical investigation of mesoporous LDHs on CO₂ adsorption at high temperature because mesoporous materials are characterized as having high surface area, pore volume, and pore size, with a narrow

pore diameter distribution ^[147]. Recently, although Mg-Al-LDH mesoporous materials have been synthesized for catalysis or CO₂ capture, the adsorption temperature was too low to be applied for CO₂ capture at high temperature (500-700 °C) and the capture capacity is also very small ^[146,149]. Therefore, in exploring porous sorbents with high adsorptive capacity and durability, mesoporous oxides such as alumina and silica as the support for CaO-based sorbents become more important but only few studies have been conducted on CaO-based CO₂ sorbents. For this reason, mesoporous alumina was considered as advanced supports and sorbents because of its good thermal and chemical stability and high mechanical modulus ^[150-152].

In this article, a novel ordered mesoporous metal oxide material was prepared by calcining a mesoporous AlOOH-supported Ca-Al-LDH precursor which was synthesized by using mesoporous Al₂O₃ and CaCl₂ as directive agents via the hydrothermal urea reaction. The structural characteristics, morphology and formation mechanism of the novel mesoporous solid material were evaluated by using X-ray diffraction (XRD), Brunauer-Emmett-Teller (BET) measurements, scanning electron microscopy (SEM), and transmission electron microscopy (TEM). Moreover, the mesoporous metal oxide materials were also examined as a potential solid sorbent for CO₂ capture at high temperature. A detailed discussion on the high-temperature CO₂ adsorptive behavior and characterization of the solid sorbent was made based on thermogravimetric analysis (TGA). Furthermore, the developed mesoporous oxide displayed a rapid adsorption rate, high capture capacity, and excellent multiple-cyclic capture stability.

3-2 Experiments

3-2.1 Synthesis of mesoporous metal oxides

According to a previous study ^[153], Yuan and co-workers reported highly ordered mesoporous alumina (MA) with high thermal stability. In a typical preparation, triblock

copolymer HO(CH₂CH₂O)₂₀-(CH₂CH(CH₃)O)₇₀(CH₂CH₂O)₂₀H (2 g; Aldrich, Mn= ≈ 5,800, Pluronic P123) was dissolved in absolute ethanol (20 mL; Sigma-Aldrich, 99.5%) and stirred for 4 h at RT. In another solution, aluminum isopropoxide (AIP, ≈ 20 mmol; Aldrich, +98 wt.%) was dissolved in nitric acid (3.2 mL; J.T Baker, 70 wt.%) and absolute ethanol (10 mL). Then, the AIP solution was slowly added to the surfactant solution, and the mixed solution was vigorously stirred for 5 h at RT and then transferred to an oven to evaporate the solvent at 60 °C for 3 d. The resulting powder (denoted M-AlOOH) was calcined at 700 °C for 4 h with a heating rate of 5 °C min⁻¹ in an air flow and then cooled in a furnace to ambient temperature to give MA.

MA-supported CaAl LDH (LDH/MA) was fabricated by hydrothermal urea reaction using the following precursors: synthesized MA, calcium chloride dihydrate (CaCl₂ · 2H₂O; Riedel-de Haën, 99 wt.%), and urea [(NH₂)₂CO; Merck, 99.5 wt.%] as the directing agent. In a typical procedure, CaCl₂ · 2H₂O powder was dissolved in deionized water and stirred for 30 min. Subsequently, this solution was added to the previously prepared MA suspension in an aqueous medium containing 0.5M urea in excess and stirred for 30 min at RT. The molar Ca/Al/(NH₂)₂CO ratio of the final solution was 3:1:10. The mixed solution was transferred to an autoclave and heated at 150 °C for 3 d in an oven. After the hydrothermal urea reaction, the precipitate was centrifuged, washed with ethanol/deionized water, and dried at 60 °C for 24 h. The resulting powder was calcined at 700 °C for 1 h with a heating rate of 10 °C min⁻¹ in an air flow and then cooled in a furnace to ambient temperature to give the mesoporous CaAl metal oxide (M-CaAl).

3-2.2 Characterization of mesoporous metal oxides

The resulting powders were characterized by performing XRD measurements (MAC Science MXP18AHF XRD, with CuK_α radiation source, λ=1.5418 Å). Nitrogen sorption measurements at 77 K were conducted by using a Micromeritics ASAP 2010 system. The

pore diameters of samples were determined by means of the Barrett-Joyner-Halenda (BJH) method on the basis of desorption branches of nitrogen isotherms. All samples were degassed under vacuum at 200 °C for 2 h prior to the measurement. SEM images of the sample were collected by using a JEOL-6700 field-emission electron microscope at an accelerating voltage of 15 kV. TEM micrographs and electron diffraction patterns were recorded by using a JEOL JEM-2100F electron microscope equipped with an Oxford energy-dispersive spectrometer (EDS) analysis system. Elemental Ca or Al distribution mapping was conducted by using a TECNAI 30 electron microscope fitted with an electron energy loss spectroscopy (EELS) detector. Samples for TEM measurements were embedded in resin and ultramicrotomed into slices with thicknesses of about 50 nm. Thermogravimetric analysis (TGA, TA Instrument Q500) was used to investigate the CO₂ adsorption properties of the calcined mesoporous CaAl metal oxide samples. The heating rate was 10 °C min⁻¹, and the calcined sample was maintained at a high temperature for 30 min under nitrogen and was then carbonated by pure CO₂ gas with a flow rate of 60 mL min⁻¹ (CO₂ partial pressure at 40 kPa) at different temperatures (200-800 °C) for 2 h. The adsorption capacity (C_{ads.}, wt.%) was defined according to the below Equation:

$$C_{\text{ads.}} (\text{wt.}\%) = [\text{weight of CO}_2/\text{weight of calcined sample}] \times 100$$

Additionally, CO₂ adsorption capacity was carried out in a fixedbed reactor, namely, a quartz tube reactor 0.8 mm in diameter. A small amount of calcined sample (~0.165 g) with particle sizes of 0.2-0.5 mm and quartz wool were installed in the reactor and placed into a furnace equipped with a temperature controller. Adsorptive experiments were carried out at 600 °C for 1 h under CO₂ gas with a flow rate of 60 mL min⁻¹ (partial pressure of 40 kPa). Online chemical analysis of CO₂ and nitrogen at the exit of the reactor was achieved by using a gas chromatograph (Agilent 7890A). Nitrogen was used as the internal standard (flow rate of 10 mL min⁻¹). The below Equation was used to calculate the capacity of the calcined sample ^[154]:

$$N_{\text{CO}_2} = \int_0^{t_1} (F_{\text{CO}_2, \text{tot}} - F_{\text{CO}_2, t}) dt$$

in which $F_{\text{CO}_2, \text{tot}}$ indicates the average value of CO_2 flow rate during saturation; $F_{\text{CO}_2, t}$ represents the CO_2 flow rate at time t ; and t_1 represents the time point at which the CO_2 content in the gas effluent does not increase. The CO_2 adsorption/desorption cycles of the mesoporous M-CaAl were collected by means of TGA and in CO_2 (adsorption 700°C for 10 min in pure CO_2 gas and then desorption at another 8 min in N_2 gas with a flow rate of 60 mL min^{-1}). The cycles were repeated 30 times.

3-3 Results and discussion

3-3.1 Characteristics of mesoporous metal oxides

Small-angle XRD (SA-XRD) patterns of MA, LDH/MA, and CaAl metal oxide (M-CaAl) are illustrated in Figure 3.1(a), where the characteristic reflections of the $p6mm$ hexagonal structure at $2\theta = 0.79^\circ$ (MA), 0.77° (LDH/MA), and 0.818° (M-CaAl) are displayed and the corresponding spacing (d spacing) is indexed with $d_{100}=11.18$, 11.47 , and 10.9 nm , respectively. A hexagonal unit cell parameter (a_0) of 12.9 (MA), 13.24 (LDH/MA), and 12.58 nm (M-CaAl) was calculated by assuming a (100) reflection of the hexagonal array of pores of the mesoporous metal oxides. It is indicative of mesostructure formation. This finding also indicates that the hexagonal arrangement of the mesoporous structure evolved upon mesoporous-metal-oxide synthesis. Large-angle XRD (LA-XRD) patterns of the mesoporous metal oxides are shown in Figure 3.1(b). After calcination at 700°C , MA displays three broad peaks of the (311), (400), and (440) reflections, which corresponded to those of crystalline $\gamma\text{-Al}_2\text{O}_3$ (JCPDS no. 29-1486), indicating a crystalline $\gamma\text{-Al}_2\text{O}_3$ framework. Moreover, after the MA and calcium precursor reacted in the hydrothermal urea method, the diffraction peaks of the LDH/MA sample exhibited a typical HT-like phase with diffraction peaks at $2\theta = 11.62^\circ$ ($d_{003} = 0.762 \text{ nm}$) and 22.978° ($d_{006} = 0.387 \text{ nm}$), which

corresponded to the basal planes of (003) and (006). It also indicated a well-developed crystalline layered structure with rhombohedral symmetry; in addition, strong diffraction peaks of CaCO_3 (JCPDS no. 01-0837) were observed at $2\theta = 23.00^\circ$ ($d_{012} = 0.387$ nm), 29.48° ($d_{104} = 0.302$ nm), 47.35° ($d_{024} = 0.192$ nm), and 65.38° ($d_{300} = 0.143$ nm). It is suggested that the calcium precursor may rapidly react with the aqueous urea solution, which dissociates to produce CO_3^{2-} during hydrothermal treatment to form CaCO_3 precipitates on the MA surface. In addition, weak diffraction peaks of AlOOH (JCPDS no. 17-0940) appeared at $2\theta = 14.48^\circ$ ($d_{020} = 0.611$ nm), 28.24° ($d_{120} = 0.316$ nm), 38.31° ($d_{031} = 0.234$ nm), 46.1° ($d_{131} = 0.196$ nm), and 49.38° ($d_{200} = 0.185$ nm). This structure corresponds to an orthorhombic unit cell. The diffraction peaks were indexed by using the space group Cmcm . During the urea treatment, $\gamma\text{-Al}_2\text{O}_3$ is transferred to boehmite until the thermal treatment was applied to induce the phase transition. As the mesoporous LDH/MA was calcined at 700°C , M-CaAl nanoparticles formed. The LA-XRD patterns of the mesoporous metal oxides were characterized, corresponding to the crystalline structures of $\gamma\text{-Al}_2\text{O}_3$ (JCPDS no. 29-1486), $\text{Ca}(\text{OH})_2$ (JCPDS no. 01-1079), CaAl_4O_7 (JCPDS no. 23-1037), and $\text{Ca}_{12}\text{Al}_{22}\text{O}_{33}$ (JCPDS no. 09-0413). The $\gamma\text{-Al}_2\text{O}_3$ peak intensity is weak because most of the $\gamma\text{-Al}_2\text{O}_3$ has reacted with CaO to form M-CaAl. In addition, $\text{Ca}(\text{OH})_2$ was identified due to the sensitivity of CaO to water gas. Therefore, we use $\text{Ca}(\text{OH})_2/\text{CaO}$ to avoid confusion.

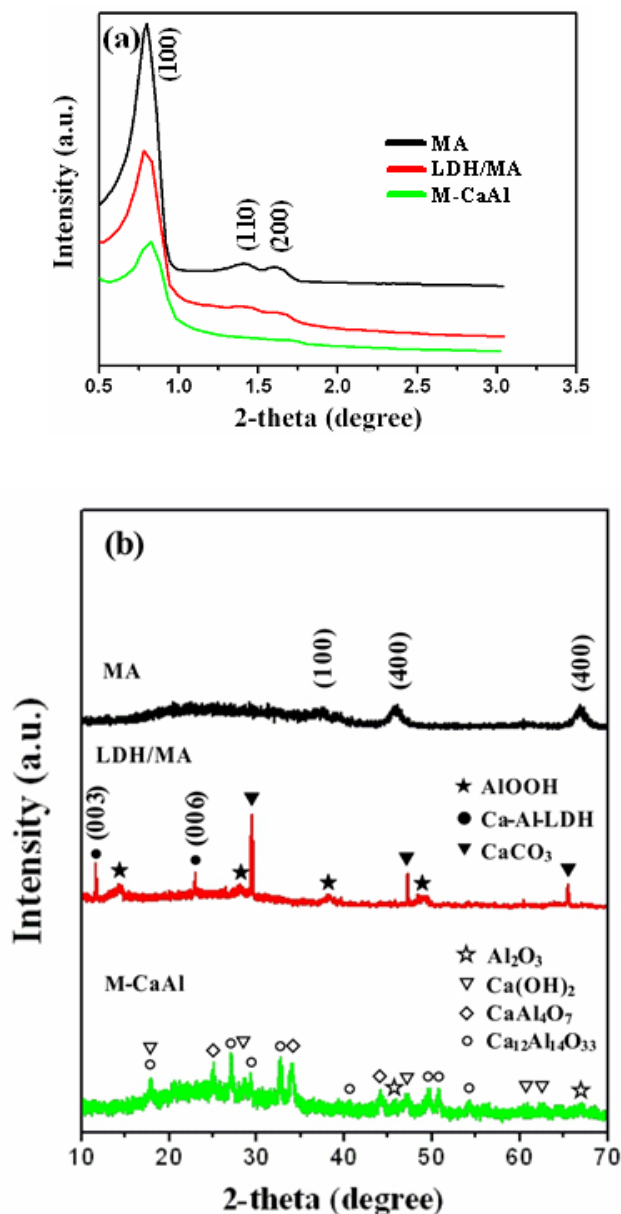


Figure 3. 1 (a) small-angle XRD patterns^[172], (b) large-angle XRD patterns of the MA, LDH/MA, and M-CaAl samples.

Nitrogen adsorption isotherms and the corresponding pore size distribution of the mesoporous metal oxides are shown in Figure 3.2. The isotherms can be classified as type IV, indicating typical mesoporous metal oxides^[155]. The hysteresis loop of MA or M-CaAl displays type H1 characteristics, and the steepness of the capillary condensation step indicates the uniformity of the mesopores. On the other hand, the LDH/MA sample shows a hysteresis loop of type H2, which is typical for wormhole-like mesostructures and

hierarchical scaffold-like mesoporous structures^[156-157]. Some typical textural parameters of the MA, LDH/MA, and M-CaAl samples were BET surface areas of 285, 192, and 273 m² g⁻¹; pore volumes of 0.6, 0.38, and 0.48 cm³ g⁻¹; and pore size distributions of 7.1, 4.7, and 6.2 nm, respectively. Therefore, in the LDH/MA sample after loading the calcium precursor, the presence of CaCO₃ particles restricted the amount of nitrogen adsorbed, as indicated by the smaller BET surface area and pore volume. Also, in this case, the reduced apparent porosity can only be explained by partial blocking of the mesopore system; in addition, the calcined sample (M-CaAl) with a larger BET surface area and pore volume was probably due to decarbonation of CaCO₃ to produce smaller CaO particles. The large surface area and large pore volume may enhance the potential applications of these mesoporous metal oxide materials in CO₂ capture at high temperature.

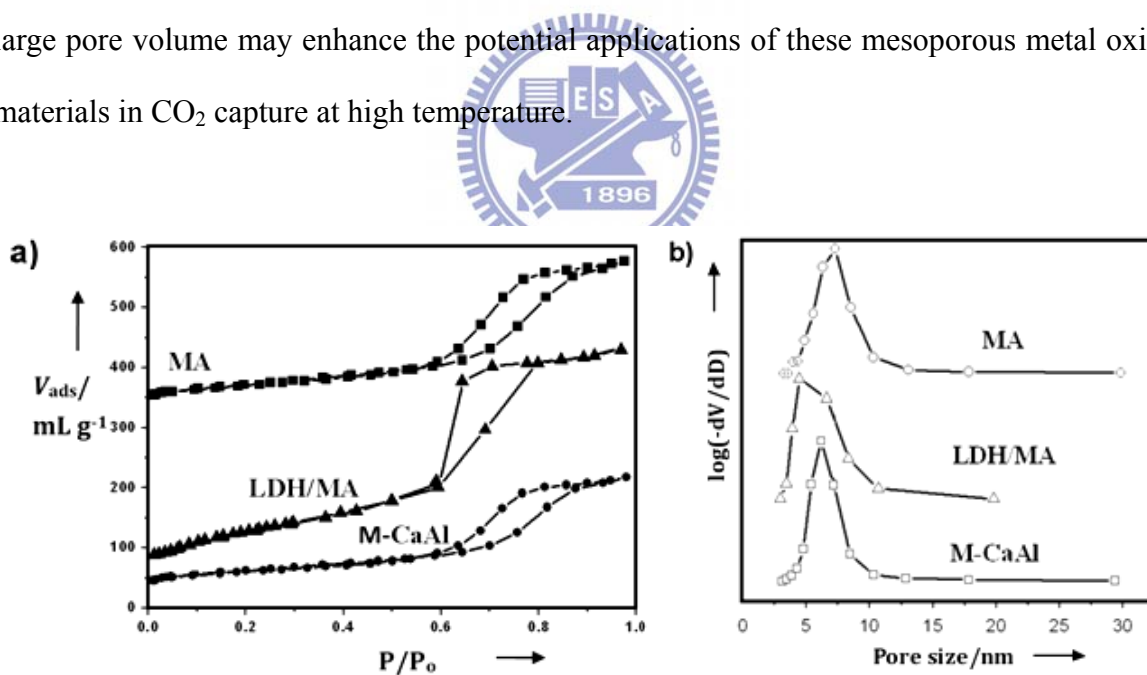


Figure 3. 2 (a) N₂ adsorption isotherms of the MA, LDH/MA, and M-CaAl samples and (b) the corresponding pore size distribution.

An SEM image of the M-AlOOH sample prepared by evaporation-induced self-assembly is shown in Figure 3.3(a), which displays a crystal-like morphology with particle sizes of 0.2-1.5 μm . After loading calcium, the surface morphologies of the LDH/MA and M-CaAl samples are shown in Figure 3.3(b) and (c), respectively. The morphologies of the LDH/MA sample exhibit a flake-like shape with a particle size

distribution in the range of 100-300 nm and a thickness of about 20 nm. According to the powder XRD results shown in Figure 3.1(b), the LDH/MA sample mainly consists of CaCO_3 , an HT-like compound (CaAl LDH), and AlOOH . It should be noted that CaCO_3 displays mainly strong diffraction peaks and is assumed to be precipitated on the surface of LDH/MA during the hydrothermal urea reaction. Furthermore, after the LDH/MA sample has been calcined at 700 °C for 1 h, the M-CaAl sample exhibits uniform spherical nanoparticles with a particle size of 20-40 nm. Conversely, CaCO_3 crystals decomposes at high temperature to form CaO nanoparticles on the surface of M-CaAl ^[158-159], where the presence of $\text{Ca}(\text{OH})_2$ in Figure 3.1(b) is ascribed to the reaction of moisture in the air with CaO.

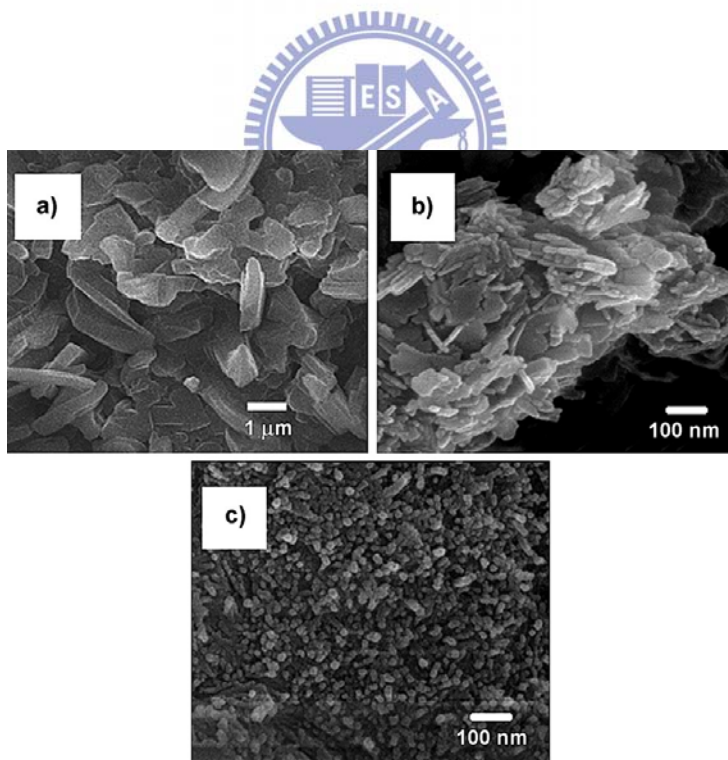


Figure 3. 3 The SEM images of (a) the synthesized M-AlOOH, (b) LDH/MA, and (c) M-CaAl samples.

TEM and energy-dispersive spectrometry (EDS) analyses of the LDH/MA sample are given in Figure 3.4, for which two different domains are observed. The first domain displays a large number of disordered mesoporous metal oxide nanotubes with lengths of 50-200 nm (Figure 3.4 (a)). The second domain in Figure 3.4(d) exhibits channels with 2D

hexagonal symmetry (p6mm) along [110] with an interplanar space calculated to be 10.5 nm, which is in good agreement with that determined by means of SA-XRD (11.47 nm). It is possible that the disordered metal oxide nanotubes may split from the ordered mesoporous arrays after the hydrothermal urea reaction. The high-resolution TEM (HR-TEM) image (inset of Figure 3.4 (a)) depicts an individual nanotube with an average width of about 9.5 nm. In addition, some large crystals are observed in Figure 3.4(b), and HRTEM examination from the lattice image of CaCO₃ (inset of Figure 3.4(b)) clearly shows that the estimated value of $d_{012} = 0.39$ nm corresponds to $d_{012} = 0.387$ nm of the (012) peak of CaCO₃ in LA-XRD because CaCO₃ is formed according to the following reactions: $\text{NH}_4\text{CNO}(\text{urea}) + 2\text{H}_2\text{O} \rightarrow 2\text{NH}_4^+ + \text{CO}_3^{2-}$ and $\text{Ca}^{2+} + \text{CO}_3^{2-} \rightarrow \text{CaCO}_{3(s)}$ [160]. Compositional analysis of the mesoporous metal oxides examined by means of EDS is shown in Figure 3.4(c) for disordered mesoporous metal oxide nanotubes (spot 1 in Figure 3.4(a)) and a large crystal (spot 2 in Figure 3.4(b)). EDS analysis performed on spot 1 reveals that the nanotubes consisted of a large amount of Al and O and a small amount of Ca, but that the large crystal was mainly composed of Ca. According to the LA-XRD and EDS results, Ca²⁺ may easily react with mesoporous $\gamma\text{-Al}_2\text{O}_3$ after hydrothermal urea treatment to form CaAl LDHs, indicating that Ca²⁺ uniformly diffuses into the mesoporous AlOOH framework to obtain the mesoporous AlOOH-supported CaAl LDHs. The CaAl LDHs with crystalline nanoplatelets could be formed on the inner or outer surface of the mesoporous AlOOH nanotubes in Figure 3.4(e), with nanosized platelets of 3-30 nm.

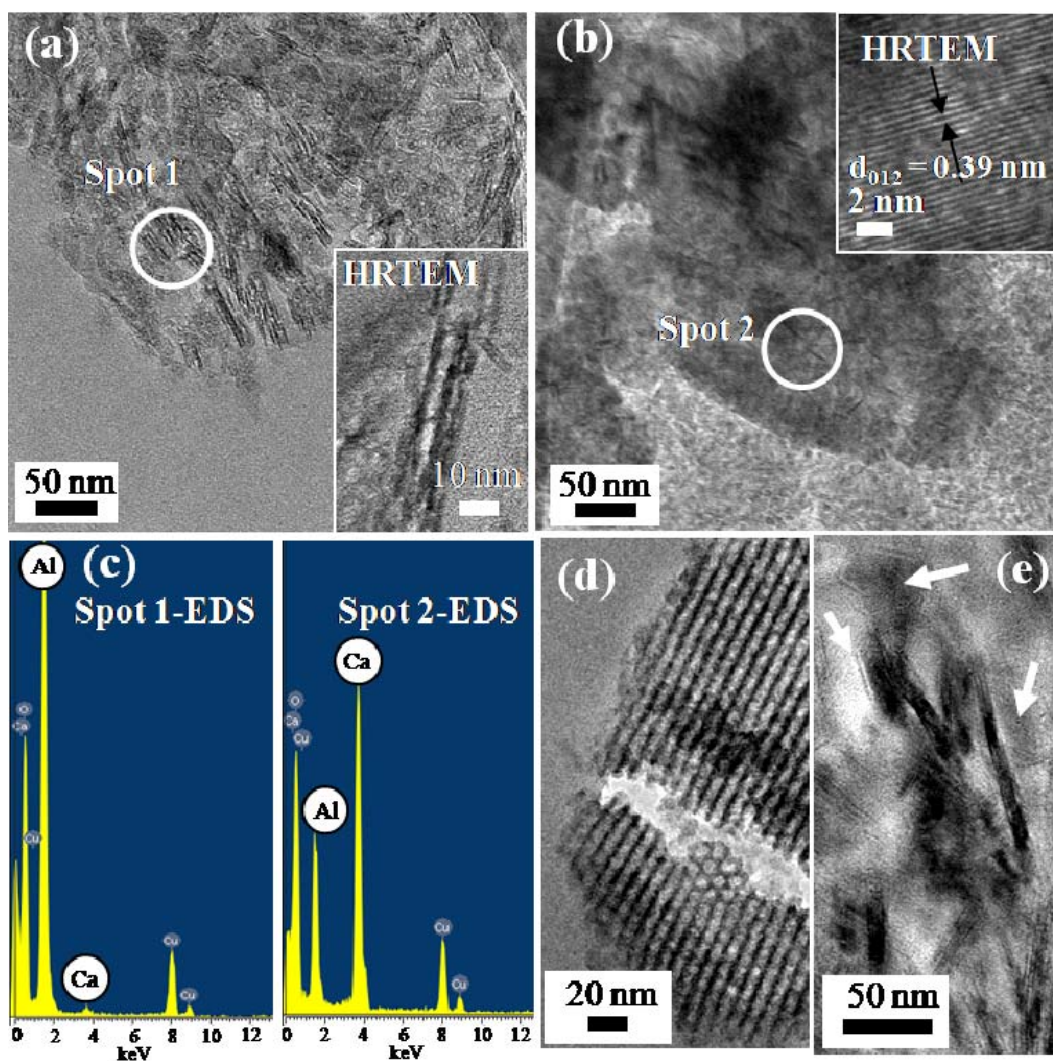


Figure 3. 4 (a), (b), (d), (e) the TEM images and (c) EDS analysis of the LDH/MA sample.

Furthermore, TEM, electron energy loss spectroscopy (EELS) mapping, FT diagrams, and selected-area electron diffraction (SAED) patterns were used to characterize the crystalline structure and element distribution of calcined M-CaAl (Figure 3.5). The M-CaAl sample showed an ordered mesoporous network with hexagonal-like arrays along [100] (Figure 3.5(a)); the pore size was about 6.8 nm, corresponding to a pore size distribution of 6.2 nm in the nitrogen-adsorption isotherm. HRTEM results (Figure 3.5 (e)) clearly show the lattice image of the mesoporous configuration of the metal oxide with a highly crystalline framework; the lattice spacing was estimated to be $d_{131} = 0.23$ nm, corresponding to $d_{131} = 0.26$ nm of the (-131) peak of CaAl_4O_7 in LA-XRD. The inset FT

diagram in Figure 3.5(e) indicates a single-crystalline structure. In addition, the two EELS mapping images for Ca (Figure 3.5(b)) and Al (Figure 3.5 (c)) were overlapped (Figure 3.5(d)); the resulting map clearly indicated that the Ca atoms were homogeneously dispersed in the Al matrix. However, some metal oxide nanotubes were also inspected, and the results are shown in Figure 3.5(f). The SAED pattern in the inset of Figure 3.5(f) clearly displays the polycrystalline structure of the nanotubes, implying that, as the M-CaAl LDHs calcined at high temperature, a solid solution or mixture of phases composed of CaAlO evolved from the single-crystalline framework to form calcium aluminum oxides.

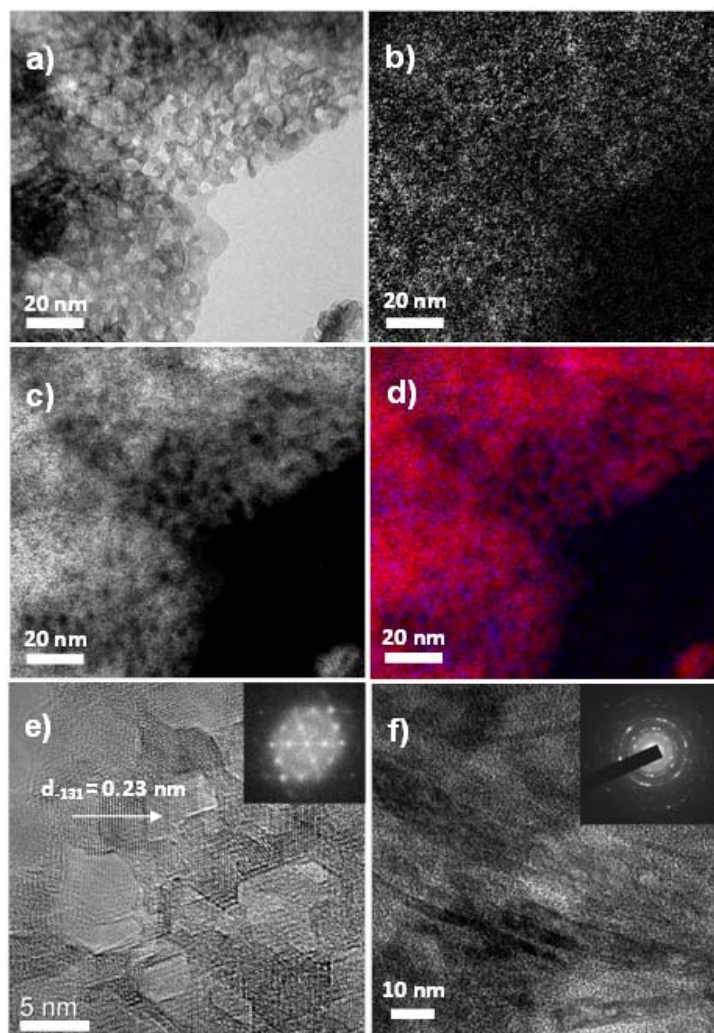
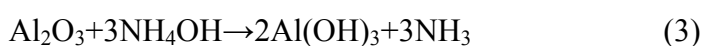
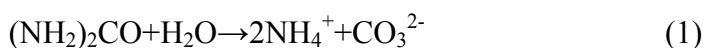
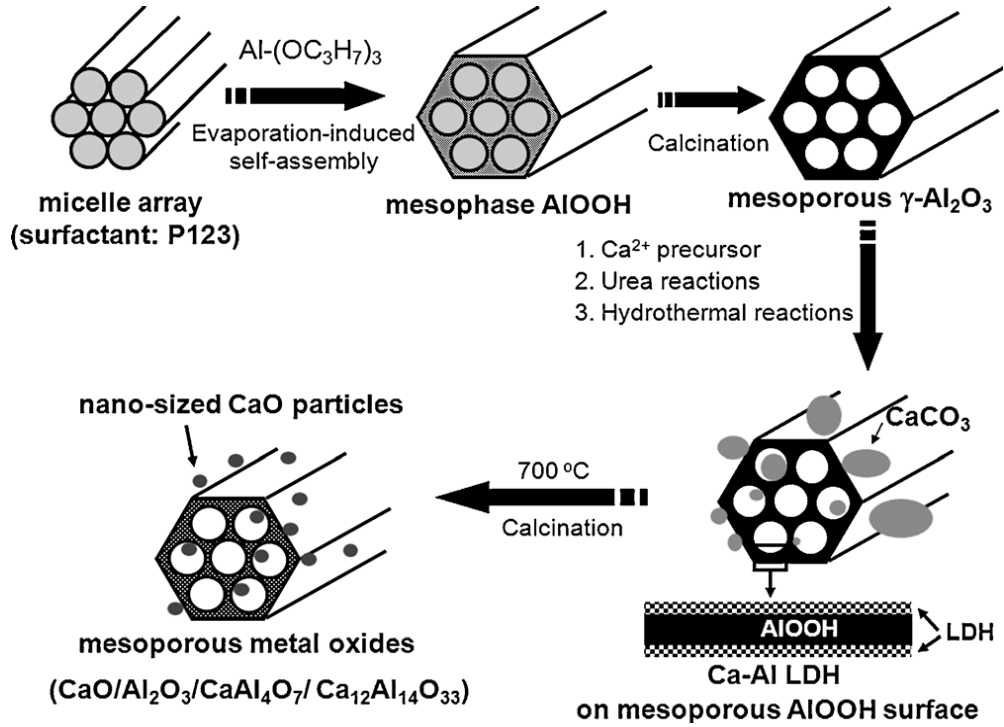
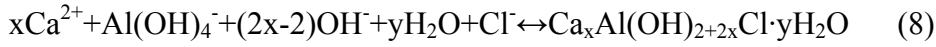
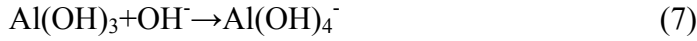


Figure 3. 5 (a) TEM image of the M-CaAl sample, the qualitative element mapping for Ca (b) and for Al (c) of the TEM image by EELS analysis, (d) the overlap image of the (b) and (c) resulting images, (e) the high resolution TEM image including its ED pattern, and (f) TEM image including nanotubes and ED pattern of the M-CaAl sample^[172].

3-3.2 Formation mechanism of mesoporous metal oxides

The formation mechanism of mesoporous metal oxide materials is illustrated in Scheme 3.1. The process for the formation of mesophase AlOOH is based on evaporation-induced self-assembly ^[161]. Organic-inorganic hybrid structures form by interfacial interaction through charge density matching between the organic surfactant P123 and inorganic aluminum isopropoxide are formed. The addition of surfactant P123 leads to the formation of micellar hexagonal arrays. At the beginning of this process, a large amount of monomers formed by hydrolysis of inorganic aluminum isopropoxide (AIP). When the concentration of the monomers in the solution reached a critical value, the monomers energetically start to interact with the surfaces of the P123 micelles, possibly through a hydrophilic group (-C-C-OH), with the copolymer associated with the Al-OH group along the hydrolyzed Al monomer (designated the AlOOH mesophase). The assembly mechanism for such an interaction could be surfactant-metal monomer complexation through electrostatic hydrogen bonding and/or van der Waals forces to direct the evolution of the assembled nanostructure ^[162-163]. When subjected to calcination at high temperature (700 °C) to remove the surfactant, the mesophase AlOOH is transformed into the crystalline γ -Al₂O₃ structure with an ordered mesostructure and high thermal stability (designated as mesoporous γ -Al₂O₃) ^[164-165]. Moreover, when mesoporous γ -Al₂O₃ and CaCl₂ are used as precursors and reacted in the presence of the urea solution, the MA-supported CaAl LDH (designated as CaAl LDH on mesoporous AlOOH surface) was formed according to Equations (1)–(8):

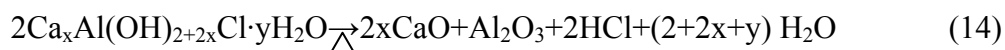
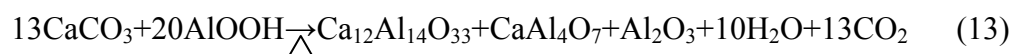
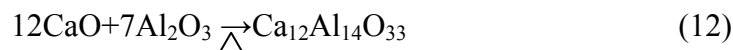
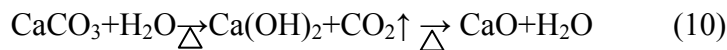
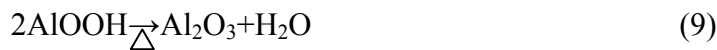




Scheme 3. 1 Illustration of the formation mechanism of ordered mesoporous metal oxide materials.

The urea solution would be thermally decomposed to form H_2CO_3 and NH_4OH at 150 °C by hydrothermal treatment, according to Equations (1) and (2). Subsequently, partial dissolution of the mesoporous $\gamma\text{-Al}_2\text{O}_3$ in the presence of the decomposed substances (OH^-) formed mesoporous AlOOH on the outer surface of mesoporous $\gamma\text{-Al}_2\text{O}_3$ following Equations (3) and (4) [166]. Under these conditions, the Ca ions should react rapidly with the decomposed matter (CO_3^{2-}) to precipitate CaCO_3 on the mesoporous AlOOH particles, according to Equations (5) and (6). Moreover, CaAl LDHs could be formed in this hydrothermal urea system, as evidenced in the XRD pattern shown in Figure 3.1(b), which is similar to a previous report on the formation of MgAl LDHs [167]. During hydrothermal

treatment, MgO and Al₂O₃ could be hydrated to form Mg(OH)₂ and Al(OH)₃, respectively, and then Mg(OH)₂ could be quickly dissociated to give Mg²⁺ and OH⁻, which were subsequently deposited on the surface of Al(OH)₃/Al₂O₃ to form a MgAl LDH material. Thus, in this system, nanosized CaAl LDH may be formed on the surface of the mesoporous AlOOH, as evidenced by LA-XRD and TEM, through combining Equations (5), (7), and (8). When the mesoporous AlOOH-supported CaAl LDH sample was calcined at 700 °C for 1 h, mesoporous metal oxides were obtained, corresponding to Equations (9)-(14). According to the literature, the phase transition of boehmite (AlOOH) into the γ-Al₂O₃ phase begins at about 400 °C following Equation (9)^[165-168]. Here, after calcination at 700 °C, CaCO₃ on the boehmite (AlOOH) surface could be decomposed into Ca(OH)₂ in the presence of H₂O and then into CaO nanoparticles, according to Equation (10). Furthermore, CaO would react with γ-Al₂O₃ at high temperature to form calcium aluminum oxides (CaAl₄O₇ or Ca₁₂Al₁₄O₃₃ or CaAlO solid solution), according to Equation (11) and (12). As a result, the CaAlO solid solution may be formed according to Equation (13).



3-3.3 CO₂ adsorptive behavior of mesoporous metal oxides

In Figure 3.6, calcined M-CaAl was used as a sorbent for CO₂ capture, for which the CO₂ sorption capacity was determined by means of TGA. To identify the sorbent performance, the sample powders were measured at 200-800 °C under pure CO₂ flow gas. Figure 3.6(a) shows the CO₂ adsorption capacity and the rate of CO₂ adsorption of the

M-CaAl sample at 600 °C for 2 h. A higher CO₂ capture capacity (ca. 40 wt.%) and rapid adsorption rate was mainly obtained in the first reaction stage. Moreover, the adsorption rate of CO₂ capture, dW/dt, is shown in the inset of Figure 3.6(a) and indicates that a maximum adsorption rate appears in the first 1-2 min when CO₂ gas is introduced. The capability of these materials to capture CO₂ strongly depends on the CaO/Ca(OH)₂ content instead of CaAlO, according to the previous literature reports^[143]. The maximum CO₂ adsorption capacity occurred at 650-700 °C, which was consistent with the results in this study. In addition, the equilibrium constants (K_a) for the reactions of Ca(OH)_{2(s)}+CO_{2(g)}→CaCO_{3(s)}+H₂O_(g) and CaO_(s)+CO_{2(g)}→CaCO_{3(s)} at 650 °C in ambient pressure were about 183.98 and 117.42, respectively. The K_a values of the reactions decreased when the temperature increased from 450 to 750 °C. This is in contrast to experimental results that show the adsorption capacity increasing with temperature. It may be assumed that the reactions were controlled by a kinetic process rather than by a thermodynamic process.

Although TGA has been widely used to study the adsorption and desorption of CO₂ sorbents, the flow of the CO₂-containing gas onto the sample bed is not well defined in TGA because of a bypass that often causes problems in kinetic studies^[169]. Herein, we present a comparative kinetic study using both TGA and a fixed-bed reactor to determine the feasibility and limitation of the two different techniques. The adsorption curves shown in Figure 3.6(c) measured by means of TGA and a fixed-bed reactor clearly indicates that adsorption takes place in two stages. The first stage is very rapid, whereas the second stage is slow. During the first stage of adsorption, reaction takes place between the active CaO of mesoporous CaAl metal oxides and CO₂, leading to the formation of surface CaCO₃. This part of the process is reaction controlled. The second stage of adsorption is rather slow and diffusion controlled; it is almost linear with time. During the slow reaction regime, the reaction rate decreased because CO₂ needed to diffuse through a CaCO₃ layer formed on the surface to reach unreacted CaO. As the sorbent surface was covered by CaCO₃, small pores

were blocked by the formation of a nonporous carbonate product layer. This layer significantly hinders the inward diffusion of CO₂ [170]. In this case, the adsorption rate in the fixed-bed reactor was similar to TGA for the same experimental conditions (see Figure 3.6 (c)). The adsorption rate in the fixed-bed reactor was about 0.5-1 min. Conversely, these results indicate that TGA can be used for kinetic studies of carbonation reactions of Ca-based sorbents. Furthermore, the CO₂ capture capacity (as carbonation efficiency) of the mesoporous materials was also strongly influenced by the carbonation temperature. Figure 3.6(b) shows that the CO₂ adsorption capacity increased with increasing temperature up to 700 °C. The maximum CO₂ adsorption capacity of the materials was about 45% at a sorption temperature of around 650 °C as obtained from the smooth curve of the CO₂ sorption capacity. The amount of maximum CO₂ adsorbed per gram of Ca was about 0.52 g of CO₂ per gram of Ca. Above that temperature (700 °C), the adsorption capacity decreased because the equilibrium reaction between $\text{CaO} + \text{CO}_2 \rightarrow \text{CaCO}_3$ occurred at 750 °C, which further evidenced a maximum adsorption of the M-CaAl at approximately 700 °C. In addition, because the calcination reaction of $\text{CaCO}_3 \rightarrow \text{CaO} + \text{CO}_2$ occurs at around 750-800 °C and is the equivalent to chemical desorption, as the temperature exceeds 750 °C, the adsorption capability decreases and ceases to adsorb CO₂ at 800 °C. On the other hand, the carbonation reaction of $\text{CaO} + \text{CO}_2 \rightarrow \text{CaCO}_3$ is chemical adsorption. At 200 °C, the temperature is too low for CO₂ adsorption.

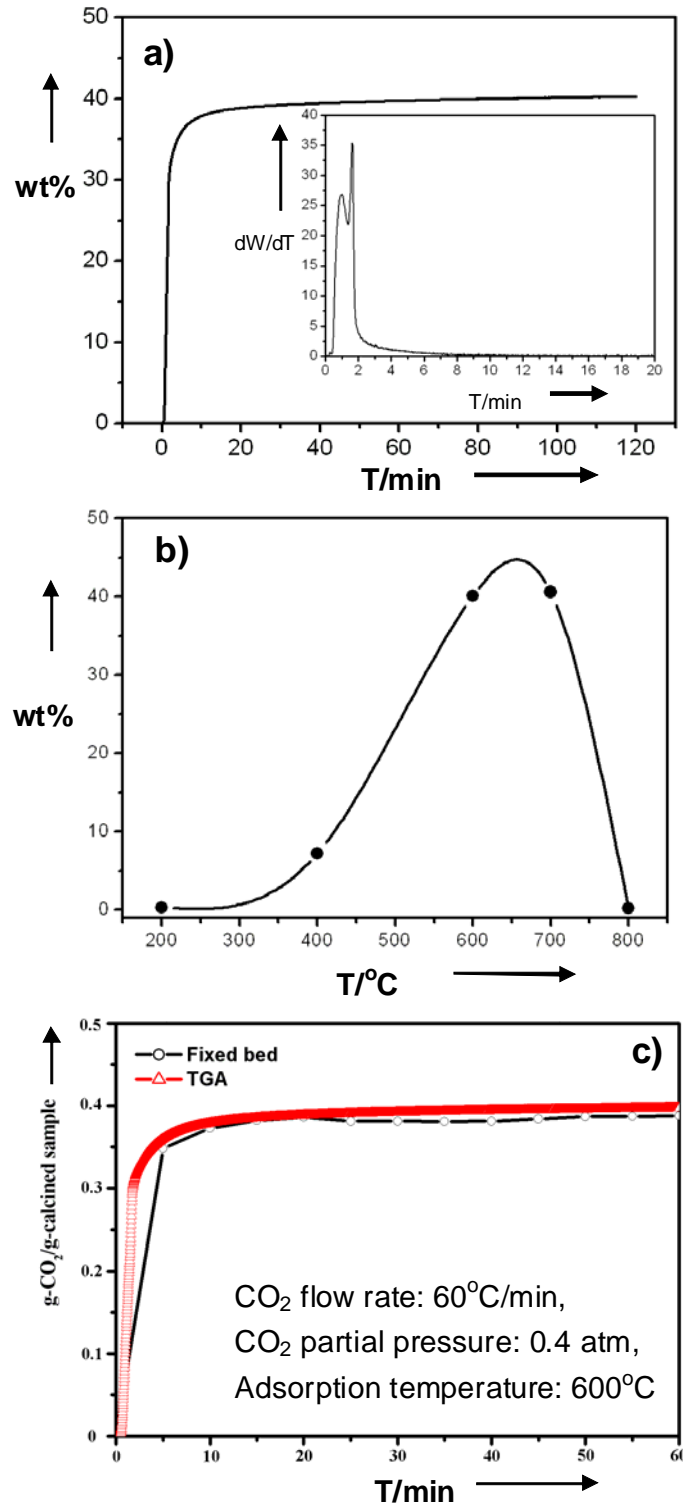


Figure 3. 6 (a) CO₂ adsorption capacity of M-CaAl sample by absorbed at 600 °C, inset includes the rate of CO₂ sorption, (b) CO₂ adsorption capacity of the sample at various temperature (200 °C, 400 °C, 600 °C, 700 °C, 800 °C), and (c) Comparison of CO₂ adsorption curve in TGA and fixed bed, where the weight (%) calculation was divided by the total weight change of the sample.

The rapid sorption and longer cycle life of the CO₂ sorbent play an important role in the industrial application of CO₂ capture. Figure 3.7(a) shows the adsorption/desorption cycle performance of CO₂ capture on M-CaAl nanoparticles at 700 °C. The CO₂ adsorption capacity showed a slight decrease from the first cycle to the 15th cycle, after which a clear decay was detected from the 15th to the 30th cycles. The irreversible adsorption of about 20% over 30 cycles is attributed to partial sorbent activity decay because of the partial sintering between CaO/CaCO₃ in the sorbents and strong chemical interactions between the sorbent and CO₂ molecules ^[171]. These results indicate that the newly synthesized mesoporous metal oxide displayed a high adsorption capacity with long-term durability. Furthermore, after being recycled 30 times, the SEM image of the mesoporous metal oxide in Figure 3.7(b) shows that partial aggregation of the mesoporous metal oxide particles may occur; the primary nanoparticles (as shown in Figure 3.3(c)) are still observed on the surface of the secondary aggregated particles, indicating that the nanostructured materials (γ -Al₂O₃, CaAl₄O₇, and Ca₁₂Al₁₄O₃₃) could provide a stable framework to inhibit the deactivation of CaO or Ca(OH)₂ and strengthen the adsorptive performance.

These results indicate that the newly-synthesized mesoporous metal oxide displayed a high adsorption capacity with long-term durability. After recycling 30 times, the SEM image of the mesoporous metal oxide in Figure 3.7(b) shows that partial aggregation of the mesoporous metal oxide particle may occur, and the primary nanoparticles (as shown in Figure 3.3(c)) were still observed on the surface of the secondary aggregated particles, indicating that the nanostructured materials (γ -Al₂O₃, CaAl₄O₇, and Ca₁₂Al₁₄O₃₃) could provide a stable framework to inhibit the deactivation of CaO or Ca(OH)₂ and strengthen the adsorptive performance.

The adsorption or desorption of CO₂ gas at 600 °C for mesoporous metal oxide could be further characterized by using FTIR spectroscopy. The FTIR spectra were recorded by using a Bomem DA8.3 spectrometer with a resolution of $\nu = 4 \text{ cm}^{-1}$ in the range of $\nu =$

4000-450 cm^{-1} , as shown in Figure 3.7(c). After CO_2 adsorption, it is evident that CaCO_3 is present in the sample. The CO_3^{2-} stretching vibration in CaCO_3 occurs at $\nu = 1430, 873,$ and 710 cm^{-1} . The weak band is characteristic of the O-H stretching vibration at $\nu = 3645 \text{ cm}^{-1}$ because there are few Ca/Al-OH bending vibrations on the surface of metal oxides. A broad band for the O-H stretching vibration at around $\nu = 3500\text{-}3300 \text{ cm}^{-1}$ is also observed as a result of adsorption of water molecules in an ambient atmosphere. Moreover, for the sample after desorption, the O-H stretching vibration bands (Ca/Al-OH) can be clearly observed at $\nu = 3650$ and 800 cm^{-1} and bands appeared at $\nu = 1420\text{-}1640$ and $880\text{-}800 \text{ cm}^{-1}$, which implies that CaCO_3 still remained at $700 \text{ }^\circ\text{C}$. According to a literature report that the CO_2 molecules were adsorbed into the active sites of the calcined metal oxide, which was prepared by using HT MgAl LDHs, different species occurred (unidentate carbonate, chelating bidentate carbonate, bridging bidentate carbonate, and bicarbonate) ^[168]. The FTIR spectroscopy results indicated that the strongest active sites correlated with unidentate-type adsorption and were chiefly responsible for the irreversibility of adsorption, which could further explain the possible adsorption mechanism.

The results reveal that mesoporous metal oxide nanoparticles can exhibit different adsorption capacities for CO_2 by controlling the mesostructured material and particle sizes (structure or phase) and be further used for CO_2 capture and hydrogen gas production by treating natural gas for applications in fuel cells, power plants, or fuel combustion in vehicles.

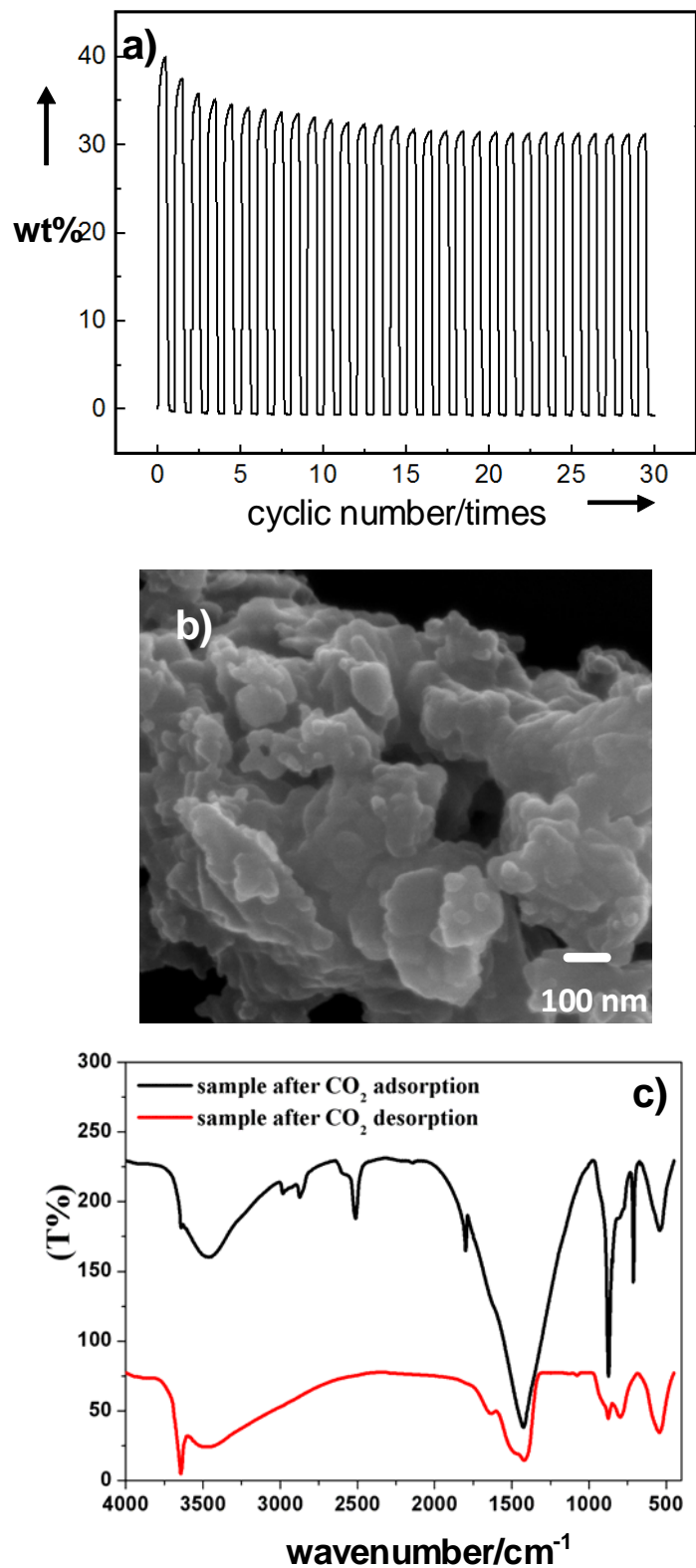
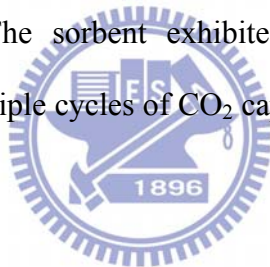


Figure 3. 7 (a) CO₂ adsorption/desorption cycles of the M-CaAl sample adsorbed at 700 °C, (b) SEM image of the M-CaAl after 30 cycles, and (c) FTIR spectra of the M-CaAl after adsorption and desorption.

3-4 Conclusion

Novel high-temperature CO₂ sorbent, mesoporous Ca-Al metal oxides, was successfully synthesized using γ -Al₂O₃ and CaCl₂ as precursors to produce mesoporous materials (γ -AlOOH with LDHs during the hydrothermal urea reaction). XRD patterns, nitrogen- adsorption isotherms, and TEM analysis confirmed that the mesoporous metal oxides had ordered mesostructured arrays with large surface areas, narrow pore size distributions, and a highly crystalline mesoporous framework. The mesoporous M-CaAls with highly dispersed CaO/Ca(OH)₂ nanoparticles inside or outside the mesoporous framework provided a high adsorption capacity and rapid adsorption ability for high-temperature CO₂ capture. The sorbent exhibited advantageous stable adsorption capacity and durability during multiple cycles of CO₂ capture at high temperature due to the mixed calcium aluminum oxides.



Chapter 4

Microwave Assisted In Situ Synthesis of Mesoporous Calcium

Aluminate Nanocomposites

4-1 Introduction

Calcium aluminates ($\text{Ca}_{12}\text{Al}_{14}\text{O}_{33}$) have long been known as a refractory mixed oxide in the steel industry and as a hydraulic material in the cement community. In recent years new applications of calcium aluminates have emerged in optical devices^[173], oxygen ionic conductors^[174], biomaterials^[175-176]. Lemonidou et al. reported that the deposition of 5 wt.% Ni on calcium aluminate (molar ratio $\text{CaO}/\text{Al}_2\text{O}_3=1/2$) proved to be more catalytic and active with lower coke deposition for the reaction of CO_2 reforming of CH_4 ^[177]. Hosono et al.^[178-179] reported that the interconnected cage-like structure of mayenite (crystal structure, see Appendix-3), a complex calcium aluminate of general formula $\text{Ca}_{12}\text{Al}_{14}\text{O}_{33}$ or $12\text{CaO}\cdot 7\text{Al}_2\text{O}_3$ or C_{12}A_7 , is an insulator with high visible transparency. Traditionally, bulk calcium aluminate cements can be obtained by fusing or sintering a mixture of CaO or CaCO_3 and alumina (Al_2O_3) at temperatures above 1400 °C but displayed very low specific surface area ($<1 \text{ m}^2/\text{g}$)^[180]. Risbud et al. reported that amorphous calcium aluminate ($\text{Ca}_{12}\text{Al}_{14}\text{O}_{33}$) powder with high surface area can be synthesized by calcining a mixed composition of both aluminum and calcium precursors (such as organic metal or metal salt) below 900 °C^[181-182]. On the other hand, crystalline calcium aluminate ($\text{Ca}_{12}\text{Al}_{14}\text{O}_{33}$) can be also obtained by evaporative decomposition of a solution made from calcium and aluminum nitrate precursors after a heat-treatment at 900 °C^[183]. Recently, Zawrah et al. further reported that the nanosized calcium aluminate with particle size of $< 50 \text{ nm}$ can be successfully synthesized by thermal decomposition treatment after 1000 °C^[184]. However, up to now, calcium aluminate nanocrystallite with mesoporous structure used as a support for catalyst and oxygen ion conductor has been little investigated.

In the recent years, microwave-enhanced chemistry has been gaining important because it can utilize the inherent properties of the liquids, solids, and their mixtures to convert microwave energy in situ into heat for promoting the reactions ^[185-186]. Hence, the microwave-assisted syntheses of mesoporous materials (such as MCM-41 and SBA-15) have attracted wide attention ^[21, 187] because it offers many advantages such as homogeneous and simultaneous heating through the reaction cell, rapid nucleation and growth, and suppression of undesired phases.

To the author's knowledge, we are the first to report the mesoporous calcium aluminate ($\text{Ca}_{12}\text{Al}_{14}\text{O}_{33}$) nanocomposites synthesized by microwave-assisted syntheses and subsequent calcination to produce a special dual-structure of polycrystalline nanorods and/or nanonetworks. Moreover, the effect of Ca/Al molar ratio on the migration of an ionic calcium species on the mesostructured surface as well as on the morphology of mesostructured $\text{Ca}_{12}\text{Al}_{14}\text{O}_{33}$ nanocomposites was also investigated. The characterization techniques including nitrogen adsorption, powder X-ray diffraction (PXRD), scanning electron microscopy (SEM) and transmission electron microscopy (TEM) with electron energy loss spectroscopy (EELS) were used to examine the crystalline structure, morphology and size of nanostructured calcium aluminates and the pore properties of these mesoporous materials before and after the microwave reaction between calcium ion and mesoporous alumina.

4-2 Experiments

4-2.1 Preparation of mesoporous calcium aluminate nanocomposites

Firstly, according to a previous study ^[153], Yuan and co-workers reported highly ordered mesoporous alumina (MA) with high thermal stability. In a typical preparation, triblock copolymer $\text{HO}(\text{CH}_2\text{CH}_2\text{O})_{20}(\text{CH}_2\text{CH}(\text{CH}_3)\text{O})_{70}(\text{CH}_2\text{CH}_2\text{O})_2\text{OH}$ (2g; Aldrich, Mn=5,800, Pluronic P123) was dissolved in absolute ethanol (20 mL; Sigma-Aldrich,

99.5%) and stirred for 4 h at room temperature. In another solution, aluminum isopropoxide (AIP, 20 mmol; Aldrich, +98 wt.%) was dissolved in nitric acid (3.2 mL; J.T Baker, 70 wt.%) and absolute ethanol (10 mL). Then, the AIP solution was slowly added to the surfactant solution, and the mixed solution was vigorously stirred for 5 h and then transferred to an oven to evaporate the solvent at 60 °C for 3 days. The resulting powder was calcined at 700 °C for 4 h with a heating rate of 5 °C min⁻¹ in an air flow and then cooled in a furnace to ambient temperature to give mesoporous Al₂O₃ (M-Al).

Secondly, the synthesized M-Al and calcium nitrate were used as the starting materials. These materials with a Ca:Al molar ratio of 1:1 or 2:1 were suspended into 100 ml of absolute alcohol solution at room temperature. Then, the solution was transferred to the TFM (tetrafluorometoxil) reactor. The reactors with the suspensions were sealed and then placed on a turntable tube for uniform heating by an equipment of microwave accelerated reaction system (model MARSTM, CEM Corporation, Matthews, NC, USA). The suspensions in the TFM vessel were heated at 80 °C for 1h in a microwave oven with 1600 W of power. The precipitation suspended in the solution was rapidly dried at 50 °C in an oven for overnight to remove the solvent. Finally, the resulting powders were calcined at 600 °C for 3h with a heating rate of 2 °C min⁻¹ in an air flow to give M-CaAl and M-2CaAl powders with Ca:Al molar ratio of 1:1 and 2:1, respectively.

4-2.2 Characterization of materials

The resulting powders were characterized by performing XRD measurements (MAC Science MXP18AHF XRD, with CuK_a radiation source, $\lambda=1.5418 \text{ \AA}$). SEM images of the sample were collected by using a JEOL-6700 field-emission electron microscope at an accelerating voltage of 15 kV. TEM micrographs and electron diffraction patterns were recorded by using a JEOL JEM-2100F electron microscope equipped with an Oxford energy-dispersive spectrometer (EDS) analysis system. Elemental Ca or Al distribution

mapping was conducted by using a TECNAI 30 electron microscope fitted with an electron energy loss spectroscopy (EELS) detector. Samples for TEM measurements were embedded in resin and ultramicrotomed into slices with thicknesses of about 50 nm. The surface area (BET) and pore size distribution were calculated using a NOVA 1000e instrument at 77 K nitrogen adsorption isotherms. All samples were degassed under vacuum at 200 °C for 2 h prior to the measurement. The samples were digested with mixed acids and their elemental compositions of Ca/Al ratio were determined by with ICP-AES on Jarrell-Ash, ICAP-9000. For the as-synthesized and calcined M-CaAl samples, they were also recorded by Fourier transform infrared spectroscopy (FTIR, Bomem DA8.3) and X-ray photoemission spectroscopy (XPS, Thermo VG Microlab 350).



4-3 Results and discussion

4-3.1 Mesoporous Al₂O₃

Figure 4.1(a) illustrates the small-angle XRD patterns of the mesoporous Al₂O₃ (M-Al), where the characteristic reflections of the p6mm hexagonal structure at $2\theta = 0.72^\circ$ (MA) are displayed and the corresponding spacing (d-spacing) is indexed with $d_{100} = 11.18^\circ$. The hexagonal unit cell parameter (a_0) of 12.9 nm (MA) was calculated from assuming a (100) reflection of the hexagonal array of pores of the mesoporous metal oxides, which is indicative of mesostructural formation. This finding also indicates that the hexagonal arrangement of the mesoporous structure was evolved upon mesoporous metal oxides synthesis. Large-angle XRD (LA-XRD) pattern of the M-Al sample is shown in Figure 4.2(a). After calcination at 700 °C, the mesoporous Al₂O₃ (M-Al) displays three broad peaks of the (311), (400), and (440) reflections, which correspond to those of crystalline γ -Al₂O₃ (JCPDS No. 29-1486), indicating a crystalline γ -Al₂O₃ framework. Figure 4.1(b) shows the high resolution image of the mesoporous Al₂O₃ exhibits the channels with 2D-hexagonal symmetry (p6mm) along [110] with an interplanar space calculated as 10.5 nm, in good

agreement with that determined by SA-XRD (11.47 nm). Nitrogen adsorption isotherms and the corresponding pore size distribution of the mesoporous Al₂O₃ (M-Al) are shown in Figures 4.1(c) and 4.1(d). The isotherms can be classified as type IV, indicating typical mesoporous metal oxides^[155]. The hysteresis loop of mesoporous Al₂O₃ (MA) displays type H1 characteristics, and the steepness of the capillary condensation step indicates the uniformity of the mesopores. Some typical textural parameter of the M-Al sample, respectively, were Brunauer-Emmett-Teller (BET) surface areas of 202 m² g⁻¹; pore volumes of 0.47 cm³ g⁻¹; and pore size distributions of 5.8 nm. The high surface area and large pore volume maybe enhance the potential applications of these mesoporous metal oxide materials in the nanostructural fabrication.

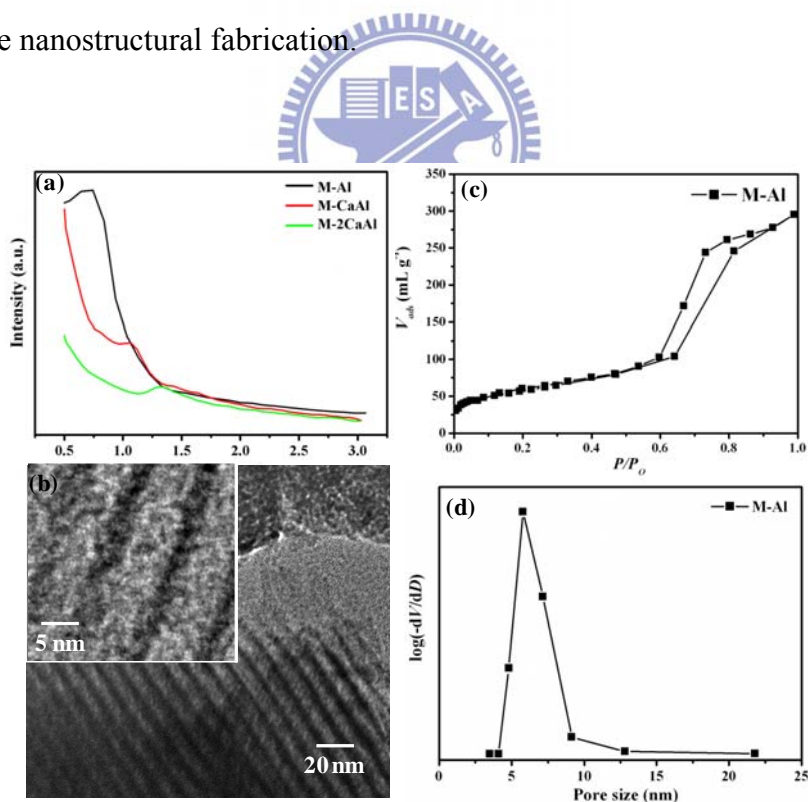


Figure 4. 1 (a) small-angle XRD patterns of calcined mesoporous materials; (b) TEM images including the high resolution TEM image, (c) N₂ adsorption isotherm and (d) pore size distribution of calcined mesoporous Al₂O₃ (M-Al)^[197].

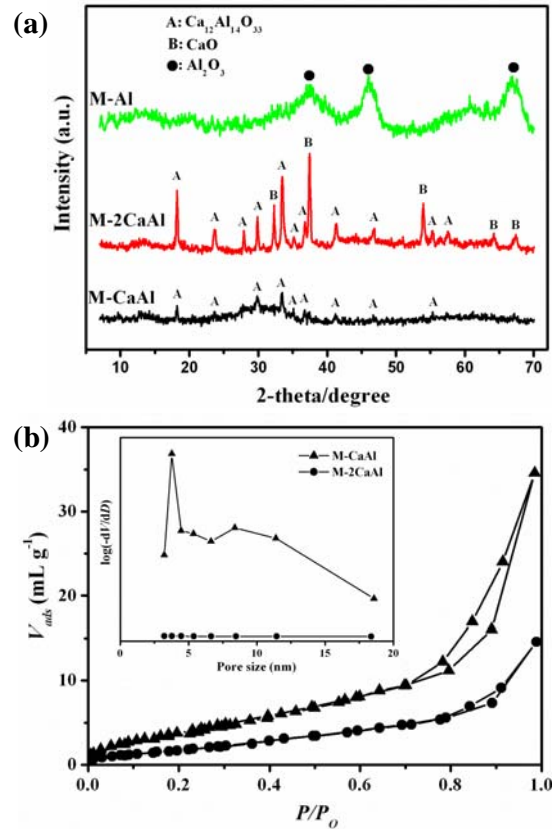


Figure 4. 2 (a) Large-angle XRD patterns^[197] and N_2 adsorption isotherms including pore size distribution of calcined mesoporous materials.

4-3.2 Mesoporous calcium aluminate nanocomposites

Mesoporous calcium aluminate nanocomposites with different molar ratios of M-CaAl and M-2CaAl were synthesized by reacting the mesoporous Al_2O_3 with a controllable concentration of calcium under the microwave-assisted hydrothermal process where the actual Ca/Al molar ratio of 0.96 (M-CaAl) and 1.94 (M-2CaAl) was measured by ICP-AES. The small- and large-angle XRD patterns of the calcined mesoporous nanocomposites (M-CaAl and M-2CaAl) are shown in Figure 4.1(a) and Figure 4.2(a), respectively. The small-angle XRD characterization of the M-CaAl and M-2CaAl samples displayed single broad diffraction peak at $2\theta = 1.06^\circ$ and $2\theta = 1.33^\circ$, respectively. The pore size decreases with increasing molar ratio of Ca/Al, demonstrated by the d-spacing reducing from 8 nm to 6.7 nm. However, the low intensity and broadened diffraction peak in the small-angle region

indicate the wormhole framework. This reveals that the Ca loading leads to the amorphous structure. Besides, the existence of small-angle diffraction peak also indicates the retained mesostructure throughout the calcination process ^[188]. This finding also demonstrates that the hexagonal arrangement of the mesoporous structure was evolved upon the synthesis of the mesoporous calcium aluminates. Additionally, the large-angle XRD patterns of the M-CaAl (Ca/Al=1:1) and M-2CaAl (Ca/Al=2:1) sample calcined at 600 °C were characterized and the main diffraction peaks correspond to crystalline structures of Ca₁₂Al₁₄O₃₃ (JCPDS No. 70-2144) and CaO (JCPDS No. 04-0777), marked as A and B, respectively. Moreover, these obvious diffraction peaks of the M-CaAl sample exhibited a pure crystalline Ca₁₂Al₁₄O₃₃ compound and the broad peaks maybe also indicate the formation of nano-sized grain in this compound. According to the previous reported literature, the Ca₁₂Al₁₄O₃₃ crystalline phase usually formed above 800 °C ^[189-190]. However, in our studies, this phase appeared obviously after calcinations at 600 °C. This may be attributed to the microwave heating, which can directly interact with the dipole of molecules, rendering accelerated uniform reactions. During the microwave heating, the kinetic energies adsorbed by those molecules in the solution become higher and thus make Ca ions in this reaction evenly distributed through the porous structure and induce a stronger affinity of the Ca ions to the high surface-area and active mesoporous Al₂O₃ matrix ^[191]; thus the reactions between Ca and Al species could occur at lower temperature to produce the crystalline Ca₁₂Al₁₄O₃₃ phases. In addition, for the M-2CaAl sample, the XRD patterns in Figure 4.2(a) indicate both phase formation of CaO and Ca₁₂Al₁₄O₃₃ compounds. It is implied that the extra un-reacted Ca species could be transferred to form calcium oxide after calcination at high temperature. Moreover, in Figure 4.2(b), the mesoporous calcium aluminate nanocomposites showed a hysteresis loop of type H2, which is typical for wormhole-like mesostructures and hierarchical scaffold-like mesoporous structures ^[156-157]. Some typical textural parameters of the M-CaAl and M-2CaAl samples were measured by

Brunauer-Emmett-Teller (BET) to display surface areas of $51 \text{ m}^2 \text{ g}^{-1}$ and $16 \text{ m}^2 \text{ g}^{-1}$, pore volumes of $0.09 \text{ cm}^3 \text{ g}^{-1}$ and $0.04 \text{ cm}^3 \text{ g}^{-1}$ and average pore size distributions of 11.8 nm and 3.9 nm, respectively. This indicates that more Ca loading would cause the formation of excessive CaO particles and the partial blocking of the mesopore system to produce smaller BET surface area and pore volume for M-2CaAl sample. In contrast, for Ca-less sample (M-CaAl), Ca ions could be uniformly distributed in the mesoporous Al_2O_3 matrix to produce smaller $\text{Ca}_{12}\text{Al}_{14}\text{O}_{33}$ nanorods and larger BET surface area and pore volume after calcining the M-CaAl nanocomposites at 600°C .

The SEM images of calcined mesoporous calcium aluminate nanocomposites were displayed in Figure 4.3. For the M-CaAl sample (Ca/Al=1:1), Figure 4.3(a) and (b) show that the nano-rods with 200-400 nm of length and 50 nm-120 nm of width were highly dispersed on the surface of mesostructured matrix and found that the $\text{Ca}_{12}\text{Al}_{14}\text{O}_{33}$ nanorods seems to either directly nucleate and grow from the surface or initiate from the interior mesostructure. The energy-dispersive spectral analysis (EDS) in Figure 4.3(c), also showed that no other impure elements, except Ca, Al and O elements, are detected, and the Ca/Al molar ratio of the mesoporous nanocomposites was estimated to be ca. 0.833 from the quantitative EDS analyses; it is close to the theoretical value of $\text{Ca}_{12}\text{Al}_{14}\text{O}_{33}$ (Ca/Al molar ratio = 0.857), possibly indicating the mesoporous nanocomposites is characteristic of a highly chemically pure $\text{Ca}_{12}\text{Al}_{14}\text{O}_{33}$ phase. It is guessed that the $\text{Ca}_{12}\text{Al}_{14}\text{O}_{33}$ nanorod-like crystallites on the mesoporous Ca-containing Al_2O_3 matrix were in-situ formed from the calcinations and interaction of the Ca species and Al_2O_3 matrix hybrid precursor prepared by microwave accelerated reaction. Moreover, Figure 4.3(a) also appeared a small portion of particles (with 0.5-1.5 μm in size) on the surface of mesoporous Ca-containing Al_2O_3 matrix, and it is possible that the rare unreactive calcium species on the Al_2O_3 matrix was calcined to form the calcium oxides. In contrast, the M-2CaAl sample (Ca/Al=2:1) showed in Figure 4.3(d) displays a rougher surface morphology and no uniform nanorods can be

detected, suggesting that the superabundant Ca species was possibly transferred into the aggregation of CaO particles on the mesoporous $C_{12}Al_{14}O_{33}$ matrix, as corresponding to large-angle XRD results (as shown in Figure 4.2(a)). Generally, the pure $Ca_{12}Al_{14}O_{33}$ crystallites was formed at high temperature (up to 800 °C) by following the reaction of $12CaO + 7Al_2O_3 \rightarrow Ca_{12}Al_{14}O_{33}$ with the Ca/Al molar ratio = 0.857; however, as the excessive Ca was added such as this sample (M-2CaAl, Ca/Al = 2), large CaO particles may be easily formed on the mesostructural Al_2O_3 matrix after calcinations, as clearly evidenced by the XRD with the sharp diffraction peaks of CaO crystal phase.

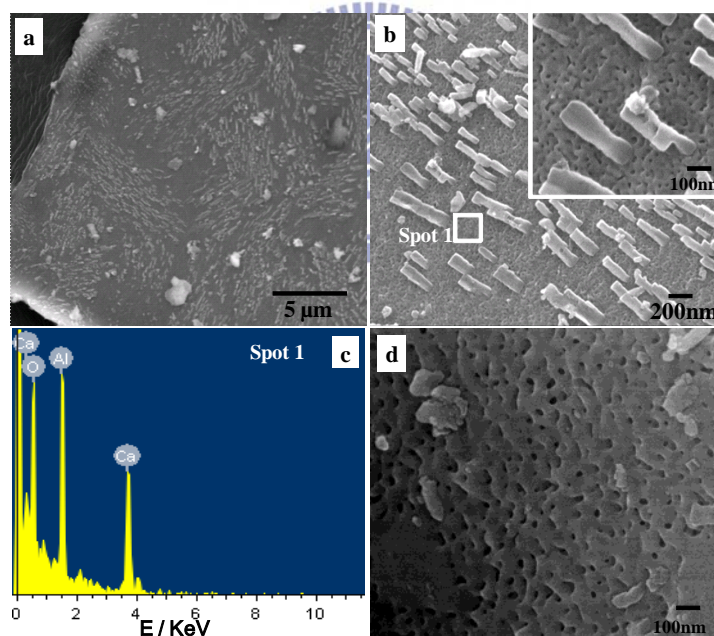


Figure 4. 3 SEM images of calcined samples (M-CaAl sample (a) and (b) including EDS (c) for Spot 1) and (M-2CaAl sample (d))^[197].

The TEM images of the calcined calcium aluminate nanocomposites (M-CaAl and M-2CaAl samples) are shown in Figure 4.4 and 4.5. For M-CaAl sample, the nanorods with diameter of 50-120 nm and length of 200-400 nm were distributed on the surface of mesoporous Ca-containing Al_2O_3 matrix, as shown in Figure 4.4(a). On the other hand, part of nanorods was observed to grow outward from the pore structure inside mesochannel for

the magnified TEM image in Figure 4.4(b) where the pore size distribution of mesostructured matrix was ca. 10-50 nm. It is suggested that when the Ca species were loaded into the ordered mesoporous Al_2O_3 under microwave assisted synthesis, a reaction between the order mesoporous Al_2O_3 frameworks with Ca ions could occur to initiate an intermediate compound which was then transformed into the mesoporous calcium aluminates with $\text{Ca}_{12}\text{Al}_{14}\text{O}_{33}$ nanorods during the subsequent calcinations. During the synthesis process, it would cause the ordered mesoporous frameworks to be consumed to form the larger mesopores. The high resolution TEM (HRTEM) and FT (fourier transform) diagram in Figure 4.4(d) reveal the $\text{Ca}_{12}\text{Al}_{14}\text{O}_{33}$ nanorods seem to be poor-crystalline structure where the diffraction rings correspond to the XRD peaks of the (211), (310), (321), and (420) reflections.

When the Ca/Al molar ratio was increased up to 2, the TEM image of the M-2CaAl sample in Figure 4.4(c) found that no nanorods can be disclosed on the mesoporous frameworks and the pore size distribution become non-uniformly with large nanopore size greater than 50 nm). Furthermore, most of the pores seem to be covered by the excessive and large-scale CaO on the surface of the larger nanoporous $\text{Ca}_{12}\text{Al}_{14}\text{O}_{33}$ matrix to limit the growth of nanorods under calcinations at high temperature. Furthermore, TEM image, EELS mapping, and FT (fourier transform) diagram were used to characterize the crystalline structure and element distribution of the calcined mesoporous calcium aluminate nanocomposites (M-CaAl) in Figure 4.5. The M-CaAl sample shows a mesoporous structure with the nanorods to form the nanocomposites in Figure 4.5(a). In addition, two images of the EELS mapping for Ca and Al were shown in Figure 4.5(b) and 4.5(c), respectively. Figure 4(d) is overlapped the image of Figure 4.5(b) and 4.5 (c), which can be clearly observed and divided two parts: (1) the Ca or Al atoms may be homogeneously dispersed in the mesoporous structure with element compositions of Ca-containing Al_2O_3 frameworks; (2) the heterogeneous and aggregative Ca atoms are observed for $\text{Ca}_{12}\text{Al}_{14}\text{O}_{33}$

nanorods that grow either from the inside mesostructural channel or outside mesostructural surface. Hence, the $\text{Ca}_{12}\text{Al}_{14}\text{O}_{33}$ nanorods could be formed by starting a nucleation process between calcium species and mesoporous Al_2O_3 , and subsequently growth in the later annealing process.

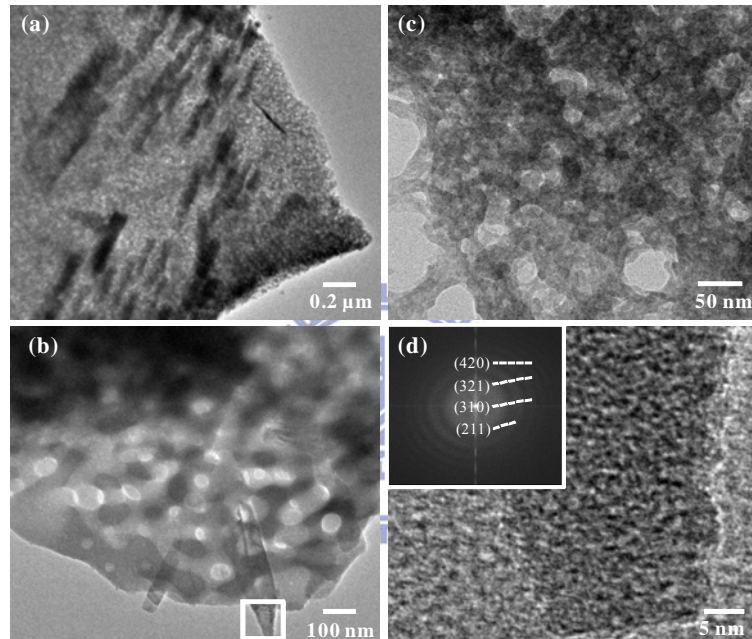


Figure 4. 4 TEM images of calcined mesoporous materials (M-CaAl sample (a), (b)) and (M-2CaAl sample (c)); (d) showing the high resolution TEM image and FT pattern of the cubic area in the image (b)^[197].

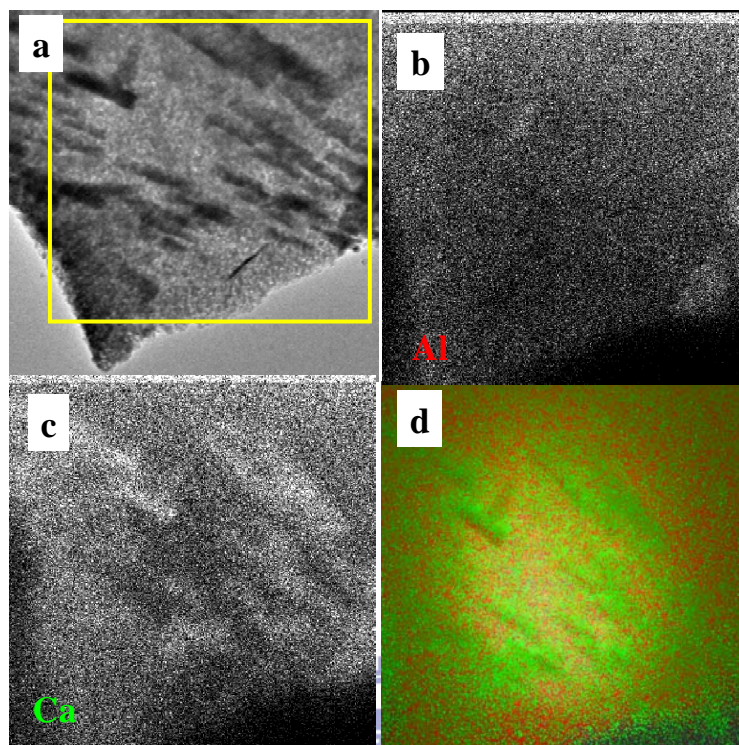


Figure 4. 5 TEM image of the M-CaAl sample, the qualitative element mapping for Al (b) and for Ca (c) of the TEM image by EELS analysis, (d) the overlap image of the (b) and (c) resulting images. (Note: green dot indicating Ca; red dot indicating Al)^[197].

The Al 2s core level of the as-synthesized sample (after microwave hydrothermal treatment) or calcined sample (M-CaAl) as well as the valence band was further analyzed using an XPS measurement. The XPS spectra in Figure 4.6(a) indicate the microwave-heating sample mainly displays the Al 2s of the hydrated-alumina (Al-OH and Al-OOH) at ~ 116 eV of binding energy. In contrast, the calcined sample (M-CaAl) exhibited the Al 2s of sharp peak at ~ 123 eV of binding energy, indicating the formation of calcium-aluminum oxides after calcination at high temperature. Further, the FTIR spectra of as-synthesized sample or calcined sample (M-CaAl) in Figure 4.6(b) evidenced the difference between microwave-assisted and calcination treatment. For the microwave treatment, the pair of bands at 953 cm^{-1} and 1020 cm^{-1} could be associated with the characteristic vibrations of the Al-OH bonding. The O-H stretching vibration bands (Ca/Al-OH) can be clearly observed at 3650 cm^{-1} and 835 cm^{-1} . The broad peak at 625 cm^{-1} and 2100 cm^{-1} can be stretching and

bending modes of AlO-(OH) ^[192]. The wide absorption band at the region 3200-3600 cm⁻¹ and the intensive bands at 1380 cm⁻¹ and 1640 cm⁻¹ are due to the vibration of H₂O molecules which took part in hydrogen bonding with Al₂O₃ surface ^[193]. It is implied that there is a hydrated formation of Ca-Al₂O₃ when mesoporous Al₂O₃ mixed with calcium species after microwave hydrothermal treatment. Additionally, according to the previous report ^[194], FTIR spectra of inorganic aluminates varied depending on aluminum coordination number, the state of coordination group (“isolated” or “condensed”) and the vibrational coupling between neighboring groups. The above mention led to a conclusion that the characteristic absorption regions of Al-O stretching vibrations are 650-800 cm⁻¹ for “isolated” and 700-900 cm⁻¹ for “condensed” AlO₄ tetrahedra, while 400-530 cm⁻¹ and 500-680 cm⁻¹ regions for “isolated” and “condensed” AlO₆ octahedra. In FTIR spectrum, the Al-O stretching vibrations for tetrahedral coordination AlO₄ are observed in the 750-850 cm⁻¹ spectral region. At the same time, for the octahedral coordination AlO₆, they were observed at 500-750 cm⁻¹. FTIR spectra in the OH-stretching region display a sharp and broader bond at 3650 cm⁻¹ (Ca-OH and Al-OH bond) and at 3450 cm⁻¹ (H₂O bond), respectively. The FTIR analysis for calcined sample (M-CaAl) is much consistent with the XRD results.

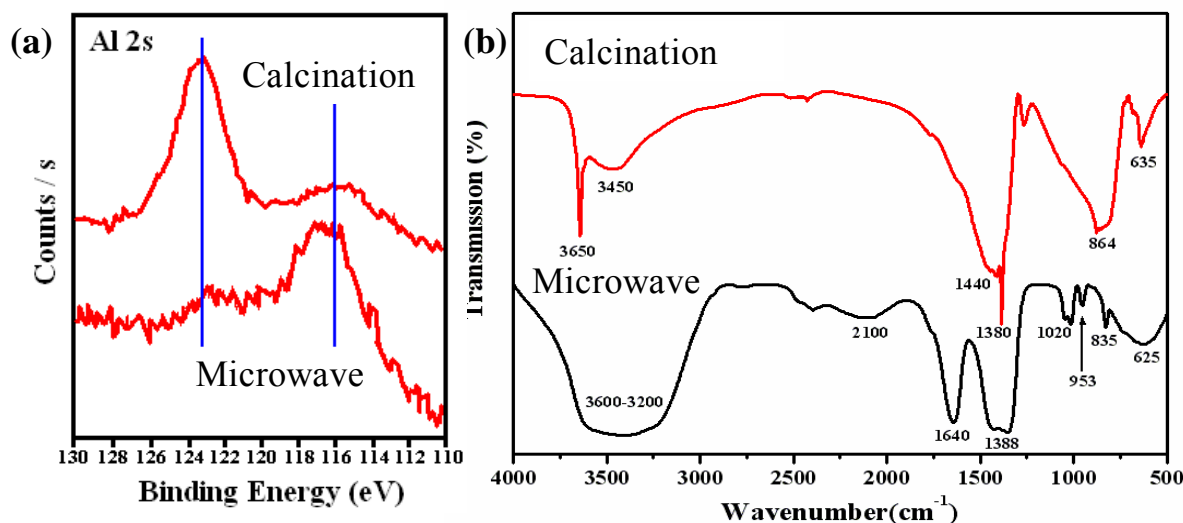


Figure 4. 6 (a) X-ray Photoelectron and (b) FTIR Spectroscopy of the M-CaAl sample prepared by microwave hydrothermal treatment for 1h and calcined at 600 °C .

4-3.3 Formation mechanism of mesoporous calcium aluminate nanocomposites

Figure 4.7(a) shows the PXRD patterns of these calcined samples (Ca/Al molar ratio=1) prepared by microwave assisted process with different hydrothermal time from 15min to 2h. Firstly, sample 15min and 30min samples, in, no diffraction peaks were detected in PXRD patterns, indicating that these samples may exist with poor-crystalline or amorphous Ca-Al-O solid solution. As increasing the microwave hydrothermal time, for 1h and 2h samples, these diffraction peaks can be clearly indexed as crystalline CaO and $\text{Ca}_{12}\text{Al}_{14}\text{O}_{33}$ phase. The SEM image for 1 h-microwave calcined sample was shown in Figure 4.3(b) which evidenced the $\text{Ca}_{12}\text{Al}_{14}\text{O}_{33}$ nanorods grown on the mesoporous surface. Increasing microwave hydrothermal time to 2 h, more nanorods and less nanotubes were found to be dispersed on the mesoporous Ca-containing Al_2O_3 matrix in presence at the same time as shown in Figure 4.7(b) and 4.7(c) observed that there are aggregative and large CaO particles were also observed in the sample. It can be inferred that longer microwave heating time may decrease the attractive force between Ca^{2+} and Al-OH, part of calcium ions remaining outside the surface of mesoporus Al_2O_3 , and rapidly migrated and aggregated to

form the larger CaO particle during subsequent calcination, as corresponding to the PXRD results of Figure 4.7(a). On the other hand, if a longer time such as more than 3 h was applied to the microwave-assisted reaction, it was found that more crystalline $\text{Ca}_{12}\text{Al}_{14}\text{O}_{33}$ nanotubes (or disappear) may be formed, indicating the growth of the crystalline $\text{Ca}_{12}\text{Al}_{14}\text{O}_{33}$ nanorods or nanotubes varies with microwave reaction parameter such as hydrothermal time.

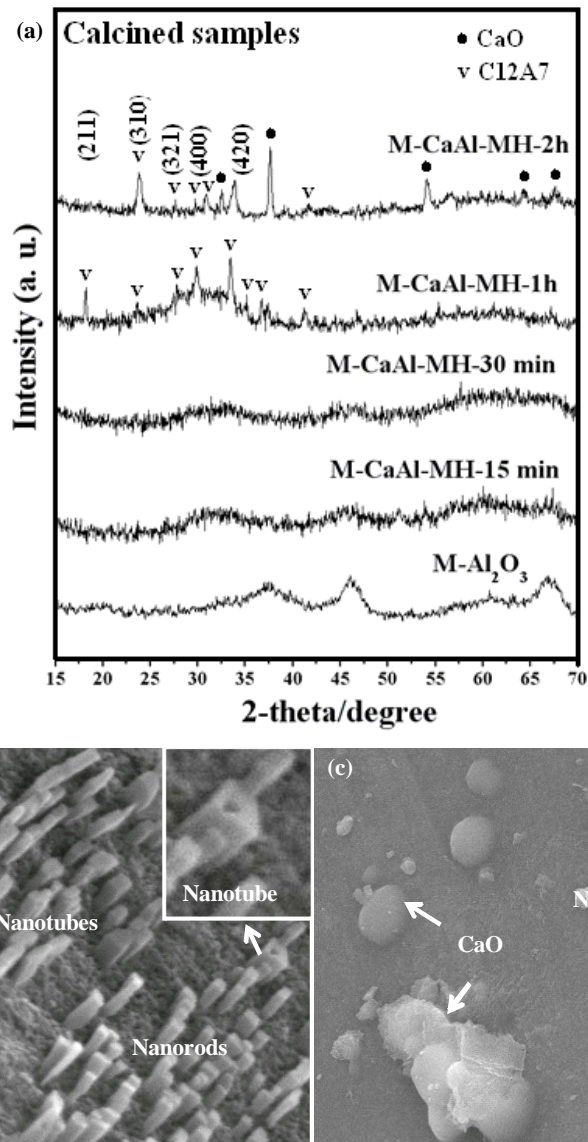
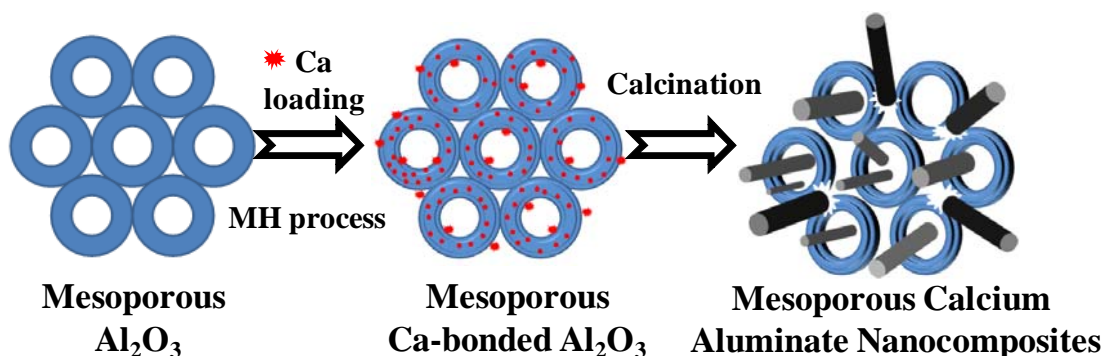


Figure 4. 7 (a) Large-angle XRD patterns of calcined samples (M-CaAl) with different reactive time at 80 °C during microwave hydrothermal (MH) reaction and then calcined at 600 °C.; (b) and (c) SEM images of calcined samples (M-CaAl-MH-2h) with analyzing in two different areas.

Scheme 4.1 illustrates the formation mechanism of mesoporous calcium aluminate nanocomposites. The process for the formation of mesoporous Al_2O_3 is based on a so-called “evaporation induced self-assembly (EISA)” [161, 196]. When subjected to calcination at high temperature (700 °C) to remove the surfactant, polycrystalline $\gamma\text{-Al}_2\text{O}_3$ structure was formed with an ordered mesostructure and high thermal stability (designated as mesoporous Al_2O_3), as corresponding to the PXRD in Figure 4.2(a). As the mesoporous $\gamma\text{-Al}_2\text{O}_3$ was used as a support to react with calcium ion in alcohol solution during microwave hydrothermal reaction, the formation pathway of the $\text{Ca}_{12}\text{Al}_{14}\text{O}_{33}$ nanorods may be involved with the Al_2O_3 hydration and a nucleation process between Ca species and Al_2O_3 according to the results of PXRD, SEM, XPS and FTIR. In the solution, the mesoporous Al_2O_3 crystallite may be hydrated to form amorphous mesoporous hydrated- Al_2O_3 which possessed high-concentrated oxy-hydroxide and hydroxide groups (such as AlO-OH and AlOH) on the Al_2O_3 surface. During the microwave synthesis, the diffusion of Ca ions and molecules was attracted and promoted toward the hydrated- Al_2O_3 matrix to deposit inside or outside the surface of mesoporous hydrated- Al_2O_3 surface, leading to the pre-crystal formation (such as AlO-Ca-OH or CaAlO(OH)_x ; designated as mesoporous Ca-bonded Al_2O_3). Next, the solid-state reaction (calcinations) could promote the phase transformation of the mesoporous calcium aluminate nanocomposites where are two kind of calcium aluminates (amorphous Ca-containing Al_2O_3 or crystalline $\text{Ca}_{12}\text{Al}_{14}\text{O}_{33}$ nanorods) could be formed depending on Ca ion content. The Ca-rich pre-crystal complexes inside the mesochannel pore or outside the surface of Al_2O_3 mesochannel can react with more Al_2O_3 nano-frameworks to grow pure $\text{Ca}_{12}\text{Al}_{14}\text{O}_{33}$ nanorods after calcinations at high temperature. In contrast, the Ca-less deposited on the Al_2O_3 surface may be doped into the Al_2O_3 frameworks to form amorphous Ca-O-Al solid solution. In summary, hydrothermal time and element composition (Ca/Al) play important roles in preparing the mesoporous calcium aluminate nanocomposites via microwave hydrothermal process.



Scheme 4. 1 The formation mechanism of mesoporous calcium aluminate nanocomposites.

4-4 Conclusion

Novel mesoporous calcium aluminate ($\text{Ca}_{12}\text{Al}_{14}\text{O}_{33}$) nanocomposites with nano-scale rods and mesoporous frameworks have been successfully synthesized by using the microwave-hydrothermal process and calcination below 600 °C. The mesoporous calcium aluminate nanocomposites possessed a specific surface area of $\sim 51\text{m}^2\text{g}^{-1}$ and a broad pore size distribution with 4-12 nm. The results of SEM, TEM and PXRD showed that highly dispersed $\text{Ca}_{12}\text{Al}_{14}\text{O}_{33}$ nanorods on the mesoporous frameworks were obtained by controlling the Ca/Al molar ratio of 1:1 where the polycrystalline-like $\text{Ca}_{12}\text{Al}_{14}\text{O}_{33}$ nanorods were grown in/on the one-dimensional mesochannels. The formation mechanism of the mesoporous calcium aluminate nanocomposites could be possibly proposed as the results of XRD, TEM/EELS, FTIR, and XPS analyses.

Chapter 5

Synthesis and Characterization of Mesoporous Gd₂O₃ Nanotube and Its Use as a Drug-Carrying Vehicle

5-1 Introduction

Nanocapsules have been proposed as a drug carrier that may be used to realize the “magic bullet” concept proposed by Couvreur et al. ^[198], which refers to a drug carrier capable of targeting a particular site and releasing its contents when desired. Nanocapsules offer advantages by enabling the drug to be encapsulated in a protective environment. Nanotubes have been suggested as a promising alternative, offering advantages such as distinct inner and outer surfaces which are readily accessible by removal of the end caps, and an increased volume ^[199] providing a higher payload capacity. However, when the drug is simply filled into a porous network of tubes, a major problem is the uncontrolled release of drugs or therapeutics. Therefore, manipulation of a controlled release kinetic is a key objective of many novel drug delivery approaches ^[200]. By combining the attractive tubular structure of silica nanotubes with magnetic properties of iron oxide, magnetic nanotubes have recently been developed (that is, silica–iron oxide composite nanotubes) ^[201] as platforms for image-guided targeted drug delivery. In addition, drug release from the magnetic core/shell nanocarriers that comprise magnetic nanoparticulate “cores” with an organic or inorganic “shell” can be easily triggered by an external magnet, which has been known as the “magneticmotor” for site-specific drug delivery applications ^[202]. In our laboratory, we have reported a novel core/shell nanocarrier with a drug-containing silica core surrounded by a single-crystalline iron oxide shell ^[203]. The magnetic nanoshell displays an ultrafast response and sensitivity upon exposure to a high-frequency magnetic field (HFMF), in which the highly magnetic-sensitive property of the nanometer-scale shell allows a controlled burst release of drug in a quantitative manner. The template synthesis is

a general approach for preparing nanomaterials that involves chemical synthesis or electrochemical deposition of the desired materials within the pores of a nanoporous membrane or other solid surface. By using hard templates, with a well-confined void, through a reciprocal casting technology, the resulting entities, after removal of the hard templates, forming channels, pores, or connected hollow space, have been extensively reported ^[204]. However, such a hard templating method involves multi-stage processes and sometimes leads to the loss of pore structure during the removal of hard templates ^[205]. Recently, block copolymers have been increasingly used to organize mesostructured composite solids, because the architectures of the amphiphilic block copolymers can be rationally adjusted to control the interactions between the inorganic and organic species. Selfassembly of block copolymers ^[206], surfactants ^[207], colloidal suspensions ^[208] and proteins ^[209] as soft templates provide a versatile approach to the creation of nanostructures with potential applications in biomaterials and nanotechnology. Long-chain or block polymers have been reported as an M41S family of mesoporous silica and SBA-15 mesoporous silica, where a hexagonally ordered mesoporous structure was observed ^[210]. However, to the best of our knowledge, there has been little reported study on the formation of oxide nanotube by soft-templating.

In this study, we prepared a tubular nanostructure constructed with Gd_2O_3 high-crystalline nanoparticles via a soft-templating method by amphiphilic block copolymer as a structure-directing agent and gadolinium isopropoxide as an inorganic precursor in non-aqueous solution. The gadolinium isopropoxide was frequently used as Gd alkoxide in the conventional sol-gel process to synthesize Gd_2O_3 thin film or powder because the transition from a solution into a solid involved the condensation and hydrolysis of alkoxide ^[211]. However, trials have not yet been made for Gd_2O_3 nanotube with high crystallinity by combining both softtemplating and sol-gel processes. The resulting mesoporous Gd_2O_3 was then characterized using powder X-ray diffraction (PXRD), and transmission electron

microscopy (TEM) with electron diffraction (ED) pattern was used to examine the nanostructural properties of Gd₂O₃ nanotube. Nitrogen sorption was used to obtain the pore size distribution of the Gd₂O₃ nanotube. For magnetic materials such as Gd₂O₃ or Fe₃O₄ nanoparticles, intensive interest has mainly focused on magnetic resonance imaging (MRI) or drug storage for subsequent delivery applications ^[212-213]. Here, the Gd₂O₃ nanotube was employed as a drug carrier and demonstrated a controlled release pattern of a model drug via stimulus with an external magnetic field.

5-2 Experiments

5-2.1 Synthesis of Gd₂O₃ nanotube

Mesoporous gadolinium oxide was synthesized using a surfactant solution of 0.183 g of block copolymer HO(CH₂CH₂O)₂₀(CH₂CH(CH₃)O)₇₀(CH₂CH₂O)₂₀H (Aldrich, Mn ~5800, Pluronic P123) dissolved in 5 ml isopropanol (Sigma-Aldrich, 99.9%, IPA) and stirred at 40 °C for 2 h. The pH value of the solution was adjusted to pH = 1.0 by adding HCl solution (Merk, 30%) followed by agitating at 40 °C for 24 h; the solution was then cooled down to room temperature (RT). Additionally, the Gd precursor solution composed of 0.42 g gadolinium isopropoxide (Stream, 99.9%, Gd(OC₃H₇)₃), 6 ml of toluene, 4 ml of IPA and 0.38 g of acetyl acetone (Fluka, 99.6%, CH₃COCH₂COCH₃, AcAc) was slowly dropped into the surfactant solution at RT under stirring to give a mixed solution. The mixed solution was stirred at 80 °C for 24 h in a PP bottle and then was cooled down to room temperature. The precipitate was filtered, washed with ethanol, dried at 40 °C for 24 h, and then calcined at 580 °C with a heating rate of 1 °C min⁻¹ for 6 h in air, then furnace-cooled to ambient temperature.

5-2.2 Characterization

The resulting powders were characterized using powder X-ray diffraction measurements (MAC Science MXP18AHF XRD, with Cu K α radiation source, $\lambda = 1.5418$ Å). TEM micrographs and electron diffraction patterns were recorded by a JEOL JEM-2100F electron microscope equipped with an Oxford energy-dispersive spectrometer (EDS) analysis system. Samples for TEM measurements were embedded in resin and ultramicrotomed into slices with thickness of ~50 nm. Nitrogen sorption measurements at 77 K were carried out a Micromeritics ASAP 2010 system. The pore diameters of samples were determined by the BJH (Barrett-Joyner-Halenda) method on the basis of desorption branches of nitrogen isotherms. Attenuated total reflectance Fourier transform infrared spectroscopy (ATR-FTIR) spectra were recorded on a spectrometer (Bomem DA8.3, Canada) with a KBr plate. The FTIR spectra were taken with a resolution of 2 cm $^{-1}$ in the range of 4000-400 cm $^{-1}$. The Gd $_2$ O $_3$ nanotubes were magnetized (M-H loops) at 300 K with applied fields of up to 10 kOe using a Quantum Design MPMS-7 SQUID magnetometer.

5-2.3 Loading of drug ibuprofen (IBU)

The loading of the drug IBU (Aldrich) inside the Gd $_2$ O $_3$ nanotube was carried out as follows: 0.02g of the samples was added to 10 ml of ibuprofen hexane solution (1 mg ml $^{-1}$) and soaked with stirring at 45 °C for 48 h until the concentration of the solution became steady; this was conducted by monitoring the ibuprofen concentration using a Lambda 20 UV-Vis spectrometer at a wavelength of 272 nm. The mixture was then cooled quickly to ambient temperature. Finally, the precipitate was filtered, washed quickly and thoroughly with hexane, and dried under vacuum at 40 °C. The amount of drug encapsulated in the Gd $_2$ O $_3$ nanotube was then calculated by the total amount of IBU, subtracting the residual IBU in the supernatant. The encapsulation efficiency (EE) of IBU was obtained as follows:

$$EE\% = (A - B)/A \times 100$$

where A is the total amount of the IBU and B is the amount of IBU remaining in the supernatant.

5-2.4 Drug-release behavior under high-frequency magnetic field (HFMF)

The high-frequency magnetic field (HFMF) of 50-100 kHz was applied to the Gd₂O₃ nanotube to investigate the drug-release behavior. The strength of the magnetic field depended on the coils, the frequency was 50 kHz, and the strength of the magnetic field (H) was kept at 2.5 kA m⁻¹ [214]. The temperature of the HFMF generator was controlled by cycling cooling water at 25 °C. The drug release behavior from the Gd₂O₃ nanotube was measured in 10 ml phosphate buffered saline per sponge cube (pH 7.4). The released ibuprofen concentration was monitored by a Lambda 20 UV-Vis spectrometer at a wavelength of 272 nm.



5-2.5 Cell culture test

Cytotoxicity of the as-prepared Gd₂O₃ nanotubes was also evaluated in this work through the use of conventional cell culture method by estimating the cell viability (in per cent) after a short-term exposure to the nanotubes under physiological environment. Epithelial cells (ARPE-19) were obtained from the American type Culture Collection and were cultured in Corning 75 cm² cell culture flasks. 90% 1:1 mixture of Dulbecco's modified Eagle medium (Gibco) and Ham's F12 medium containing 1.2 g l⁻¹ sodium bicarbonate, 2.5 mM L-glutamine, 15 mM HEPES and 0.5 mM sodium pyruvate was supplemented with 10% FBS (fetal bovine serum). Cells were cultured in an incubator at 37 °C at 5% CO₂ and the medium was changed approximately every 2 days. The cytotoxicity was assessed by MTT assay. The cells were harvested in log phase growth stage and seeded in 96-well (10⁴ cells/well) overnight and treated with the samples at different concentrations. The cells were then incubated for an additional 48 h. After 48 h, cells were incubated with

10% MTT agent for 4 h. Then the medium was replaced with 200 μ l of DMSO and the absorbance was monitored by an ELISA reader at a wavelength 570 nm. Cell viability was calculated by the following equation: $\text{Cell viability (\%)} = (A_{\text{sample}}/A_{\text{control}}) \times 100\%$

5-3 Results and discussion

5-3.1 Characteristics of Gd₂O₃ nanotube

In this study, poly(alkylene oxide) block polymer (designated EO₂₀PO₇₀EO₂₀; Pluronic P123) was used as a soft template for the synthesis of Gd₂O₃ nanotube. A sol-gel process was employed by hydrolyzing organometallic gadolinium isopropoxide in the presence of P123 templates. The template was removed by calcination at 600 °C for 6 h in air and a tubular nanostructure was evolved. TEM analysis indicated, along [100] and [110] (Figure 5.1(a) and (b), respectively), that mesoporous channels array along [110] was clearly observed. The nanostructure was examined using large-angle X-ray diffraction (LA-XRD), where the resulting pattern shows nine characteristic peaks, as that of cubic crystalline Gd₂O₃ (JCPDS No. 011-0604), in Figure 5.2(a), having intensive and sharp diffraction peaks, indicating a highly crystalline Gd₂O₃ framework with spatial group Ia₃. The unit cell parameter was calculated with the value of $a_0 = 1.080$ nm, which is consistent with the literature value ($a_0 = 1.081$ nm). The Scherrer equation was applied in the estimation of average particle size based on the full widths at half maximum (FWHM) of the XRD pattern at Gd₂O₃ (222) reflection and the resulting particle size was estimated to be ca. 12 nm. Figure 5.2(b) illustrates the small-angle XRD (SA-XRD) pattern of Gd₂O₃ nanotube where a characteristic reflection of the p6mm hexagonal structure at $2\theta = 1.54^\circ$ is observed and the corresponding spacing (d_{spacing}) is indexed with $d_{100} = 5.73$ nm. The hexagonal unit cell parameter (a_0) of 6.62 nm was calculated from assuming a (100) reflection of the hexagonal array of open pores of the Gd₂O₃ nanotube. This finding also indicates that a hexagonal arrangement of the tubular nanostructure evolved upon Gd₂O₃ synthesis.

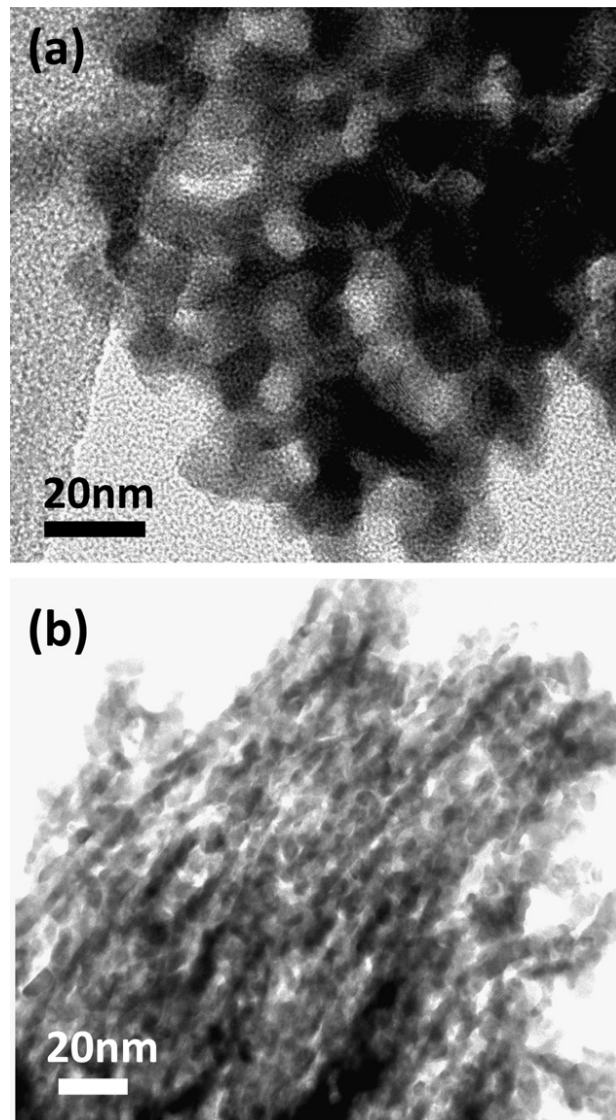


Figure 5. 1 TEM images of the Gd_2O_3 nanotube of (a) along [100] and (b) along [110].

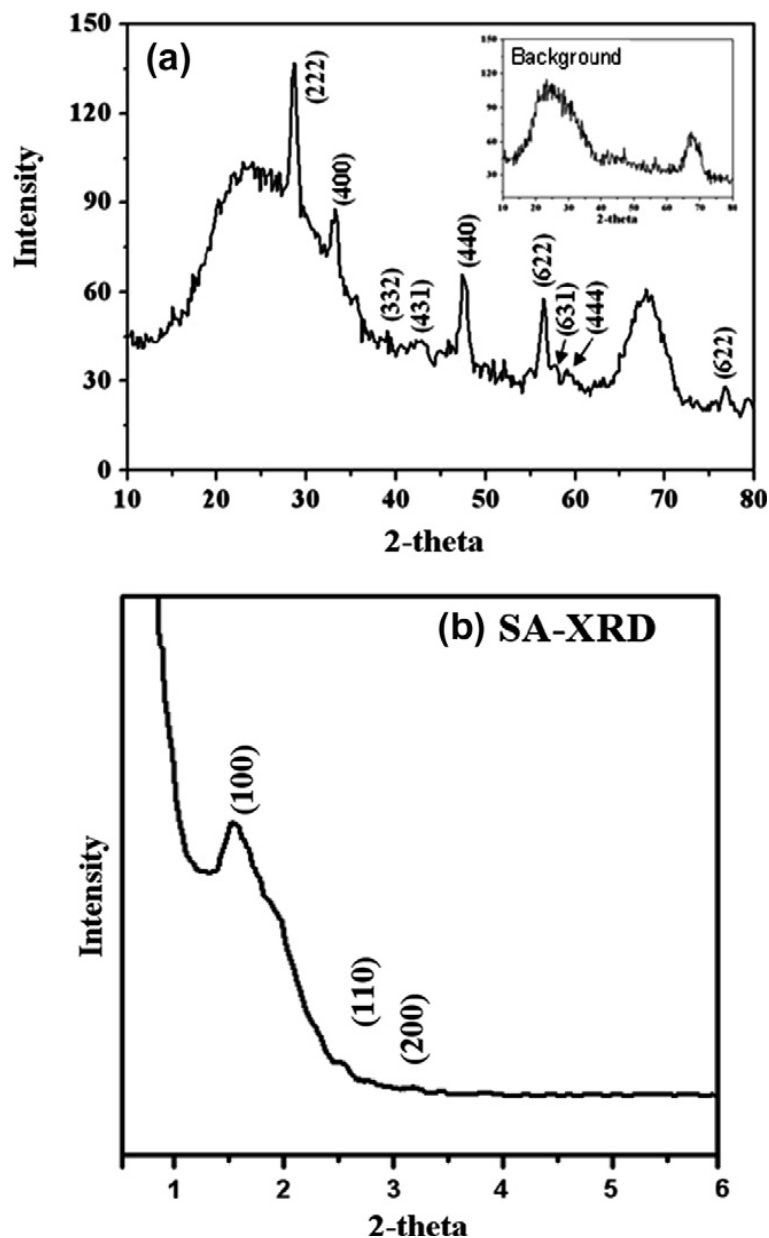


Figure 5. 2 (a) Large-angle XRD pattern of the Gd_2O_3 nanotube; the indexing is based on $a_0 = 1.08$ nm (cubic symmetry, $Ia3$) and (b) small-angle XRD pattern of the Gd_2O_3 nanotube; the indexing is based on $a_0 = 6.54$ nm ($p6$ mm).

Transmission electron microscopy analysis with electron diffraction and energy-dispersive spectrum of the Gd_2O_3 nanotube is given in Figure 5.3. A close examination of Figure 5.3(a) indicates that a hollow channel was constructed as a bundle of Gd_2O_3 nanotubes. The tubular nanostructure of the sample can be further confirmed with a sharp contrast between the edge and the central part of the Gd_2O_3 nanotubes. These

nanotubes are essentially constructed as a result of well-ordered assembly of Gd_2O_3 nanocrystals along the long axis of the nanotube to form the wall of the nanotube. The wall thickness is distinguished readily by the darker contrast to be about 10-20 nm, which, on average, is the same order of magnitude as the estimated size of primary particle, indicating a single-particle wall architecture. The length of the Gd_2O_3 nanotube is ca. 200 nm in Figure 5.3(a). High-resolution TEM examination, as shown in Figure 5.3(b), clearly shows from the lattice image of Gd_2O_3 nanoparticles that the estimated value of $d_{222} = 3 \text{ \AA}$ corresponds to $d_{222} = 3.1 \text{ \AA}$ of the (222) peak of cubic Gd_2O_3 in LA-XRD, indicating that the hexagonal walls are constructed by self-assembly of highly crystalline Gd_2O_3 nanoparticles. Electron diffraction patterns on the walls, illustrated in Figure 5.3(c), clearly exhibit characteristic rings associated with (222), (440), (332), (431), (440) and (622) crystal planes of the Gd_2O_3 cubic phase, which further substantiated a highly crystalline nature of the Gd_2O_3 nanoparticles. The energy-dispersive spectral analysis, Figure 5.3(d), also shows that no other impure elements, except Gd and O elements, are detected, indicated a highly chemically pure Gd_2O_3 phase.

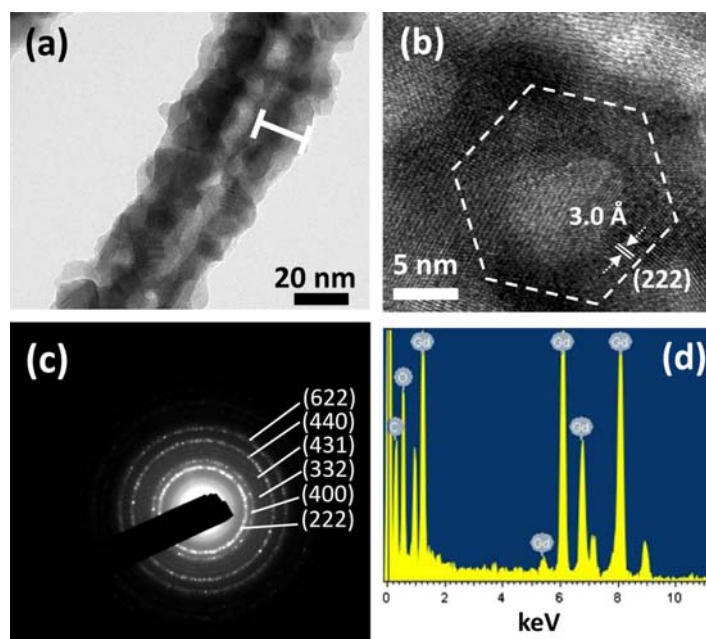


Figure 5. 3 (a) TEM images, (b) high-resolution TEM (HRTEM) image, (c) ED pattern and (d) EDS of the Gd₂O₃ nanotube.

Nitrogen adsorption isotherms and a corresponding pore size distribution of the Gd₂O₃ nanotube are shown in Figure 5.4. The adsorption isotherm (Figure 5.4(a)) shows a typical type-IV profile with a clear H4-hysteresis loop, which is a typical characteristic of porous materials. The uptake at high pressure was associated with the empty spaces between the particles. Brunauer-Emmett-Teller (BET) analysis gave a specific surface area of 68 m² g⁻¹ and pore volumes of 0.11 cm³ g⁻¹. In addition, the Gd₂O₃ nanotube shows a bimodal pore size distribution in the range of 2-5 nm and 15-30 nm (Figure 5.4(b)). A closer TEM examination (Figure 5.4(c)) indicated that the Gd₂O₃ nanotube appears to construct with two types of pores: firstly, an arranged one with pore size of ca. 5 nm; and secondly, a sparingly, randomly distributed pore with a size of 15-30 nm. The former is characterized as a result of hierarchical development along the block copolymer chain upon nucleation and polycondensation of the Gd precursor, whilst the randomly distributed larger mesopores may result from the possibility of undesired micellar nanostructure development over which an edge-edge or face-face contact or other possible contact combination gives rise to

larger voids among the tubular structure. On this basis, it is reasonable to believe that the compositional ratio between the Gd precursor and a corresponding copolymer may be less optimized, resulting in a trace amount of the unreacted copolymer that gives rise to such sparingly distributed pores in the final nanotube.

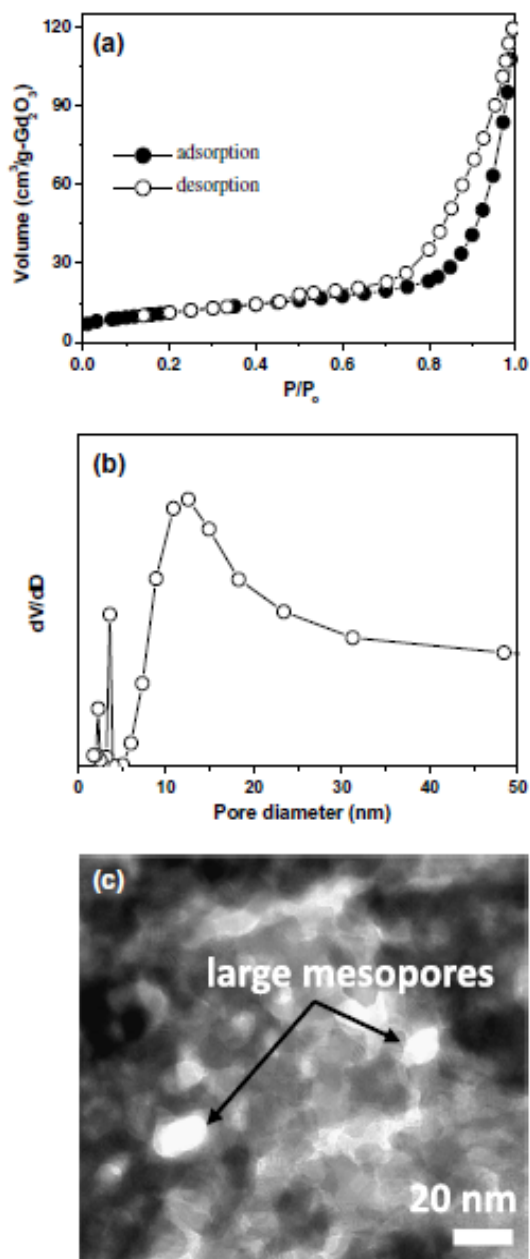
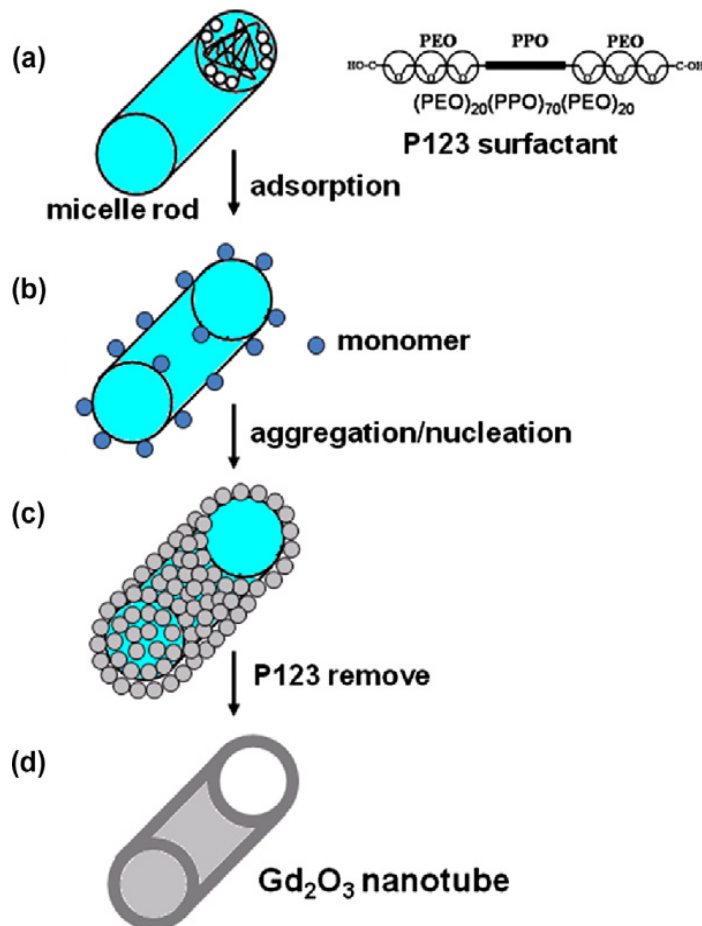


Figure 5. 4 (a) N₂ sorption isotherms of the Gd₂O₃ nanotube; (b) showing the corresponding pore size distribution and (c) TEM image of the Gd₂O₃ nanotube showing order and larger pores.

5-3.2 Formation mechanism of Gd₂O₃ nanotube

Such a soft-templating method has been observed frequently in a number of supramolecular-directing systems ^[215]; a self-assembly of the templates (surfactants, such as P123) in the solution system to form the micellar structure of hexagonal arrays can occur ^[216], as illustrated in Scheme 5.1(a). At the beginning of the sol-gel reaction, a large amount of monomers was formed by hydrolysis of organometallic gadolinium isopropoxide. When the concentration of the monomers in the solution reached a critical value, the monomers energetically start an interaction toward the surfaces of the P123 micelles, possibly through a carbonyl group, -C=O, of the copolymer associated with the hydroxyl group, Gd-OH, along the hydrolyzed Gd monomer (Scheme 5.1(b)). The assembly mechanism for such an interaction can be a surfactant-metal monomer complexation, as a result of, for example, electrostatic, hydrogen bonding, and/or van der Waals forces to direct the evolution of assembled nanostructure ^[196]. Then, Gd-containing nucleus can be evolved, originating from the adsorbed Gd monomers on the copolymer micellar surface (Scheme 5.1(c)). We speculate that the nucleation process is a quasi-heterogeneous behavior and continuously proceeded until most of the monomers were consumed. After then, the concentration of monomers started to decrease below the critical value until the nucleation process ceases completely. An energetically favored formation of the nuclei on the P123 micellar surface will slow down the growth of the nuclei and by contrast, form more nuclei along the micellar surface. As a result, the entire nucleation and growth process was largely dominated in the nucleation stage, resulting in the formation of an enormous amount of tiny particles on the micellar surface. In other words, upon nucleation and growth, the P123 micelles act as a functionalized surface, which could preferentially increase the speed of nucleation and decrease in the meantime the rate of crystal growth ^[217]. As illustrated in Scheme 5.1(d), the templates were pyrolytically removed and aggregates further oxidized into Gd₂O₃ nanocrystals. Since the nucleation proceeds on the micellar surface, resulting

nanocrystal development is virtually conformed to the geometry of the micelles and stacks orderly, resulting in a final nanotube shape with a hexagonal packing arrangement.



Scheme 5. 1 The formation mechanism of Gd_2O_3 nanotube.

5-3.3 IBU loading and release from Gd_2O_3 nanotubes

Ibuprofen, an anti-inflammatory drug, was used as model molecule to demonstrate the encapsulation and eluting behavior of the Gd_2O_3 nanotube. From absorbance FTIR spectra of Gd_2O_3 nanotube after IBU uptake, in comparison with the spectrum of the ibuprofen and the neat Gd_2O_3 nanotube (Figure 5.5), the neat sample (spectrum 5a) shows characteristic bands of Gd_2O_3 : the bands around 3460 and 1650 cm^{-1} are due to the OH stretching vibration and OH deformation vibration, respectively. The absorption appearing around 1510 and 1410 cm^{-1} corresponds to CO asymmetric vibration. The band at $\sim 540\text{ cm}^{-1}$ is

assigned to the Gd-O vibration mode of cubic Gd₂O₃, which is in agreement with Ref. [211]. Spectrum 5b, related to samples after IBU incorporation, showed additional peaks around 3000-2850 cm⁻¹ assigned to the symmetric and asymmetric stretching vibrations of -CH_x groups, due to the ibuprofen alkyl chain. In addition, pure IBU shows a strong carboxyl band at 1715 cm⁻¹, which corresponds to the carboxyl group (COOH) present in IBU. Gd₂O₃ nanotube loaded with IBU showed the disappearance of a strong carboxyl band at 1715 cm⁻¹; instead, a new peak at 1558 cm⁻¹ appeared which may be attributed to the asymmetric stretching vibration of COO⁻, since carboxylic acid salts exhibit a strong characteristic COO⁻ asymmetric stretching band in the range of 1650-1550 cm⁻¹ [218]. This observation indicates a deprotonation of the IBU molecule when it interacted with the Gd₂O₃ nanotube, suggesting a good chemical affinity between the IBU and the nanotubes. The IBU encapsulation efficiency of 22% can be easily achieved through a simple impregnation method.

The release of IBU from the Gd₂O₃ nanotube shows a near linear profile over a short-term period, i.e. ~10 min, of immersion, after 24 h incubation in the IBU-containing solution, at physiological environment (Figure 5.6(a)). The release amount of IBU in the testing period takes about 4.60% of the total amount of IBU encapsulated within the nanotubes. This finding suggests that the encapsulated IBU molecules in the Gd₂O₃ nanotube released in a zero-order kinetic at the initial stage of drug elution, which may be attributed to the strong interaction between IBU molecules and Gd₂O₃ nanotube, strongly regulating the release profile of the IBU molecule. Such an interaction, according to the aforementioned spectral analysis, may be a hydrogen bonding between the COO⁻ group of IBU and OH group on the surface of the nanotube. If it is true, dissociation of the hydrogen bonds occurred upon a strong association of water molecule, where the IBU was further protonated upon salvation and released from the nanotube. On this basis, this salvation-dissociation mechanism may dominate the eluting profile, rather than diffusion only,

resulting in a near zero-order kinetic. Such an eluting pattern is of practical interest and importance, since a burst-like elution behavior has frequently been observed in many existing bulk, film, or particulate drug-carrying systems, making an unfavorable drug release profile at the early stage of delivery.

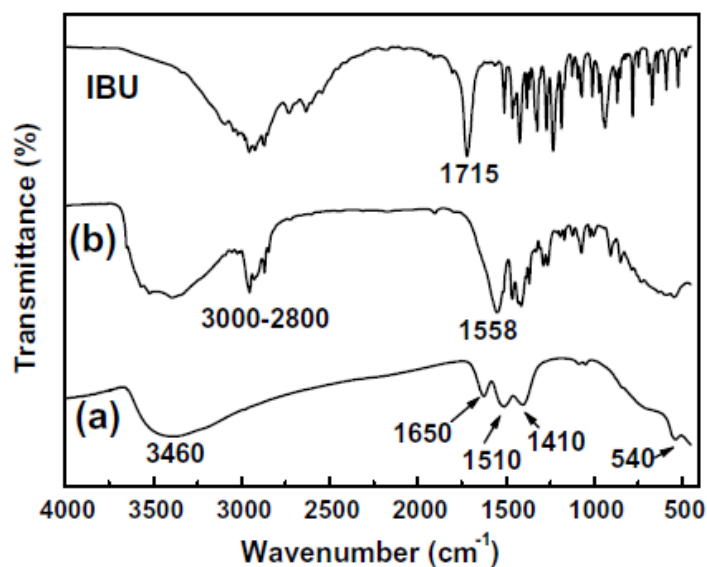


Figure 5. 5 FTIR spectra of (a) the neat Gd₂O₃ nanotube and (b) the Gd₂O₃ nanotube after IBU uptake and IBU.

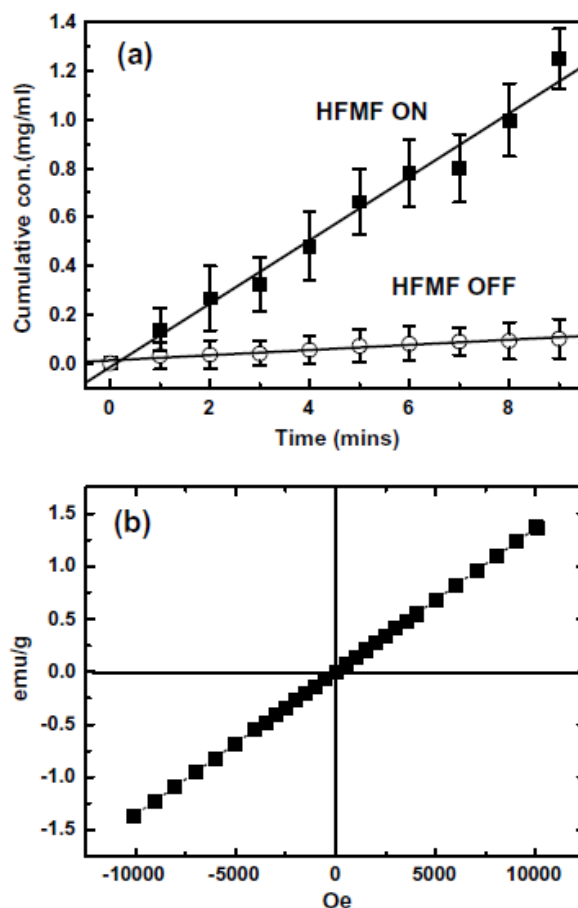


Figure 5. 6 (a) IBU release profiles from the Gd₂O₃ nanotube under the magnetic field switching on and off and (b) hysteresis loop analysis of the Gd₂O₃ nanotube.

5-3.4 Magnetically triggered IBU release from the nanotube

Upon applying a high-frequency alternating magnetic field (50 kHz and a power output of 15 W) to the IBU-containing nanotube for a period of ~10 min, a larger amount of drug (compared to the case without applying magnetic field) was detected, indicating that the IBU was released rapidly from the nanotubes under magnetic stimulus. Similar to the case without magnetic induction, the profile of drug released from the Gd₂O₃ nanotubes showed a linear increment with the stimulus time, i.e. a zero-order kinetic. This finding indicates a two fold effect: (1) the applied HFMF boosted the released amounts of IBU, but seemed not to alter the mechanism of release to any appreciable extent and (2) the Gd₂O₃ nanotubes exhibited a magnetic responsive behavior. For the latter, a magnetization curve was detected

and shown in Figure 5.6(b), where the curves show similar shape with negligible hysteresis. This indicates that the Gd₂O₃ nanotubes displayed paramagnetic behavior, although relatively weak in magnetization, indicating that the Gd₂O₃ nanotubes can be magnetized by an applied magnetic field. A plausible explanation for the mechanism of the magnetically triggered IBU release behavior can be that under high-frequency magnetic field, the Gd₂O₃ nanotubes were subjected to a resonance effect and gave rise to an increased pore size of the Gd₂O₃ network, making the Gd₂O₃ nanotubes more structurally loosened. Hence, the nanotubes swelled in the presence of the magnetic field and the structural change of nanotubes boosted the drug-release behavior. In addition, the magnetic-induced drug-release behavior suggests that the proposed salvation-dissociation mechanism can be promoted by increasing IBU dissociation from the nanotube, resulting in an increase in IBU eluting amount by 56.7% over the same elution period. It is suggested that both dissociation and nanotube swelling may interplay in the resulting elution profile.

Since the Gd₂O₃ has been well recognized as a contrast agent for clinical diagnosis, together with the drug-carrying and controlled elution abilities currently explored, it is reasonable to believe that a combined therapeutic functionality can be simultaneously achieved using the Gd₂O₃ nanotubes currently developed ^[219].

5-3.5 Cytotoxicity of Gd₂O₃ nanotube

In the cytotoxicity study (48 h exposure of ARPE-19 cell line), the results of the MTT assay (Figure 5.7) represented a measurable metabolic competence of the normal epithelial cells with the Gd₂O₃ nanotubes at different concentrations. At a lower concentration of the nanotubes, i.e. <100 µg ml⁻¹, the cell viability of about 100% was observed, suggesting that the Gd₂O₃ nanotubes, with a critically low concentration, exhibited relatively low to negligible toxicity with respect to the epithelial cells. However, above the critical concentrations, i.e. 500 µg ml⁻¹ and 1000 µg ml⁻¹, the cell viability illustrated a reduction to

78% and 66%, respectively, suggesting a certain toxic effect of the nanotubes with respect to the epithelial cells can be developed for a 48 h period. However, despite its cytotoxic effect, it was also found that the nanotubes currently developed showed a cytocompatible range for the nanotubes below, say, $500 \mu\text{g ml}^{-1}$. Taking its drug-carrying capacity determined above, i.e. 22%, it is noticeable that a drug payload of $110 \mu\text{g ml}^{-1}$ can be easily achievable. Such a payload can be therapeutically effective for a localized delivery of a drug, such as anti-cancer agent, which will be reported separately.

Although the preliminary studies ensure a cytocompatible region of the Gd_2O_3 nanotubes under current experimental control, extensive in vitro and in vivo evaluation is needed before assessing their suitability for practical in vivo anti-cancer treatment.

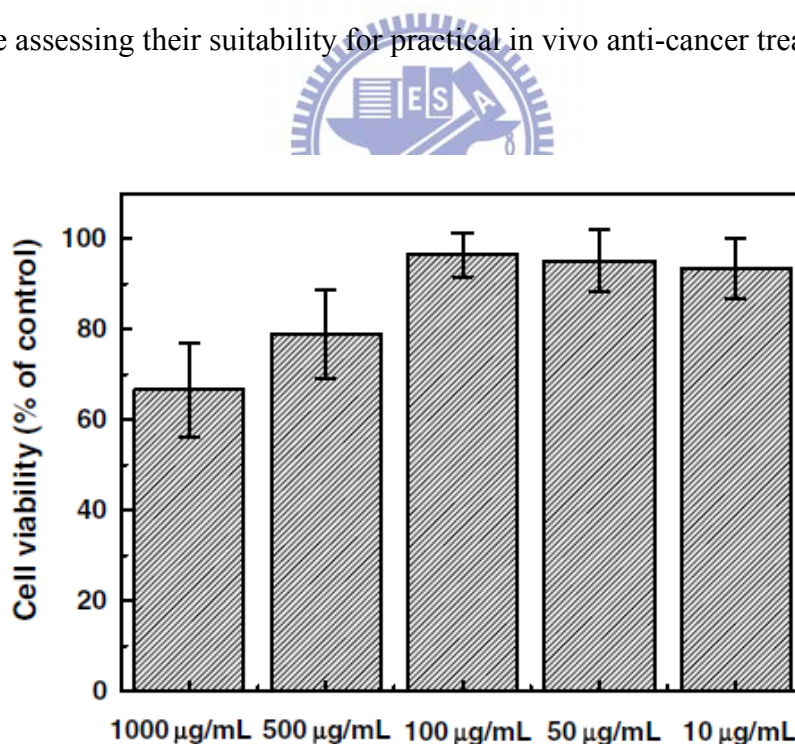


Figure 5. 7 Cell viability of ARPE-19 cells incubated for 48 h with different concentrations ($1000 \mu\text{g ml}^{-1}$, $500 \mu\text{g ml}^{-1}$, $100 \mu\text{g ml}^{-1}$, $50 \mu\text{g ml}^{-1}$, and $10 \mu\text{g ml}^{-1}$) of the samples.

5-4 Conclusion

Through the use of structure-directing macromolecules, associated with a sol-gel synthesis, a highly crystalline mesoporous Gd_2O_3 network with a tubular nanostructure was successfully prepared. The hierarchical development of the nanoporous Gd_2O_3 nanotube

originates from self-organization of the templating amphiphilic copolymer, where the templating molecule, after forming into micellar structure, provides numerous active sites for the nucleation and growth of the Gd precursor. Self-assembly of the Gd_2O_3 nanocrystals along the micellar surface of the copolymer gives rise to the formation of nanoporous Gd_2O_3 nanotubes after pyrolytic removal of the template. Such a nanoporous nanotube allowed the therapeutic substance, e.g. IBU in this case, to be effectively encapsulated and released in a linear fashion. More interestingly, the nanotubes exhibited a weak paramagnetic behavior which enables the encapsulated IBU to elution in a controllable profile upon a magnetic stimulus. Together with its well-known property as contrast agent in clinical diagnosis, the Gd_2O_3 nanotube is believed to provide combined therapeutic functionalities for medical applications.



Chapter 6

Bioactive TiO₂ Ultrathin Film with Worm-like Mesoporosity for Controlled Drug Delivery

6-1 Introduction

Titanium exhibits desired mechanical properties such as moderate elasticity, high strength-to-weight ratio, and biocompatibility. Hence, titanium and its oxidative derivatives, such as TiO₂, have long been employed for biomedical applications in the areas of dentistry, orthopedics, and osteosynthesis. However, titanium based implants with their surfaces have been realized not able to firmly attach to the host tissues due to fibrous capsule formed on titanium surface in vivo ^[220-221]. In order to avoid implant loosening and failure, the methods of coating bioactive thin films on implants have been developed, such as anodic oxidation ^[222], sol-gel technology ^[223-224], plasma spray ^[225], and sputtering ^[226]. Appropriate coatings are advantageous and even necessary for the acceptance and functioning of the implant. In several studies, TiO₂ thin film coatings was used to improve the hydrophilic properties of implants to favor osteoblast cell adhesion and enhanced the expressions of osteogenic genes ^[227-228]. Therefore, TiO₂ thin film coatings show a strong interfacial bonding between TiO₂ surface and living tissue ^[229]. In recent years, the coated implant can be viewed as a combinatory drug/medical device which represents an emerging new trend in nanotherapeutics. A combination of therapeutic drug and medical device can be integrated to increase the performance and life time of currently used implants and improve clinical compliance and life quality of patients ^[230]. On this base, either porosity or thickness of the resulting coating may consider critical as a drug reservoir for suitable therapeutic performance. Too thick coating such as several tens to hundred of micrometers of thickness has been declined in practice due to mechanical instability and potential adverse complications, such as inflammation caused by coating fragmentation after implantation

[231-233]. On the other hand, coating with desired pore size or porosity has been highlighted and is expected to be tunable according to the therapeutic molecules to be carried and delivered.

Hence, it is technically and medically important to design an ultrathin porous coating capable of carrying and delivering drug with reasonably time period for improved therapeutic performance, especially for hard-tissue implants. Since the discovery of the MCM-type mesoporous materials [148], great attention has been focused on the synthesis and characterization of surfactant templated mesoporous silica materials [234, 207]. Due to the possibility of the strict control of their pore size, pore structure, and surface properties, increasing interest has been directed to the exploration of mesoporous silica materials for drug delivery systems [235-236]. Furthermore, thin films of mesoporous oxide materials may offer more therapeutic opportunities for biomedical applications, particularly for implanted or invasive medical devices.

In this study, evaporation-induced self-assembly (EISA) method was used to synthesize mesoporous TiO₂ ultrathin films. Taking advantages of the simplicity of synthetic process, mesoporous TiO₂ thin films can be used to modify the surface and improved biofunctionality of medical implants. In the meantime, we also employ those mesopores of TiO₂ thin films to carry ibuprofen and vancomycin followed by a controlled release of the drug, for therapeutic purpose. Cytocompatibility and bioactivity of the resulting mesoporous TiO₂ ultrathin film were evaluated in vitro using osteoblast adhesion test and apatitic formation in the presence of acellular simulated body fluid, respectively.

6-2 Experiments

I cooperated with Ms. Chih-Shin Chao and Dr. Kun-Ho Liu of our group to prepare these samples in this study and the detailed preparation and characterization can be found in

Ms. Chao's master thesis [249]. Cell culture test was prepared by Wei-Lin Tung of our group.

I thank Ms. Chao, Ms. Lin, and Dr. Liu for this work.

6-2.1 Preparation of the mesoporous TiO₂ ultrathin films

Titanium tetraisopropoxide (TTIP, 98%, ACROS), acetyl acetone (AcAc), and 2-propanol was stirring as precursor solution. The surfactant block copolymer P123 [HO(CH₂CH₂O)₂₀(CH₂CH(CH₃)-O)₇₀(CH₂CH₂O)₂₀H, Aldrich] was slowly added to the precursor solution. The obtained solution was hydrolyzed at a pH 1.2 condition. The molar ratio of P123/TTIP/AcAc/IPA was 0.03/1/0.5/35. The mixture was stirred for 3 h and spin-coated on silicon (100) or glass substrate at 2000 rpm-30 s. Finally, the spin coated films were calcined at 450 °C for 4 h.



6-2.2 Characterization of the mesoporous TiO₂ ultrathin films

The resulting ultrathin films on silicon substrate were characterized using powder X-ray diffraction (PXRD) measurements (MAC Science MXP18AHF XRD, with Cu K α radiation source, $\lambda = 1.5418 \text{ \AA}$). TEM micrographs, electron diffraction patterns were recorded by a JEOL JEM-2100F electron microscope equipped with an Oxford energy-dispersive spectrometer (EDS) analysis system. For the cross-sectional TEM characterization, the calcined sample was first cleaved into small pieces of $\sim 2\text{mm} \times 3 \text{mm}$, then pairs of such pieces were glued to each other through face-to-face contact. The glued stacks were mechanically ground and polished into wedge shapes, followed by chemical polishing with Rodel NALCO 2354 CMP fluid. Fourier transformed infrared spectroscopy (ATRFTIR) spectra were recorded on a spectrometer (Bomem DA8.3, Canada) with a KBr plate. The FTIR spectra were taken with a resolution of 2 cm^{-1} in the range of $4000\text{-}450 \text{ cm}^{-1}$.

6-2.3 Loading and release behavior of IBU

First, the films ($2 \times 2 \text{ cm}^2$) were impregnated with a 2 ml of ibuprofen solution (IBU) in ethanol (5 mg/ml, 10 mg/ml, 40 mg/ml) for a time period of 24 h and were dried at $50 \text{ }^\circ\text{C}$. Then, the films were washed with 10 ml of phosphate buffer saline (PBS) to remove the excess IBU resided along the surface region. The amount of drug encapsulated in the mesoporous TiO_2 film was then calculated by the initial amount of drug subtracting the drug left in the supernatant. Encapsulation efficiency (EE) of drug was obtained as described below

$$\text{EE (\%)} = (\text{A}-\text{B})/\text{A} \times 100$$

where A is the total amount of the drug and B is the amount of drug remaining in the supernatant. In order to compare the drug loading and release behavior of IBU and VAN, the films ($2 \times 2 \text{ cm}^2$) were impregnated with 2 ml of (1) IBU in ethanol and (2) vancomycin (VAN) in DI water of 10 mg/ml concentration, respectively, for 24-h period, followed by washing with 10 ml PBS to remove surface drugs and dried at $50 \text{ }^\circ\text{C}$. For drug release evaluation, the drugloaded films were immersed in a PBS solution and concentration of released IBU or VAN was measured by UV/Vis spectrophotometer at wavelength of 254 nm and 282 nm, respectively.

6-2.4 Cell culture test of the mesoporous TiO_2 ultrathin films

The mouse bone marrow osteoblastic cells, 7F2, were cultured in medium containing 90% alpha minimum essential medium with 2mM_L -glutamine and 1 mM sodium pyruvate without ribonucleosides and deoxyribonucleosides, 10% fetal bovine serum and maintained in humidified atmosphere with 5% CO_2 at $37 \text{ }^\circ\text{C}$. Then, the cells seeded with a density of $5 \times 10^3 \text{ cells/cm}^2$ on different specimen surfaces for cytocompatibility evaluation.

After 48 h of incubation, cells were fixed in 3.7% formaldehyde and permeabilization was performed with 0.1% triton-100 in PBS. 7F2 cells were washed with PBS and then

stained with Rhodamine-Phalloidin (1 $\mu\text{g}/\text{ml}$) at 37 $^{\circ}\text{C}$ for 1 h. Then the cell morphology was investigated by fluorescent microscope ($\times 400$, eclipse, TE2000-U, Nikon). Three samples of each group, i.e., control, TiO_2 film without calcinations, TiO_2 film with calcinations, were prepared for statistical analysis and five randomly selected images from one sample substrate were captured and calculated. The cell number was collectively measured and averaged for those three samples and presented as mean \pm SD.

6-2.5 Bioactivity of the mesoporous TiO_2 ultrathin films

The mesoporous TiO_2 ultrathin films ($1 \times 1 \text{ cm}^2$) were immersed in 10 ml SBF with ion concentrations (Na^+ 213.0, K^+ 7.5, Ca^{2+} 3.8, Mg^{2+} 2.3, Cl^- 221.7, HCO_3^- 6.3, HPO_4^{3-} 1.5, SO_4^{2-} 0.8 mM), nearly equal to those in human blood plasma, at 36.5 $^{\circ}\text{C}$ and contained in a polystyrene bottle. The SBF was prepared by dissolving reagent grade chemicals of CaCl_2 , $\text{K}_2\text{HPO}_4 \cdot 3\text{H}_2\text{O}$, KCl , NaCl , $\text{MgCl}_2 \cdot 6\text{H}_2\text{O}$, NaHCO_3 , and Na_2SO_4 in DI water and buffered at pH 7.4 using tris(hydroxymethyl)-aminomethane ($(\text{CH}_2\text{OH})_3\text{CNH}_2$) and 1 M HCl at 36.5 $^{\circ}\text{C}$. After a given immersion period, the films were removed from the SBF, gently washed with DI water, and dried at 40 $^{\circ}\text{C}$. The surfaces of the immersed films were analyzed by SEM (JEOL 6500) and XRD (Shimadzu XRD-6000, $\lambda = 1.541 \text{ \AA}$).

6-3 Results and discussion

6-3.1 Characteristics of mesoporous TiO_2 ultrathin film

To obtain mesoporous TiO_2 ultrathin film, poly (alkylene oxide) block polymer (designated $\text{EO}_{20}\text{PO}_{70}\text{EO}_{20}$; Pluronic P123) was used as a soft template. A sol-gel process was employed by hydrolyzing organometallic titanium isopropoxide in the presence of P123 templates. After condensation, the mesoporous structure of TiO_2 film was evolved by removing the template at 450 $^{\circ}\text{C}$ for 6 h in air. The calcined TiO_2 film was examined using large-angle XRD (LA-XRD), where the resulting pattern, Figure 6.1 shows four

characteristic peaks of the basal reflections of (101), (112), (200), and (211) planes at $2\theta = 25.4^\circ$, 38.3° , 48.1° , 55° , respectively, corresponding to the tetragonal crystalline TiO_2 phase (JCPDS No. 21-1272). Intensive and sharp diffraction peaks indicated highly crystalline TiO_2 frameworks with space group $I4_1/amd$ (141). Figure 6.2 shows the small-angle X-ray diffraction (SA-XRD) patterns of the as-synthesized and calcined mesoporous TiO_2 films. In Figure 6.2(a), a characteristic reflection of the $p6mm$ hexagonal structure at $2\theta = 0.96^\circ$ and $2\theta = 1.66^\circ$ is observed and the corresponding spacing (d_{spacing}) is indexed with $d_{100} = 9.2$ nm and $d_{110} = 5.32$ nm, respectively. The hexagonal unit cell parameter (a_0) of 10.6 nm was calculated from assuming a (100) reflection of the hexagonal array of mesoporous TiO_2 film. Those aforementioned results indicate that the as-synthesized mesoporous TiO_2 film exhibits highly ordered arrays. After calcination, Figure 6.2(b) shows a single broad diffraction peaks at $2\theta = 1.2^\circ$ with the corresponding spacing (d_{spacing}) indexed with $d_{100} = 7.36$ nm, being suggestive of mesostructural order [237].

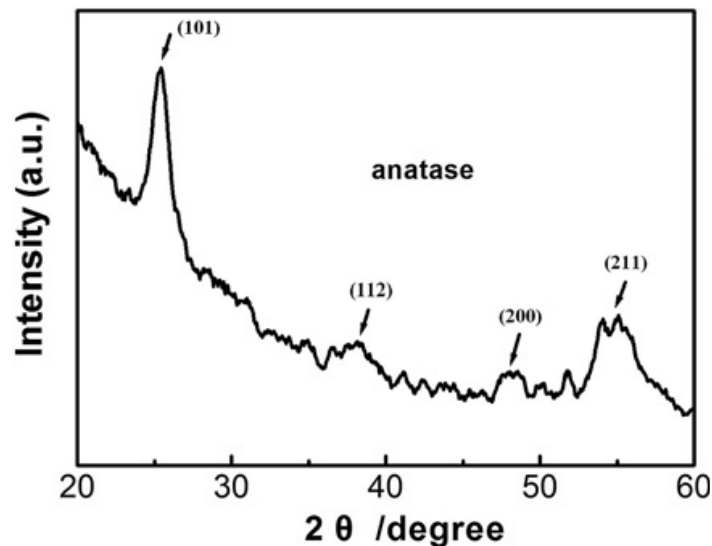


Figure 6. 1 Large-angle XRD pattern of the mesoporous TiO_2 ultrathin film [249].

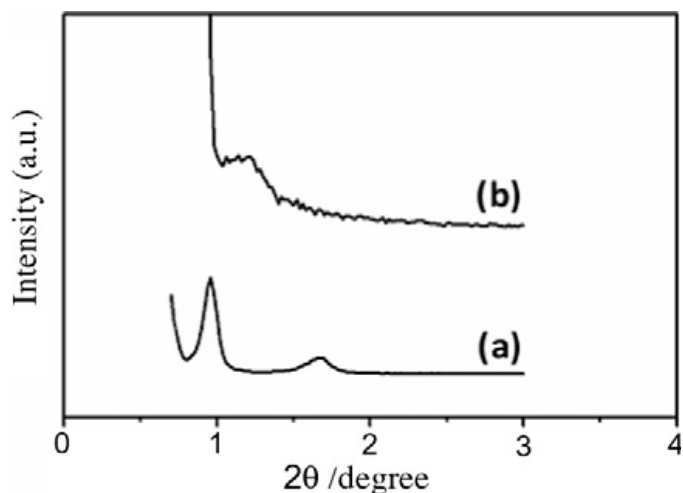


Figure 6. 2 Small-angle XRD pattern of the mesoporous TiO₂ ultrathin film (a) before and (b) after calcinations ^[249].

Figure 6.3 shows the cross-sectional TEM images of the calcined mesoporous TiO₂ film, whereas a thickness of ~126 nm with uniform worm-like mesoporous structure can be found. The thickness of the solid framework was ca. 5-8 nm which is thicker than that of pore size (ca. 4 nm). It is well-known that high-temperature calcination causes severe shrinkage of TiO₂ film structure ^[238-239], the structure mesoporous TiO₂ film is therefore expected to be disturbed while calcining at high temperatures and in this case, as large as ~20% of shrinkage was measured. However, experimental observation indicated structural integrity reminded intact for the mesoporous TiO₂ film, where a thicker wall of the mesoporous film is expected to keep the structure from collapsing during calcination ^[240]. In addition, the uneven framework is considered to result in the broad diffraction peak of SA-XRD pattern. The worm-like channels that are more or less regular in diameter were packed in random forming a three dimensional mesoporous structure, which may also contribute to the single broad peak observed over the low-angle region. It exhibits mesoporous TiO₂ framework with well-crystalline nanostructure, corresponding to the intensive diffraction peak for the LA-XRD pattern, as the high resolution TEM image given in the inset of Figure 6.3. Both the XRD and TEM analyses confirmed the formation of

worm-like mesoporous structure of the TiO₂ film coating through the use of sol-gel synthesis, associated with the presence of a molecular template. The open pore structure of the resulting TiO₂ film permits its potential capability to carry pharmaceutical substances for improved therapeutic purposes. The worm-like structure developed throughout the mesoporous ultrathin film was believed to be a result due to the molecular assembly of the soft template upon rigid framework development upon the synthesis, which also provides a highly tortuous path for a potential sustained delivery of therapeutic molecules.

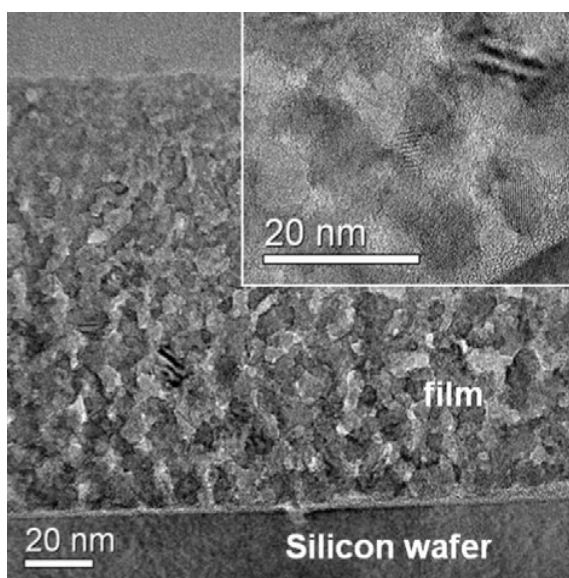


Figure 6. 3 TEM image of the mesoporous TiO₂ ultrathin film after calcinations ^[249].

6-3.2 Drug loading and release behavior from mesoporous TiO₂ ultrathin film

Ibuprofen (IBU), an anti-inflammatory drug, was used as model molecule to demonstrate the encapsulation and eluting behavior of the mesoporous TiO₂ film. From the absorbance FTIR spectra, the mesoporous TiO₂ ultrathin film (Figure 6.4(a)) shows characteristic bands of TiO₂: the bands around 3230 and 1620 cm⁻¹ are due to the OH stretching vibration and OH deformation vibration, respectively, which can be attributed to the surface-adsorbed H₂O and hydroxide group (-OH) of TiO₂ ^[241]. The broad band at 450-900 cm⁻¹ can be ascribed to the vibration of Ti-O bond in TiO₂ ^[242]. In addition, pure

IBU shows a strong carboxyl band at 1730 cm^{-1} , which corresponds to the carboxyl group (C = O), as shown in Figure 6.4(c). The absorption appearing around 1430 and 1250 cm^{-1} corresponds to CO asymmetric vibration. After loading of IBU, Figure 6.4(b), it shows additional peaks at 2970 - 2880 cm^{-1} assigned to the symmetric and asymmetric stretching vibrations of $-\text{CH}_x$ groups, due to the IBU alkyl chain. In addition, the disappearance of a strong carboxyl band at 1730 cm^{-1} ; instead, a new peak at 1550 cm^{-1} appeared which may be attributed to the asymmetric stretching vibration of COO^- , since carboxylic acid salts exhibit a strong characteristic COO^- asymmetric stretching band in the range of 1650 - 1550 cm^{-1} [218]. This observation indicated a deprotonation of the IBU molecule when it was interacted with the mesoporous TiO_2 film, suggesting a strong chemical affinity between the IBU and the ultrathin film. Such an interaction, according to the spectral analysis aforementioned, is likely a hydrogen bonding between the carboxyl group of IBU and hydroxyl group of the TiO_2 film. In addition, the FT-IR spectrum of vancomycin shows in Figure 6.4(d). Additional well-pronounced bands in the range from 1700 to 1000 cm^{-1} and from 3600 to 2800 cm^{-1} are the characteristic bands of vancomycin. For instance, a strong carboxyl band at 1680 cm^{-1} , characteristic band of a C-C mode of vibration in the aromatic rings at 1493 cm^{-1} , and N-H and/or O-H stretching vibration at 3400 - 3200 cm^{-1} , respectively. While loading with vancomycin (VAN), FT-IR spectrum, Figure 6.4(e), depicts characteristic bands at 3400 cm^{-1} and 1650 cm^{-1} designated the stretching and bending vibrations of the O-H bond. Compared to the FT-IR spectra of TiO_2 , three new bands were observed for TiO_2 after incorporation of VAN at 1510 cm^{-1} , 1420 cm^{-1} , and 1230 cm^{-1} , which were attributed to aromatic adsorption from the VAN molecule. It is indicated that the surface of the mesoporous TiO_2 film was covered with sufficient amount of vancomycin.

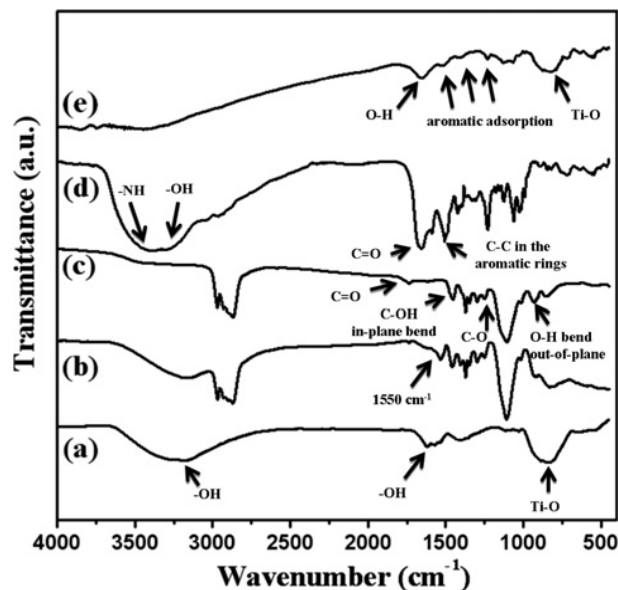


Figure 6. 4 FTIR spectra of (a) the mesoporous TiO₂ ultrathin film, (b) the IBU loaded mesoporous TiO₂ ultrathin film, (c) pure IBU, (d) pure VAN, and (e) the VAN loaded mesoporous TiO₂ ultrathin film.

When different concentrations of IBU (5 mg/ml, 10 mg/ml, and 40 mg/ml) were incorporated in the mesoporous TiO₂ film, a drug encapsulation efficiency of 10%, 18%, and 5%, respectively, was observed. With the increase of IBU solution, a saturated drug payload of ca. 2 mg/ml was observed. Figure 6.5 also indicates a slower release of IBU from the mesoporous film with the higher drug payload (immersed in 10 or 40 mg/ml) than that from the film with lower drug payload (i.e., in the case of 5 mg/ml). For the latter, IBU was depleted in about 10 h, whilst longer release profile of 30 h was achieved for the higher drug-loaded films. The slower release profile suggested that the release of IBU was effectively inhibited upon diffusion outward the TiO₂ film. Such a slower diffusion is believed to be related with tortuous porosity of the films where the IBU was loaded into deeper regions of the pore structure while impregnating with the high-concentrated IBU solution. Furthermore, as more drug molecules encapsulated in the mesoporous structure of the TiO₂ film, limited space may also restrict IBU diffusion, rendering a slower release profile, as evidenced in Figure 6.5.

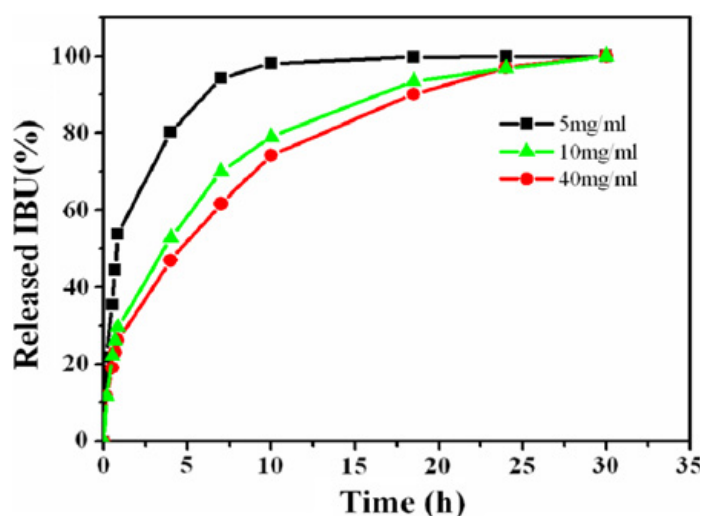


Figure 6. 5 Mean cumulative ibuprofen release behavior from the mesoporous TiO₂ ultrathin film with different immersed concentration.

To further illustrate the size effect of the drug molecule on a subsequent release behavior from the mesoporous TiO₂ film, vancomycin was employed, which has a larger, by a factor of ca. 14 times, molecule size of $3.2 \times 2.2 \text{ nm}^2$ [243], compared with IBU, $\sim 1 \times 0.5 \text{ nm}^2$, and has a dimension closed to the pore size of the mesoporous TiO₂ film, as illustrated in Figure 6.6(a) and 6.6(b). While impregnation with drug solution of 10 mg/ml concentration, VAN reached much lower drug payload of 0.75 mg/ml and showed faster release profile than that of IBU, Figure 6.6(c), where $\sim 95\%$ VAN released in about 10 h and as high as 50% being burst released, whilst $\sim 80\%$ for the IBU over a 10 h period. Larger molecule size experiences more difficult in drug loading inside the pores, and this renders more surface-bounded drug and less drug resided within mesopores, giving rise to an early-phase burst, by 50% and a higher release rate within the first hour. In order to further understand the release behavior, diffusion exponent n was determined by the use of Power Law [244].

$$M_t/M_0 = kt^n, (M_t/M_0 \leq 0.6)$$

where M_t is the amount of drug released at time t , M_0 is the amount of drug loaded, k is a rate constant and n is the diffusion exponent related to the diffusion mechanism. Herein, the diffusion exponent n and constant K calculated from the drug release profiles are 0.08, 0.48 and 33.2, 4.01 for VAN and IBU, respectively ($R^2 = 0.99, 0.97$ for VAN and IBU, respectively). There are three types of release profiles that can be categorized. As the diffusion exponent n is closed to zero, the drug release rate remains constant until the exhaust of drug. The second common type of release kinetics is first-order release or diffusion-controlled release when n is closed to 0.5. The release rate is proportional to the mass of drug contained within the device. It means the release rate declines exponentially with time, approaching a release rate of zero as the device approaches exhaustion. When the n is closed to one swelling-controlled release kinetics is dominated. From the results, the diffusion exponent n of VAN closed to zero corresponds to a zero-order release kinetic while the diffusion exponent n of IBU closed to 0.5 showed Fickian diffusion kinetics. Zero-order release kinetic of VAN suggested a time-independent release that may be the cause of larger molecules tending to aggregate on the surface of TiO_2 films. On the other hand, IBU showed a diffusion-controlled release behavior which indicated the release rate of IBU molecules from TiO_2 film determined by the diffusion rate of molecules. Hence, it can be explained that smaller IBU molecules showed slower release rate than larger VAN molecules. Besides, from FTIR analysis aforementioned, it is reasonably to believe that both the pore size and chemical interaction between the drug molecule and TiO_2 surface play critical role in dominating the resulting release kinetics. Although it is hard to give a clear-cut of the released amount of the drugs that dominated by specific releasing mechanism, the interplay between these factors will depend on the relative amount of drug adsorbed onto and encapsulated into the porosity structure of the TiO_2 film. In general, this comparison suggests the worm-like nanostructure of the ultrathin film coating imparting considerable amount of porosity for drug load and in the meantime, increased the length of

pathway for drug diffusion. Both contributions, associated with the chemical affinity, allow drug elution for time duration of 30 h over such an ultrathin coating. However, extended release with a controllable dosing quantity can be further designed, albeit not the main focus of this preliminary investigation, upon nanostructural optimization included coating thickness, porosity, and pore size through the use of soft-template synthesis for specific biomedical practices.



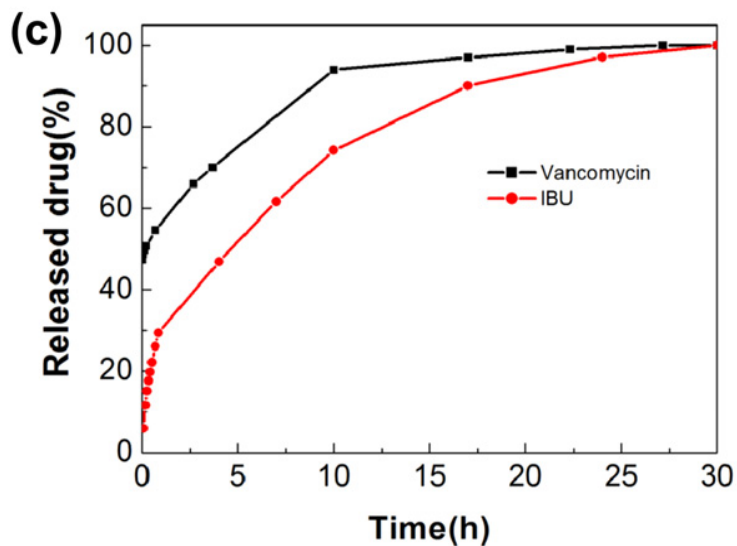
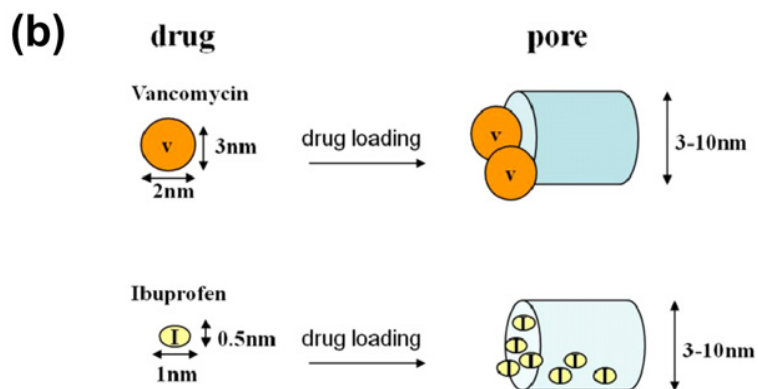
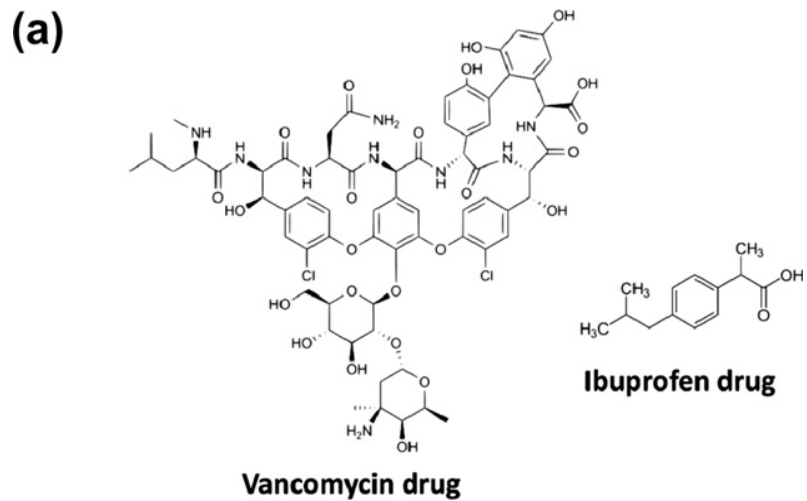


Figure 6. 6 The molecular structure of ibuprofen and vancomycin drugs (a), the illustration of drug loading method for various molecular size (b) and those drugs delivery profile during 30 h (c) ^[249].

6-3.3 Cell culture of mesoporous TiO₂ film

The cellular behavior on the mesoporous TiO₂ film was examined by culturing murine osteoblast cells (7F2) on coated surfaces. Figure 6.7 shows the cell adhesion and spreading on the mesoporous TiO₂ film with red fluorescent action skeleton by fluorescent microscopy. Osteoblast cells were seeded on the surface with three different morphological structures: mesoporous TiO₂ film before (Figure 6.7(b)) and after calcination (Figure 6.7(c)), and glass substrate (Figure 6.7(a)) as control. All surfaces favored the adhesion and growth of 7F2 murine osteoblast cells, with no sign of cytotoxicity was detected. For optical microscopic observation of the cell morphology and growth condition, which was shown ~60 percent confluency during the tested time, and it would be clear and easy to observe and calculate under such seeding density. After 48 h of cultivation, cell seeded on calcined mesoporous TiO₂ film proliferated to a greater extent than non-calcined film and control group. After 6 h of incubation with calcined mesoporous TiO₂ surfaces, cells remained round shape. After 48 h, cell morphology was still intact in structure and most cells homogeneously spreaded and flattened on the surface. The morphology of 7F2 cells on non-calcined and glass surfaces were similar, however, the number of cells adhered to non-calcined surfaces was less than on the glass control, as displayed in Figure 6.7(d), where for the former, residual solvent left within the non-calcined film may exert adverse effect on cell survival, suggesting the solid phase of the non-calcined film together with the templating surfactant are unlikely biocompatible to the cells. Compare with the control group and non-calcined film, 7F2 cells adhered much better and even supported and enhanced cell proliferation on the calcined mesoporous TiO₂ film.

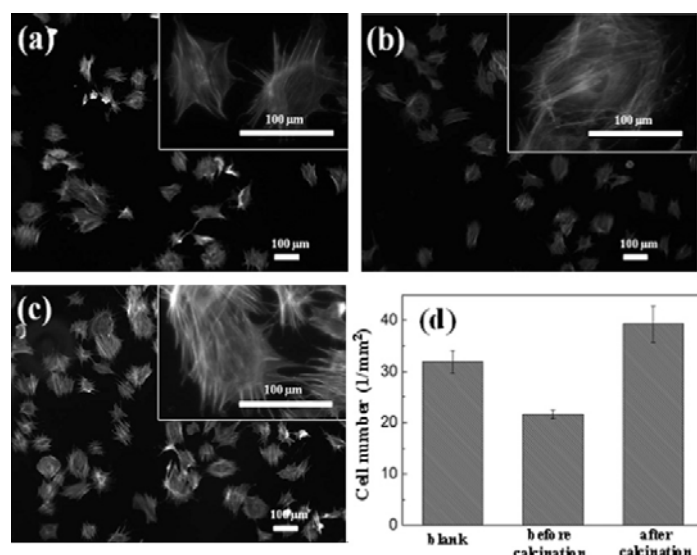


Figure 6.7 Microscopic images (a-c) and cell number calculation (d) of osteoblastic cell incubated for 48 h on the different substrate (glass as control (a), TiO₂ ultrathin film for before (b) or after calcination (c)). For cell counting, the results were averaged and presented as mean \pm SD, and analyzed by Student's t-test (p value <0.05) [249].

6-3.4 Bioactivity of mesoporous TiO₂ ultrathin film

An easy and well-accepted method for estimate of bioactivity of a given surface in vitro is to examine whether the surface is able to induce the formation of apatitic (hydroxyl apatite) layer when soaked in a simulated body fluid (SBF) [245-246]. As an indication of bioactivity, the formation of an apatite layer on the implant surface in vitro was also observed in in vivo experiments and can be translated for the implants to form chemical bonding with living bone. TiO₂ has been reported to be bioactive as hard tissue implants, introduction of porosity turns to be critical in enhancing activity for a TiO₂ coating because the rough and porous surface can enlarge the area for cell attachment and spreading [247]. The formation of a bone-like apatite layer on a bioactive ceramics can be reproduced in an acellular simulated body fluid (SBF) with ion concentrations nearly equal to those of human blood plasma. Figure 6.8(a) shows the SEM micrographs of the calcined mesoporous TiO₂ film soaked in SBF for 10 days. The characteristic apatite globular crystals are clearly visible, as shown in Figure 6.8(b). Therefore, EDS analysis, Figure 6.8(c) ensures that the

surface layer observed in Figure 6.8(a) is mainly composed of calcium phosphate (see Table 6.1). The crystal size of the apatite layer for 10 days incubation was about 1-3 μm and the Ca/P atomic ratio of bone-like apatite was 1.45, which is a typical Ca-deficient apatite, as generally observed in the literature reports. Such as that observed by Milella and coworkers on a titania gel, who suggested the apatite layer formation is virtually a result of that Ti-OH groups along the TiO_2 surface, causing apatite nucleation^[248]. The hydroxyl groups favored reaction with Ca ions from the SBF, followed a subsequent deposition of phosphate groups to form apatite crystallite. Therefore, it suggested that the mesoporous TiO_2 ultrathin film prepared in the work is bioactive, and its worm-like nanostructure along the layer structure multi-functionalized the coating capable of delivering therapeutic drugs for biomedical purpose.



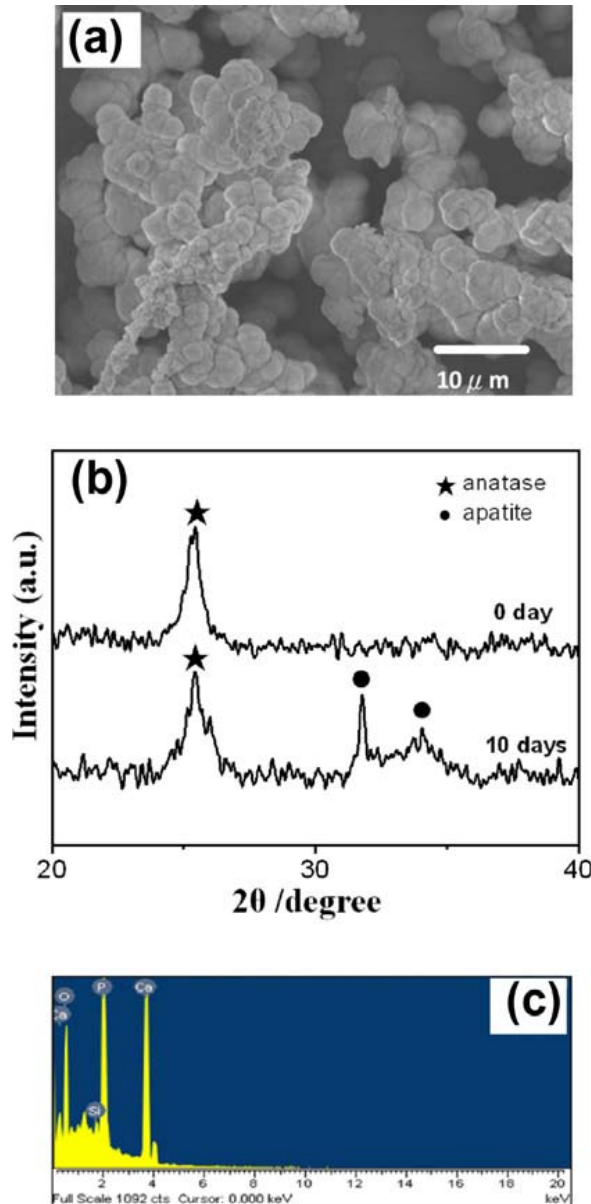


Figure 6. 8 (a) SEM, (b) LA-XRD and, (c) EDS analysis of the calcined mesoporous TiO_2 ultrathin film soaked in SBF for 10 days ^[249].

Table 6. 1 Composition of calcium phosphate on mesoporous TiO_2 thin films soaked in SBF for 10 days.

Ten days after immersion in SBF	Contents of Ca atomic (%)	Contents of P atomic (%)
TiO_2 thin film before calcination	14.7	11.29
TiO_2 thin film after calcination	18.36	12.68

6-4 Conclusion

A facile method was employed to synthesize mesoporous structure of TiO₂ ultrathin films. LA-XRD, SA-XRD, and TEM images showed the formation of worm-like mesoporous structure TiO₂ framework with crystalline phase. The worm-like structure provides a tortuous path for therapeutic molecules to load and diffuse for drug release purpose. FTIR demonstrated that an interaction of the IBU molecule with the mesoporous TiO₂ film, suggesting a good chemical affinity between the IBU and the ultrathin film. Both the chemical affinity and mesoporosity dominate the resulting release profiles for both IBU and VAN molecules. The osteoblast adhesion and hydroxyl apatite deposition confirmed excellent cytocompatibility and bioactive properties of the mesoporous TiO₂ films. Above results suggested that the mesoporous TiO₂ ultrathin film prepared in the work is bioactive, and its worm-like nanostructure, associated with surface chemistry, imparting a capability of simultaneous delivery of drugs for therapeutic purpose upon application.

Chapter 7

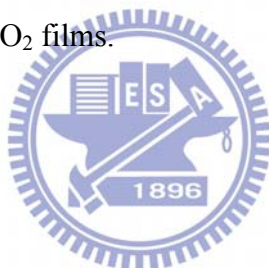
Conclusions

This study has demonstrated that these sol-gel route, microwave-assisted synthesis, hydrothermal urea reaction, and solid-state reaction can be used and designed to prepared the multi-functionalized mesoporous materials (metal oxides: CaO/CaAlO, Ca₁₂Al₁₄O₃₃, Gd₂O₃ and TiO₂), which also have shown potential applications in CO₂ capture and controlled drug delivery. Detailed summaries are presented below.

- (1) New high-temperature CO₂ sorbent, mesoporous Ca-Al metal oxides, were successfully synthesized using γ -Al₂O₃ and CaCl₂ during the hydrothermal urea reaction. The mesoporous M-CaAls with highly dispersed CaO/Ca(OH)₂ nanoparticles inside or outside the mesoporous framework provided a high adsorption capacity, rapid adsorption ability, and stable cyclic life for high-temperature CO₂ capture.
- (2) Novel mesoporous calcium aluminate nanocomposites with crystalline Ca₁₂Al₁₄O₃₃ nanorods and mesoporous structure have been successfully synthesized by using the microwave-hydrothermal process and calcination below 600 °C. The mesostructured calcium aluminates possessed a specific surface area of ~51 m² g⁻¹ and a broad pore size distribution with 4-12 nm. Highly dispersed crystalline C₁₂Al₁₄O₃₃ nanorods growth on the mesoporous CaAlO frameworks were obtained by controlling the Ca/Al molar ratio of 1:1 and microwave hydrothermal time for 1h. In the future, the nanocomposites with pore structure and high thermal stability can be used as a support for CO₂ sorbent or catalyst at high-temperature reaction.
- (3) Innovational highly crystalline mesoporous Gd₂O₃ network with a tubular nanostructure was successfully prepared through the use of structure-directing macromolecules, associated with a sol-gel synthesis. Such a nanostructured tube allowed the therapeutic

substance, e.g. IBU in this case, to be effectively encapsulated and released in a linear fashion. More interestingly, the nanotubes exhibited a weak paramagnetic behavior which enables the encapsulated IBU to elution in a controllable profile upon a magnetic stimulus.

- (4) Mesoporous structure of TiO_2 ultrathin films with worm-like mesoporous structure and crystalline framework provide a tortuous path for therapeutic molecules to load and diffuse for drug release purpose. Both the chemical affinity and mesoporosity dominate the resulting release profiles for both IBU and VAN molecules. The osteoblast adhesion and hydroxyl apatite deposition confirmed excellent cytocompatibility and bioactive properties of the mesoporous TiO_2 films.



References

- [1] K.S.W. Sing, D.H. Everett, R.A.W. Haul, L. Moscou, R.A. Pierotti, J. Rouquerol, T. Siemieniewska, *Pure Appl. Chem.* 57 (1985), 603.
- [2] J.S. Beck, J.C. Vartuli, W.J. Roth, M.E. Leonowicz, C.T. Kresge, K.D. Schmitt, C.T.W. Chu, D.H. Olson, E. W. Sheppard, S.B. Mccullen, J.B. Higgins, J. L. Schlenker, *J. Am. Chem. Soc.* 114 (1992) 10834.
- [3] S. Inagaki, Y. Fukushima, K. Kuroda, *J. Chem. Soc., Chem. Commun.* (1993) 680.
- [4] K. Moller, T. Bein, *Chem. Mater.* 10 (1998) 2950.
- [5] C.M. Yang, H.S. Sheu, K.J. Chao, *Adv. Mater.* 12 (2001) 1403.
- [6] W.J. Roth, C. Vartuli, *Stud. Surf. Sci. Catal.* 157 (2005) 91.
- [7] T.W. Kim, R. Ryoo, K.P. Gierszal, M. Jaroniec, L.A. Solovyov, Y. Sakamoto, O. Terasaki, *J. Mater. Chem.* 15 (2005) 1560.
- [8] W. Zhou, *Solid State Phenom.* 140 (2008) 37.
- [9] A. Sayari, *The chemistry of nanostructured materials*; World Scientific: USA, (2003).
- [10] J. Sun, Z. Shan, T. Maschmeyer, J.A. Moulijn, M.O. Coppens, *Chem. Commun.* (2001) 2670.
- [11] T. Yokoi, T. Tatsumi, *J. Jpn. Petrol. Inst.* 50 (2007) 299.
- [12] T. Yokoi, H. Yoshitake, T. Tatsumi, *Chem. Mater.* 15 (2003) 4536.
- [13] C.J. Brinker, R. Sehgal, S.L. Hietala, R. Deshpande, D.M. Smith, D. Loy, C.S. Ashley, *J. Membr. Sci.* 94 (1994) 85.
- [14] C.S. Cundy, P.A. Cox, *Microporous Mesoporous Mater.* 82 (2005) 1.
- [15] T. Kadono, M. Tajima, T. Shiomura, N. Imawaka, S. Noda, T. Kubota, Y. Okamoto, *Microporous Mesoporous Mater.* 115 (2008) 454.

- [16] L. Huang, S. Kawi, K. Hidajat, S.C. Ng, *Microporous Mesoporous Mater.* 82 (2005) 87.
- [17] T.W Kim, R. Ryoo, M. Kruk, K.P. Gierszal, M. Jaroniec, S. Kamiya, O. Teresaki, *J. Phys. Chem. B* 108 (2004) 11480.
- [18] B.L. Newalkar, S. Komarneni, *Chem. Mater.* 13 (2001) 4573.
- [19] X. Chen, W. Yang, J. Liu, L. Lin, *J. Membr. Sci.* 225 (2005) 201.
- [20] J. Motuzas, S. Heng, P.P.S. Ze Lau, K.L. Yeung, Z.J. Beresnevicius, A. Julbe, *Microporous Mesoporous Mater.* 99 (2007) 197.
- [21] S.E Park, D.S Kim, J.S. Chang, W.Y. Kim, *Catal. Today* 44 (1998) 301.
- [22] G.J.A.A. Soler-Illia, O. Azzaroni, *Chem. Soc. Rev.* 40 (2011) 1107.
- [23] C.J. Brinker, Y. Lu, A. Sellinger, H. Fan, *Adv. Mater.* 11 (1999) 579.
- [24] H. Yang, N. Coombs, G.A. Ozin, *Nature* 386 (1997) 692.
- [25] G.S. Attard, J.C. Glyde, C.G. Goltner, *Nature* 378 (2000) 35.
- [26] S. Che, Z. Liu, T. Ohsuna, K. Sakamoto, O. Terasaki, T. Tatsumi, *Nature* 429 (2004) 281.
- [27] F. Schuth, *Stud. In Surf. Science and Catal.* 135 (2001) 101.
- [28] C. Sanchez, G.J.D.A. Soler-Illia, F. Ribot, D. Grosso, *C.R. Chim.* 6 (2003) 1131.
- [29] A. Cabot, J. Arbiol, A. Cornet, J. R. Morante, F. Chen, M. Liu, *Thin Solid Films* 436 (2003) 64.
- [30] G. Wirnsberger, B. J. Scott, G.D. Stucky, *Chem. Commun.* (2001) 119.
- [31] L. Cot, A. Ayral, J. Durand, C. Guizard, N. Homanian, A. Julbe, A. Larbot, *Solid State Sci.* 2 (2000) 313.
- [32] C. Renault, V. Balland, E. Martinez-Ferrero, L. Nicole, C. Sanchez, B. Limoges, *Chem. Commun.* (2009) 7494
- [33] Lionel Nicole, Clément Sanchez, Benoît Limoges, *Chem. Commun.* (2009) 7494.
- [34] V.V. Guliyants, M.A. Carreon, Y.S. Lin, *J. Membr. Sci.* 235 (2004) 53.

- [35] O. de la Iglesia, M. Pedernera, R. Mallada, Z. Lin, J. Rocha, J. Coronas, J. Santamaría, *J. Membr. Sci.* 280 (2006) 867.
- [36] D. Grosso, A.R. Balkenende, P.A. Albouy, F. Babonneau, *Stud. Surf. Sci. Catal.* 129 (2000) 673.
- [37] J.M. Gomez-Vega, M. Iyoshi, K.Y. Kim, A. Hozumi, H. Sugimura, O. Takai, *Thin Solid Films* 615 (2001) 398.
- [38] H. Miyata, T. Noma, M. Watanabe, K. Kuroda, *Chem. Mater.* 14 (2002) 766.
- [39] W. Huang, B. Liu, F. Sun, Z. Zhang, X. Bao, *Microporous Mesoporous Mater.* 94 (2006) 254.
- [40] Y. Liang, M. Hanzlik, R. Anwender, *Chem. Commun.* (2005) 525.
- [41] M.B Yue, Y. Chun, Y. Cao, X. Dong, J.H. Zhu, *Adv. Funct. Mater.* 16 (2006) 1717.
- [42] R.S. Franchi, P.J.E. Harlick, A. Sayari, *Ind. Eng. Chem. Res.* 44 (2005) 8007.
- [43] S.K. Wirawan, D. Creaser, *Microporous Mesoporous Mater.* 91 (2006) 196.
- [44] P.J.E. Harlick, A. Sayari, *Stud. Surf. Sci. Catal.* 158 (2005) 987.
- [45] G. Xomeritakis, C.Y Tsai, C.J. Brinker, *Sep. Purif. Technol.* 42 (2005) 249.
- [46] S. Huh, J.W. Wiench, J.C Yoo, M. Pruski, VS.Y. Lin, *Chem. Mater.* 15 (2003) 4247.
- [47] N.Y. Yu, J.L. Zheng, Q.L. Tang, D. Wu, Y.H. Sun, W. Hu, W.Y. Liu, F. Deng, W. Hu, *Stud. Surf. Sci. Catal.* 156 (2005) 213.
- [48] G.E. Fryxell, G. Cao, *Imperial College Press* (2006) 179.
- [49] S. Che, A. E. Garcia-Bennett, T. Yokoi, K. Sakamoto, H. Kunieda, O. Terasaki, T. Tatsumi, *Nat. Mater.* 2 (2003) 801.
- [50] M.H Lim, A. Stein, *Chem. Mater.* 11 (1999) 3285.
- [51] IPCC, *Climate Change 2007: The Physical Science Basis*. Cambridge Univ. Press, Cambridge UK and New York, USA, (2007).
- [52] The NOAA annual greenhouse gas index (AGGI) is available at <http://www.esrl.noaa.gov/gmd/aggi/>.

- [53] A.A. Lacis, G.A. Schmidt, D. Rind, R.A. Ruedy, *Science* 330 (2010) 356.
- [54] CO₂ and temperature over the 20th century is available at <http://www.skepticalscience.com/co2-temperature-correlation.htm>
- [55] J.D. Figueroa, T. Fout, S. Plasynski, H. McIlvried, R.D. Srivastava, *Int. J. Greenh. Gas Con.* 2 (2008) 9.
- [56] Energy Information Administration (EIA), 2006a. Annual Energy Outlook 2006. <http://www.eia.doe.gov/oiaf/aeo/>.
- [57] Energy Information Administration (EIA), 2006b. International Energy Outlook 2006. <http://www.eia.doe.gov/oiaf/ieo/index.html>.
- [58] M. Bracht, *Energy Convers. Manage.* 38 (1997) 159.
- [59] J.W. Dijkstra, D. Jansen, G.P. Leendertse, P.P.A.C. Pex, *Hydrogen membrane reactor as key technology for sustainable use of fossil fuels*, in *Proceedings of the 1st European Hydrogen Energy Conference*, Grenoble, (2003).
- [60] J.R. Hufton, R.J. Allam,; R. Chiang, P. Middleton, E.L. Weist, V. White, *Development of a process for CO₂ capture from gas turbines using a sorption enhanced water gas shift reactor system*, in *Proceedings of the 7th International Conference on Greenhouse Gas Technologies*, Vancouver, (2004).
- [61] J.R. Hufton, S. Mayorga, S. Sircar, *AIChE J.* 45 (1999) 248.
- [62] D.P. Harrison, Z. Peng, *Int. J. Chem. React. Eng.* 1 (2003), 1.
- [63] C.S. Martavaltzi, A.A. Lemonidou, *Microporous Mesoporous Mater.* 110 (2008) 119.
- [64] Y. Ding, E. Alpay, *Chem. Eng. Science*, 55 (2000) 3929.
- [65] Z. Yong, V. Mata, A.E. Rodrigues, *Ind. Eng. Chem. Res.* 40 (2001) 204.
- [66] S.G. Mayorga, *Carbon dioxide adsorbents containing magnesium oxide suitable for use at high temperatures*. Air Products and Chemicals Inc. Allentown (PA). US Patent no. 6280503 B1, (2001).
- [67] M. Kato, S. Yoshikawa, K. Nakagawa, *J. Mater. Sci. Lett.* 21 (2002) 485.

- [68] K. Nakagawa, M. Kato, S. Yoshikawa, K. Essaki, *A novel CO₂ absorbent using lithiumcontaining oxides, in Proceedings of the 2nd Annual Conference on Carbon Sequestration, Alexandria VA, (2003).*
- [69] Y. Sakamoto, K. Nagata, K. Yogo, K. Yamada. *Microporous Mesoporous Mater.* 101 (2007) 303.
- [70] P. Kumar, S. Kim, J. Ida, V.V. Guliants. *Ind. Eng. Chem. Res.* 47 (2008) 201. M.T. Ho, G.A. Allinson, D.E. Wiley, *Ind. Eng. Chem. Res.* 47 (2008) 1562.
- [71] S.W. Park, D.S. Suh, K.S Hwang, H. Kumazawa, *Korean J. Chem. Eng.* 14 (1997) 285.
- [72] F. Zheng, D.N. Tran, B.J. Busche, G.E. Fryxell, R.S. Addleman, T.S Zemanian, C.L. Aardahl, *Ind. Eng. Chem. Res.* 44 (2005) 3099.
- [73] M.L. Gray, Y. Soong, K.J. Champagne, H.W. Pennline, J. Baltrus, R.W. Stevens Jr, R. Khatri, S.S.C. Chuang, T. Filburn, *Fuel Proc. Technol.* 86 (2005) 1449.
- [74] R. Bounaceur, N. Lape, D. Roizard, C. Vallieres, E. Favre, *Energy* 31 (2006) 2556.
- [75] G.P. Knowles, J.V. Graham, S.W. Delaney, A.L. Chaffee, *Fuel Process. Technol.* 86 (2005) 1435.
- [76] S. Kim, J. Ida, V.V. Guliants, Y.S. Lin, *J. Phys. Chem. B* 109 (2005) 6287.
- [77] A. Vinu, M. Miyahara, K. Ariga, *J. Nanosci. Nanotechno.* 6 (2006) 1510.
- [78] K. Ariga, A. Vinu, J.P. Hill, T. Mori, *Coord. Chem. Rev.* 251 (2007) 2562.
- [79] I.I. Slowing, J.L. Vivero-Escoto, C.W. Wu, V.S.Y. Lin, *Adv. Drug Deliver. Rev.* 60 (2008) 1278.
- [80] K. Ariga, *Chem. Rec.* 3 (2004) 297.
- [81] W. Otani, K. Kinbara, Q. Zhang, K. Ariga, T. Aida, *Chem. Eur. J.* 13 (2007) 1731.
- [82] A. Vinu, M. Miyahara, K. Ariga, *J. Phys. Chem. B* 109 (2005) 6436.
- [83] C.Y. Lai, B.G. Trewyn, D.M. Jeftinija, K. Jeftinija, S. Xu, S. Jeftinija, V.S.Y. Lin, *J. Am. Chem. Soc.* 125 (2003) 4451.

- [84] J. Wu, Y.J. Zhu, S.W. Cao, F. Chen, *Adv. Mater.* 22 (2010) 749.
- [85] J.H. Chang, C.H. Shim, B.J. Kim, Y. Shin, G.J. Exarhos, K.J. Kim, *Adv. Mater.* 17 (2005) 634.
- [86] Q. Fu, G.V.R. Rao, L.K. Ista, Y. Wu, B.P. Andrzejewski, L.A. Sklar, T.L. Ward, G.P. Lopez, *Adv. Mater.* 15 (2003) 1262.
- [87] Z.Y. Zhou, S.M. Zhu, D. Zhang, *J. Mater. Chem.* 17 (2007) 2428.
- [88] K.A. Fisher, D.H. Katherine, T.M. Joan, *Chem. Eur. J.* 9 (2003) 5873.
- [89] Y. Zhao, L.N. Lin, Y. Lu, S.F. Chen, L. Dong, S.H. Yu, *Adv. Mater.* 22 (2010) 5255.
- [90] K.C.F. Leung, T.D. Nguyen, J.F. Stoddart, J.I. Zink, *Chem. Mater.* 18 (2006) 5919.
- [91] W.J. Xu, Q. Gao, Y. Xu, D. Wu, Y. Sun, *Mater. Res. Bull.* 44 (2009) 606.
- [92] C. Park, K. Oh, S.C. Lee, C. Kim, *Angew. Chem. Int. Ed.* 46 (2007) 1455.
- [93] H.J. Kim, H. Matsuda, H.S. Zhou, I. Honma, *Adv. Mater.* 18 (2006) 3083.
- [94] T.D. Nguyen, Y. Liu, S. Saha, K.C.F. Leung, J.F. Stoddart, J.I. Zink, *J. Am. Chem. Soc.* 129 (2007) 626.
- [95] R. Hernandez, H.R. Tseng, J.W. Wong, J.F. Stoddart, J.I. Zink, *J. Am. Chem. Soc.* 126 (2004) 3370.
- [96] D.P. Ferris, Y.L. Zhao, N.M. Khashab, H.A. Khatib, J.F. Stoddart, J.I. Zink, *J. Am. Chem. Soc.* 131 (2009) 1686.
- [97] N.K. Mal, M. Fujiwara, Y. Tanaka, *Nature* 421 (2003) 350.
- [98] N.K. Mal, M. Fujiwara, Y. Tanaka, T. Taguchi, M. Matsukata, *Chem. Mater.* 15 (2003) 3385.
- [99] J. Lu, E. Choi, F. Tamanoi, J.I. Zink, *Small* 4 (2008) 421.
- [100] S. Giri, B.G. Trewyn, M.P. Strellmaker, V.S.Y. Lin, *Angew. Chem. Int. Ed.* 44 (2005) 5038.
- [101] E. Ruiz-Hernandez, A. Lopez-Noriega, D. Arcos, I. Izquierdo-Barba, O. Terasaki, M. Vallet-Regi', *Chem. Mater.* 19 (2007) 3455.

- [102] R. Xing, H. Lin, P. Jiang, F. Qu, *Colloids Surf., A* 403 (2012) 7.
- [103] L.L. Yu, H. Bi, *J. Appl. Phys.* 111 (2012) 07B514.
- [104] P. Yang, Z. Quan, Z. Hou, C. Li, X. Kang, Z. Cheng, J. Lin, *Biomaterials* 30 (2009) 4786.
- [105] S. Zhu, Z. Zhou, D. Zhang, *ChemPhysChem* 8 (2007) 2478.
- [106] S. Guo, D. Li, L. Zhang, J. Li, E. Wang, *Biomaterials* 30 (2009) 1881.
- [107] Y.P. Guo, L.H. Guo, Y.b. Yao, C.Q. Ning, Y.J. Guob, *Chem. Commun.* 47 (2011) 12215.
- [108] M. Zrínyi, *Colloid. Polym. Sci.* 278 (2000) 98
- [109] T.Y. Liu, Ph. D. Thesis, *Study on intelligent magnetic hydrogel and nanosphere for drug controlled release*, Department of Materials Science and Engineering, National Chiao Tung University, July (2008)
- [110] J.M. Gomez-Vega, A. Hozumi, H. Sugimura, O. Takai, *Adv. Mater.* 13 (2001) 822.
- [111] M. Vallet-Regi, I. Izquierdo-Barba, A. Ramila, J. Perez-Pariente, F. Babonneau, J.M. Gonzalez-Calbet, *Solid State Sci.* 7 (2005) 233.
- [112] J. Andersson, S. Areva, B. Spliethoff, M. Linden, *Biomaterials* 26 (2005) 6827.
- [113] B. Onida, V. Cauda, S. Fiorilli, E. Verne, C.V. Brovarone, D. Viterbo, G. Croce, M. Milanesio, G. Croce, *Stud. Sur. Sci. Catal.* 158 (2005) 2027.
- [114] M. Vallet-Regí, M. Colilla, I. Izquierdo-Barba, *J. Biomed. Nanotechnol.* 4 (2008) 1.
- [115] M. Colilla, M. Manzano, I. Izquierdo-Barba, M. Vallet-Regí, C. Boissière, C. Sanchez, *Chem. Mater.* 22 (2010) 1821.
- [116] J.M. Gomez-Vega, M. Iyoshia, K.Y. Kim, A. Hozumi, H. Sugimura, O. Takaia, *Thin Solid Films* 398-399 (2001) 615.
- [117] L.M. Perez, P. Lalueza, M. Monzon, J.A. Puertolas, M. Arruebo, J. Santamaría, *Int. J. Pharm.* 409 (2011) 1.

- [118] N. Ehlert, M. Badar, A. Christel, S.J Lohmeier, T. Luessenhop, M. Stieve, T. Lenarz, P.P. Mueller, P. Behrens, *J. Mater. Chem.* 21 (2011) 752.
- [119] X. Li, J. Shi, Y. Zhu, W. Shen, H. Li, J. Liang, J. Gao, *J. Biomed. Mater. Res. B.* 83B (2007) 431.
- [120] E. Milella, F. Cosentino, A. Licciulli, C. Massaro, *Biomaterials* 22 (2001) 1425.
- [121] Y.C. Yang, E.W. Chang, B.H. Hwang, S.Y. Lee, *Biomaterials* 21 (2000) 1327.
- [122] Q.Y. Zhang, Y. Leng, R.L. Xin, *Biomaterials* 26 (2005) 2857.
- [123] A. López-Noriega, D. Acros, I. Izquierdo-Barba, Y. Sakamoto, O. Terasaki, M. Vallet-Regí, *Chem. Mater.* 18 (2006) 3137.
- [124] H. Tang, Y. Guo, D. Jia, Y. Zhou, *Microporous Mesoporous Mater.* 131 (2010) 366.
- [125] Y.P. Guo, H.X. Tang, Y. Zhou, D.C. Ji, C.Q. Ning, Y.J. Guo, *Appl. Surf. Sci.* 256 (2010) 4945.
- [126] W. Xia, K. Grandfield, A. Hoess, A. Ballo, Y. Cai, H. Engqvist, *J. Biomed. Mater. Res. B.* 100B (2012) 82
- [127] P. Jiang, H. Lin, R. Xing, J. Jiang, F. Qu, *J. Sol-Gel Sci. Technol.* 61 (2012) 421.
- [128] C. Azar, H. Rodhe, *Science* 276 (1997) 1818.
- [129] H. Herzog, E. Drake, E. Adams, Report to U.S., DOE/DE-AF22-96PC01257, 1997.
- [130] J.A. Ruether, Report to U.S., DOE/FETC-98/1058, 1999.
- [131] D.P. Harrison, *Ind. Eng. Chem. Res.* 47 (2008) 6486.
- [132] A. Auroux, A. Gervasini, *J. Phys. Chem.* 94 (1990) 6371.
- [133] C.S. Martavaltzi, A.A. Lemionidou, *Microporous Mesoporous Mater.* 110 (2008) 119.
- [134] Q. Wang, J. Luo, Z. Zhong, A. Borgna, *Energy Environ. Sci.* 4 (2011) 42.
- [135] M.K. Ram Reddy, Z.P. Xu, G.Q. (Max) Lu, J.C. Diniz da Costa, *Ind. Eng. Chem. Res.* 45 (2006) 7504.
- [136] N.D. Hutson, B.C. Attwood, *Adsorption* 14 (2008) 781.
- [137] H. Pfeiffer, P. Bosch, *Chem. Mater.* 17 (2005) 1704.

- [138] E.O. Fernandez, H.K. Rusten, H.A. Jakobsen, M. Ronning, A. Holmen, D. Chen, *Catal. Today* 106 (2005) 41.
- [139] J.I. Ida, Y.S. Lin, *Environ. Sci. Technol.* 37 (2003) 1999.
- [140] M. Lakraimi, A. Legrouri, A. Barroug, A. De Roy, J.P. Besse, *J. Mater. Chem.* 10 (2000) 1007.
- [141] T. Yamamoto, T. Kodama, N. Hasegawa, M. Tsuji, Y. Tamaura, *Energy Convers. Manage.* 36 (1995) 637.
- [142] Z.S. Li, N.S. Cai, Y.Y. Huang, H.J. Han, *Energy Fuels* 19 (2005) 1447.
- [143] S.F. Wu, T.H. Beum, J.I. Yang, J.N. Kim, *Ind. Eng. Chem. Res.* 46 (2007) 7896.
- [144] C.S. Martavaltzi, A.A. Lemionidou, *Ind. Eng. Chem.* 47 (2008) 9537.
- [145] X.P. Wang, J.J. Yu, J. Cheng, Z.P. Hao, Z.P. Xu, *Environ. Sci. Technol.* 42 (2008) 614.
- [146] Q. Wang, H.H. Tay, D.J.W. Ng, L. Chen, Y. Liu, J. Chang, Z. Zhong, J. Luo, A. Borgna, *ChemSusChem* 3 (2010) 965.
- [147] Q. Wang, Z. Wu, H.H. Tay, L. Chen, Y. Liu, J. Chang, Z. Zhong, J. Luo, and A. Borgna, *Catal. Today* 164 (2011) 198.
- [148] C.T. Kresge, M.E. Leonowicz, W.J. Roth, J.C. Vartuli, J.S. Beck, *Nature* 359 (1992) 710.
- [149] J. Tantirungrotechai, P. Chotmongkolsap, M. Pohmakotr, *Microporous Mesoporous Mater.* 128 (2010) 41.
- [150] J. Chandradass, M. Balasubramanian, *J. Mater. Sci.* 41 (2006) 6026.
- [151] J. Zou, L. Pu, X. Bao, D. Feng, *Appl. Phys. Lett.* 80 (2002) 1079.
- [152] C. Chen, W.S. Ahn, *Chem. Eng. J.* 166 (2011) 646.
- [153] Q. Yuan, A.X. Yin, C. Luo, L.D. Sun, Y.W. Zhang, W.T. Duan, H.C. Liu, C.H. Yan, *J. Am. Chem. Soc.* 130 (2008) 3465.
- [154] L. He, H. Berntsen, D. Chen, *J. Phys. Chem. A* 114 (2010) 3834.
- [155] M. Kruk, M. Jaroniec, *Chem. Mater.* 13 (2001) 3169.

- [156] Z.Y. Yuan, B.L. Su, *Chem. Phys. Lett.* 381 (2003) 710.
- [157] T.Z. Ren, Z.Y. Yuan, B.L. Su, *Chem. Phys. Lett.* 374 (2003) 170.
- [158] S.F. Wu, M.Z. Jiang, *Ind. Eng. Chem. Res.* 49 (2010) 12269.
- [159] J. Cheng, X. Zhang, Z. Luo, F. Liu, Y. Ye, W. Yin, W. Liu, Y. Han, *Mater. Chem. Phys.* 95 (2006) 5.
- [160] Y. Arai, M. Ogawa, *Appl. Clay Sci.* 42 (2009) 601.
- [161] Q. Huo, D.I. Margolese, G.D. Stucky, *Chem. Mater.* 8 (1996) 1147.
- [162] P. Yang, D. Zhao, D.I. Margolese, B.F. Chmelka, G.D. Stucky, *Nature* 396 (1998) 152.
- [163] R.W. Hicks, T.J. Pinnavaia, *Chem. Mater.* 15 (2003) 78.
- [164] Y. Mathieu, L. Vidal, V. Valtchev, B. Lebeau, *New J. Chem.* 33 (2009) 2255.
- [165] X.Y. Chen, H.S. Huh, S.W. Lee, *Nanotechnology* 18 (2007) 285608.
- [166] Z.P. Xu, G.Q. (Max) Lu, *Chem. Mater.* 17 (2005) 1055.
- [167] P. Alphonse, M. Courty, *Thermochim. Acta* 425 (2005) 75.
- [168] D. Chen, E. Bjorgum, K.O. Christensen, A. Holmen, R. Lodeng, *Adv. Catal.* 51 (2007) 351.
- [169] H. Lu, E.P. Reddy, P.G. Smirniotis, *Ind. Eng. Chem. Res.* 45 (2006) 3944.
- [170] J. Wang, E.J. Anthony, *Ind. Eng. Chem. Res.* 44 (2005) 627.
- [171] M. León, E. Díaz, S. Bennici, A. Vega, S. Ordóñez, A. Auroux, *Ind. Eng. Chem. Res.* 49 (2010) 3663.
- [172] Y.C. Chen, Master thesis, *Synthesis, characterization and CO₂ adsorption of mesoporous composite materials*, Department of Materials Science and Engineering, National Chiao Tung University, July (2010)
- [173] F.T. Wallenberger, N.E. Weston, S.D. Brow, *Melt processed calcium aluminate fibers: structural optical properties*; Bellingham, (1991).
- [174] M. Lacerada, J.T.S. Irvine, E.E. Lachowski, E.P. Glasser, A.R. West, *Br. Ceram. Trans. J.* 87 (1988) 191.

- [175] S.J. Kalita¹, S. Bose¹, H.L. Hosick, A. Bandyopadhyay, *J. Mater. Res.* 17 (2002) 3042.
- [176] A. Faris, H. Engqvist, J. Loof, M. Ottosson, L. Hermansson, *Key Eng Mater.* 309- 311 (2006) 833.
- [177] A.A. Lemonidou, M.A. Goula, I.A. Vasalos, *Catal. Today* 46 (1998) 175.
- [178] K. Hayashi, S. Matsuishi, T. Kamiya, M. Hirano, H. Hosono, *Nature* 419 (2002) 462.
- [179] P.V. Sushko, A.L. Shluger, K. Hayashi, M. Hirano, H. Hosono, *Phys. Rev. B* 73 (2006) 014101.
- [180] K. Fujji, W. Kondo, H. Ueno, *J. Am. Ceram. Soc.* 69 (1986) 361.
- [181] M. Uberoi, S.H. Risbud, *J. Am. Ceram. Soc.* 73 (1990) 1768.
- [182] M.A. Gulgun, O.O. Popoola, W.M. Kriven, *J. Am. Ceram. Soc.* 77 (1994) 531.
- [183] D.M. Roy, R.R. Neurgaonkar, T.P. O'Holleran, R. Roy, *Am. Ceram. Soc. Bull.* 56 (1977) 1023.
- [184] M.F. Zawrah, N.M. Khalil, *Ceram. Int.* 33 (2007) 1419.
- [185] E.D. Neas, M.J. Collins. *Microwave heating, theoretical concepts and equipment design, in Introduction to Microwave Sample Preparation, Theory and Practice*, American Chemical Society; Washington, (1993).
- [186] D.R. Baghurst, D.M.P. Mingos, *J. Chem. Soc., Chem. Commun.* (1992) 674.
- [187] B.L. Newalkar, S. Komarneni, *Chem. Mater.* 13 (2001) 4579.
- [188] Z. Zhaorong, J. Thomas, *Angew. Chem.* 120 (2008) 7611.
- [189] S.F. Wu, Q.H. Li, J.N. Kim, K.B. Yi, *Thermochim. Acta*, 388 (2002) 105.
- [190] J.M. Rivas Mercury, A.H. De Aza, X. Turrillas, P. Pena, *J. Solid State Chem.* 177 (2004) 866.
- [191] P. Gruene, A.G. Belova, T.M. Yegulalp, R.J. Farrauto, M.J. Castald, *Ind. Eng. Chem. Res.* 50 (2011) 4042.
- [192] P. Colomban, *J. Mater. Sci. Lett.* 7 (1988) 1324.

- [193] G.K. Priya, P. Padmaja, K.G.K. Warriar, A.D. Damodaran, G. Aruldas, *J. Mater. Sci. Lett.* 16 (1997) 1584.
- [194] P. Tarte, *Spectrochim. Acta A*, 23 (1967) 2127.
- [195] G. Arukdhas, *Molecular Structure and Spectroscopy*, (2008).
- [196] P. Yang, D. Zhao, D.I. Margolese, B.F. Chmelka, G.D. Stucky, *Nature* 396 (1998) 152.
- [197] T.J. Lee, Master thesis, *Synthesis, Characterization and CO₂ Capture of Porous Ca-Al-O Composite Sorbents*, Department of Materials Science and Engineering, National Chiao Tung University, August (2011)
- [198] P. Couvreur, C. Vauthier, *Pharm. Res.* 23 (2006) 1417.
- [199] C.R. Martin, P. Kohli, *Nat. Rev. Drug Discov.* 2 (2003) 29.
- [200] B. Peter, D.P. Pioletti, S. Laib, B. Bujoli, P. Pilet, P. Janvier, J. Guicheux, P.Y. Zambelli, J.M. Bouler, O. Gauthier, *Bone* 36 (2005) 52.
- [201] S.J. Son, J. Reichel, B. He, M. Schuchman, S.B. Lee, *J. Am. Chem. Soc.* 127 (2005) 7316.
- [202] T.J. Yoon, J.S. Kim, B.G. Kim, K.M. Yu, M.H. Cho, J.K. Lee, *Angew. Chem. Int. Ed.* 44 (2005) 1068.
- [203] S.H. Hu, D.M. Liu, W.L. Tung, C.F. Liao, S.Y. Chen, *Adv. Funct. Mater.* 18 (2008) 2946.
- [204] Y.F. Shi, Y. Wan, R.Y. Zhang, D.Y. Zhao, *Adv. Funct. Mater.* 18 (2008) 2436.
- [205] M. Tiemann, *Chem. Mater.* 20 (2008) 961.
- [206] M. Muthukumar, C.K. Ober, E.L. Thomas, *Science* 277 (1997) 1225.
- [207] Q. Huo, D.I. Margolese, U. Ciesla, P. Feng, T.E. Gier, P. Sieger, R. Leon, P.M. Petroff, F. Schüth, G.D. Stucky, *Nature* 368 (1994) 317.
- [208] A. Van Blaaderen, R. Ruel, P. Wiltzius, *Nature* 385 (1997) 321.
- [209] M.R. Ghadiri, J.R. Cranja, L.K. Buehler, *Nature* 369 (1997) 301.

- [210] D. Zhao, Q. Feng, N. Melosh, G.H. Fredrickson, B.F. Chmelka, G.D. Stucky, *Science* 279 (1998) 548.
- [211] H. Gao, X. Yang, T. Xiao, W. Zhang, L. Lou, J. Mugnier, *Appl. Surf. Sci.* 230 (2004) 215.
- [212] M.A. Fortin, R.M. Petoral, F. Söderlind, A. Klasson, M. Engström, T. Veres, P.O. Käll, K. Uvdal, *Nanotechnology* 18 (2007) 395501.
- [213] Y.S. Lin, S.H. Wu, Y. Hung, Y.H. Chou, C. Chang, M.L. Lin, C.P. Tsai, C.Y. Mou, *Chem. Mater.* 18 (2006) 5170.
- [214] R. Mohr, K. Kratz, T. Weigel, M. Lucka-Gabor, M. Moneke, A. Lendlein, *Proc. Natl Acad. Sci. USA* 103 (2006) 3540.
- [215] P. Yang, T. Deng, D. Zhao, P. Feng, D. Pine, B.F. Chmelka, G.M. Whitesides, G.D. Stucky, *Science* 282 (1998) 2244.
- [216] Y. Zhao, X. Chen, C. Yang, G. Zhang, *J. Phys. Chem. B* 111 (2007) 13937.
- [217] H. Chen, J. Zhang, X. Wang, S. Gao, M. Zhang, Y. Ma, Q. Dai, D. Li, S. Kan, G. Zou, *J. Colloid Interface Sci.* 97 (2006) 130.
- [218] G. Socrates, *Infrared characteristic group frequencies; tables and charts*: New York; Wiley, (1994).
- [219] B. Sitharaman, L.J. Wilson, *J. Biomed. Nanotechnol.* 3 (2007) 342.
- [220] A.A. Campbell, *Mater. Today* 11 (2003) 26.
- [221] P.I. Brånemark, *J. Prosthet. Dent.* 50 (1983) 399.
- [222] B. Yang, M. Uchida, H.M. Kim, X. Zhang, T. Kokubo, *Biomaterials* 25 (2004) 1003.
- [223] T. Peltola, M. Jokinen, H. Rahiala, M. Päätsi, J. Heikkilä, I. Kangasniemi, A. Yli-Urpo, *J. Biomed. Mater. Res.* 51 (2000) 200.
- [224] S. Areva, V. Ääritalo, S. Tuusa, M. Jokinen, M. Lindén, T. Peltola, *J. Mater. Sci. Mater. Med.* 18 (2007) 1633.

- [225] C.M. Vallecillo, O.M.N. Romero, G.M.V. Olmedo, B.C. Reyes, R.C. Zorrilla, J. Oral. *Implantol.* 33 (2007) 59.
- [226] U. Brohede, S. Zhao, F. Lindberg, A. Mihranyan, J. Forsgren, M. Strømme, E. Håkan, *Appl. Surf. Sci.* 255 (2009) 7723.
- [227] Z. Zhang, J. Sun, H. Hu, Q. Wang, X. Liu, *J. Biomed. Mater. Res.* 97 (2011) 224.
- [228] F. Likibi, B. Jiang, *J. Mater. Res.* 23 (2008) 3222.
- [229] M. Ueda, H. Sai, M. Ikeda, M. Ogawa, *Mater. Sci. Forum* 654–656 (2010) 2257.
- [230] D. Triggler, *J. Med. Princ. Pract.* 16 (2007) 1.
- [231] C.A. Grimes, *J. Mater. Chem.* 17 (2007) 1451.
- [232] K.A. Gross, W. Walsh, E. Swarts, *J. Therm. Spray Technol.* 13 (2004) 190.
- [233] B. León, J.A. Jansen, *Thin Calcium Phosphate Coatings for Medical Implants*; Springer Verlag: New York, (2009).
- [234] P. Yang, D. Zhao, B.F. Chmelka, G.D. Stucky, *Chem. Mater.* 10 (1998) 2033.
- [235] M. Suh, H.J. Lee, J.Y. Park, U.H. Lee, Y.U. Kwon, D.J. Kim, *ChemPhysChem* 9 (2008) 1402.
- [236] H. Hata, S. Saeki, T. Kimura, Y. Sugahara, K. Kuroda, *Chem. Mater.* 11 (1999) 1110.
- [237] J.C. Yu, L.Z. Zhang, J.G. Yu, *New J. Chem.* 26 (2002) 416.
- [238] E. Crepaldi, G.J. Soler-Illia, D.A.A. Grosso, D. Albouy, P.A. Amenitsch, C. Sanchez, *Stud. Surf. Sci. Catal.* 141 (2002) 235.
- [239] J.C. Yu, L. Zhang, Z. Zheng, J. Zhao, *Chem. Mater.* 15 (2003) 2280.
- [240] H. Li, W. Shen, J. Shi, L. Xiong, J. Liang, M. Ruan, *J. Mater. Res.* 21 (2006) 380.
- [241] Z. Ding, G.Q. Lu, P.F. Greenfield, *J. Phys. Chem. B* 104 (2000) 4815.
- [242] B. Tian, F. Chen, J. Zhang, M. Anpo, *J. Colloid Interf. Sci.* 303 (2006) 142.
- [243] T. Lopez, J. Navarrete, R. Conde, J.A. Ascencio, J. Manjarrez, R.D. Gonzalez, *J. Biomed. Mater. Res.* 78 (2006) 441.
- [244] N.A. Peppas, *Pharm. Acta Helv.* 60 (1985) 110.

- [245] M. Uchida, H.M. Kim, T. Kokubo, S. Fujibayashi, T. Nakamura, *J. Biomed. Mater. Res.* 64 (2003) 164.
- [246] K. Prashantha, B.J. Rashmi, T.V. Venkatesha, J.H. Lee, *Spectrochim. Acta A* 65 (2006) 340.
- [247] E. Gultepe, D. Nagesha, S. Sridhar, M. Amiji, *Adv. Drug Deliv. Rev.* 62 (2010) 305.
- [248] C. Massaro, M.A. Baker, F. Cosentino, P.A. Ramires, S. Klose, E. Milella, *J. Biomed. Mater. Res.* 58 (2001) 651.
- [249] C.S. Chao, Master thesis, *Synthesis and characterization of mesoporous TiO₂ thin film and its use for controlled drug delivery*, Department of Materials Science and Engineering, National Chiao Tung University, July (2009)



Appendix-1

Structure Identification and CO₂ Adsorption Behavior of Metal Oxides by Hydrothermal Coprecipitation Route

A.1-1 Introduction

In recent years, high-temperature CO₂ capture of adsorbent materials has become increasingly important in the applications of energy and environment, such as controlling CO₂ emissions from the combustion of fossil fuels, such as coal or natural gas ^[1]. Although many materials have been developed as adsorbents for high-temperature CO₂ capture, the investigations on CO₂ adsorption suggest that layered double hydroxides (LDHs) display excellent attributes of a good adsorbent, such as high adsorption selectivity and capacity, rapid adsorption/desorption kinetics at operating conditions, and good mechanical strength of adsorbent particles after cyclic exposure to high-pressure streams ^[2-5].

LDHs, also known as hydrotalcites (HTlc), are a kind of anionic clay of inorganic layered material. The general formula of the LDHs is $[M^{2+}_{1-x}M^{3+}_x(OH)_2]^{x+} \cdot [A^{m-}_{x/m} \cdot nH_2O]^{x-}$, where M^{2+} is a divalent cation such as Mg^{2+} , Ni^{2+} , Zn^{2+} , Cu^{2+} , Mn^{2+} and etc., M^{3+} is a trivalent cation such as Al^{3+} , Fe^{3+} , Cr^{3+} and etc., and A^{m-} is an interlayer anion such as CO_3^{2-} , SO_4^{2-} , NO_3^- , Cl^- , OH^- and etc. So far, although many different processes have been developed to synthesize LDHs, the coprecipitation method has been most widely used in which a salt solution of metal (IIA) and metal (IIIA) is added quickly to an alkaline salt solution. Among the II-III LDH materials, Mg-Al-CO₃ LDH (see Appendix-2) is widely studied for CO₂ adsorption because Mg oxide or Mg hydroxide provided a basic site which can react with CO₂ gas to form MgCO₃. A model has been proposed to study the thermal evolution and CO₂ adsorption capacity of Mg-Al-CO₃ LDH structures ^[6-7]. However, structure evolution and CO₂ adsorption behavior of metal oxides (MgO/Al₂O₃) by

hydrothermal coprecipitation from various IIA-based LDH compositions have barely been reported.

In this study, a series of metal oxide (M-Al-O, M = Mg, Ca, and Sr) precursors were synthesized by a hydrothermal coprecipitation route as a function of hydrothermal temperature. The effect of different divalent metal ions and synthetic temperature on the structural morphology, and thermal properties of those IIA-Al LDH systems were systematically studied to correlate with CO₂ adsorption capacity after calcinations at different temperatures. The results demonstrate that the metal oxides with different divalent metal ions display different characteristic adsorption behaviour and optimal operation temperature range for CO₂ capture/separation and hydrogen gas production for power plants at a variety of high temperature range.



A.1-2 Experiments

A.1-2.1 Preparation of metal oxides

Various metal oxide precursors were synthesized using the hydrothermal coprecipitation method (denoted as M-Al-O; M = Mg, Ca, and Sr). Mg(NO₃)₂·6H₂O (Fluka), Ca(NO₃)₂·4H₂O (Riedel-de Haën), and Sr(NO₃)₂ (Riedel-de Haën) were used as a source of divalent cation, respectively, and Al(NO₃)₃·9H₂O (Sigma-Aldrich), Na₂CO₃ (TEDIA), and NaOH (Showa) were separately used as trivalent cation, interlayer anion, and precipitation agent. Typically, 0.075 mol of divalent cation (M(NO₃)₂) and 0.025 mol of trivalent cation (Al(NO₃)₃) at molar ratio of 3:1 were dissolved separately in 75 ml deionized water. 0.16 mol of NaOH and 0.01 mol of Na₂CO₃ were dissolved in 100 ml deionized water and then added quickly to M²⁺/Al³⁺ solutions to form M-Al-O precursor by coprecipitation method. Then, the precipitated precursor was put into an autoclave for thermal reaction in an oven at 25 °C (RT), 80 °C, and 125 °C for 24 h. The white slurry was separated by centrifugation and washed 3 times with deionized water to remove unreacted ionic sources, and then dried

at 60 °C in an oven to give raw powder of M-Al-O precursor (denoted as M-Al-O-RT, M-Al-O-80, M-Al-O-125). Finally, these M-Al-O-RT, M-Al-O-80, and M-Al-O-125 samples were calcined at different temperatures (500 °C-930 °C) to form the metal oxides.

A.1-2.2 Characterization and CO₂ sorption analysis

The resulting powders were characterized using powder X-ray diffraction (PXRD) measurements (MAC Science MXP18AHF XRD, with Cu K α radiation source, $\lambda = 1.5418$ Å). The crystalline morphology and particle size of those samples were observed by field emission scanning electron microscopy (FESEM, JEOL-6700).

Thermogravimetric analysis (TGA, TA Instrument Q500) was used to investigate the CO₂ adsorption properties of the metal oxides. The heating rate was 10 °C min⁻¹, and the metal oxide sample was maintained at a high temperature for 30 min under nitrogen and then carbonated by pure CO₂ gas with a flow rate of 60 mL min⁻¹ (CO₂ partial pressure at 40 kPa) at different temperatures (200-850 °C) for 2 h. The CO₂ adsorption capacity (C_{ads}) of the calcined metal oxides was defined according to the following equation:

$$C_{\text{ads}} (\text{g-CO}_2/\text{g-calcined sample}) = \text{weight of CO}_2 / \text{weight of calcined sample}$$

Moreover, the CO₂ carbonation/calcination cycles of the metal oxides were collected by TGA (adsorption at 200 °C (Mg-Al-O), 700 °C (Ca-Al-O), and 850 °C (Sr-Al-O)) for 25 min in pure CO₂ gas and then calcination at another 8 min in N₂ gas with a flow rate of 60 mL min⁻¹). The cycles were repeated 20 times.

A.1-3 Results and discussion

A.1-3.1 Structure Characterization

The powder X-ray diffraction (PXRD) patterns of metal oxide precursors (M-Al-O, M = Mg, Ca, and Sr) synthesized by hydrothermal coprecipitation treatment at 25 °C (RT), 80 °C, and 125 °C were shown in Figure A.1.1 Mg-Al-O precursor samples were indexed as the

structure of hydrotalcite (HT)-like phase (JCPDS-14-191) with the diffraction peaks of strong reflections corresponding to basal $00l$ planes of (003), (006), and (009). When hydrothermal temperature increased from 25°C to 125°C , Figure A.1.1(a) shows that the relative intensity of the (003) peak became sharper, implying good crystalline structure and large particle size of the Mg-Al LDH synthesized by the hydrothermal method at higher temperature. For Ca-Al-O precursor samples, the PXRD patterns in Figure A.1.1(b) also displayed typical hydrotalcite (HT)-like phases with diffraction peaks at $2\theta = 10.5^{\circ}$ and 21.1° which correspond to the basal planes of (003) and (006), respectively. Although a minor CaCO_3 phase was observed, this also indicated well-developed crystalline layered structure with a rhombohedral symmetry. The formation of a CaCO_3 phase in the Ca-Al-O precursor is presumably attributed to the greater insolubility of CaCO_3 and the incompatibility of the ionic size of Al^{3+} and Ca^{2+} (0.62 \AA versus 1.06 \AA). Increasing hydrothermal temperature, it was found that the peak intensity of diffraction peaks of (003) and (006) planes for the Ca-Al-O-80 and Ca-Al-O-125 samples became stronger than the Ca-Al-O-RT sample; therefore, it implied that hydrothermal treatment at higher temperature for Ca-Al-O precursor samples could enhance the crystallization of layered double hydroxide particles. However, as compared to the Ca-Al-O-80 sample, two sets of diffraction peaks at $2\theta = 11.5^{\circ}$ and 23.3° can be clearly observed from the Ca-Al-O-125 precursor sample, which may suggest the present of two kinds of HT-like phases simultaneously. However, the phenomenon did not appear in the above-mentioned Mg-Al LDH, which was attributed to smaller ionic size of Mg^{2+} ions. Because the ionic size of Ca^{2+} ions is slightly larger than the octahedral site in crystalline structure of primary particles (Ca-Al LDH), it may become unstable at high temperature; therefore, the Ca^{2+} ions could diffuse easily to form a secondary particle on the surface of the primary particle ^[8]. The PXRD patterns of Sr-Al-O precursor samples in Figure A.1.1(c) showed that the crystalline phases of HT-like compounds was not observed but many crystalline compounds

with explicit diffraction peaks have been identified such as SrO, Sr(OH)₂, and SrCO₃. It was probably due to the large ionic radius of Sr²⁺ ions (1.27 Å), giving the Sr²⁺ hardly incorporated into the octahedral site of HT-like structure.

The SEM images of metal oxide precursors with various synthesis temperatures are shown in Figure A.1.2. The morphologies of the Mg-Al-O-RT and Mg-Al-O-80 samples displayed wormlike shape with the particle size distribution in the range of ca. 20-50 nm. The Mg-Al-O-125 sample showed an oblate shape with the lateral size of ca. 0.1-0.5 μm and the thickness of ca. 20-30 nm. However, the particle size becomes bigger with increasing hydrothermal temperature, which was well consistent with the results of PXRD patterns. It is thought that the particles may undergo anisotropic crystal growth or intergrowth into larger particles by the aggregation of raw particles upon aging temperature. Moreover, the highly-crystalline particles were also observed for Ca-Al-O precursor prepared at higher temperature. The Ca-Al-O-125 sample formed the large sheet-like plates with the lateral size of ca. 8-20 μm and the thickness of ca. 80-150 nm. In contrast, for the Sr-Al-O precursor prepared at different hydrothermal temperatures, it was found that the morphologies of the samples changed from the aggregative nanoparticles to uniform crystalline nanorod-like shape with length of 50-100 nm and width of ~20 nm upon increasing reaction temperature.

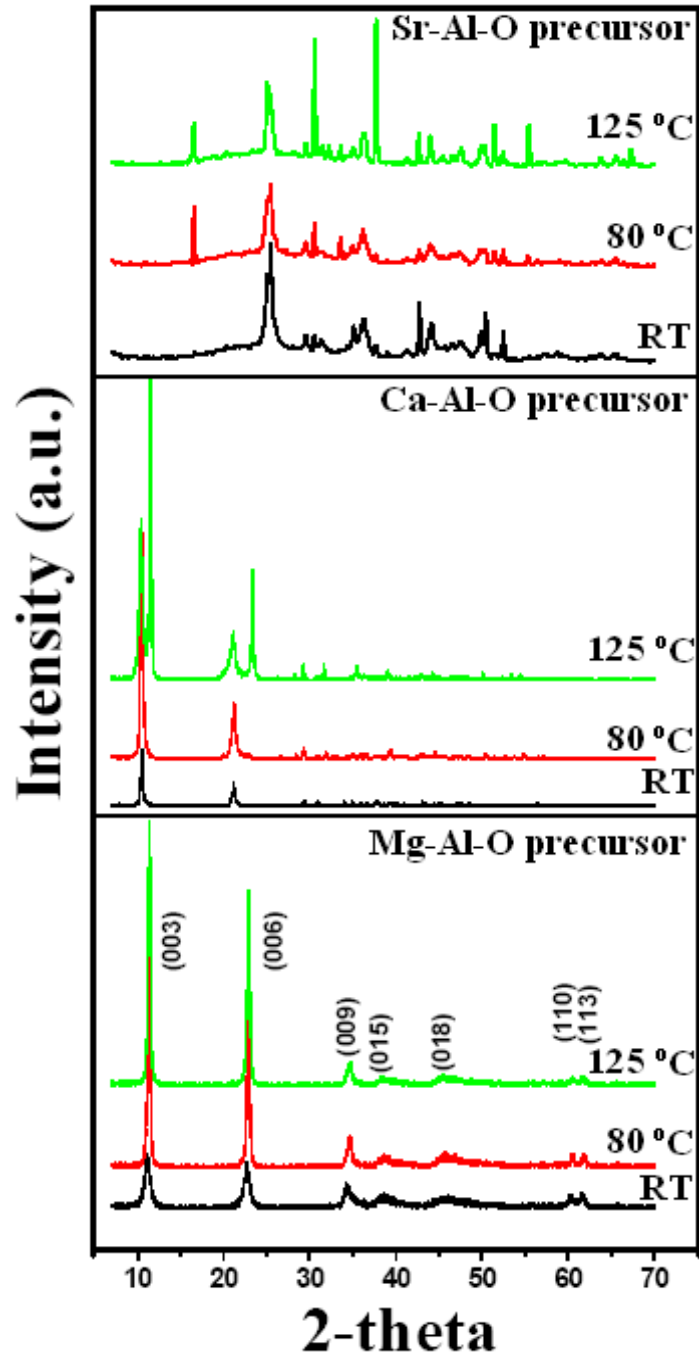


Figure A. 1. 1 The PXRD patterns of metal oxide (M-Al-O, M = Mg, Ca, and Sr) precursors by hydrothermal coprecipitation method at a various temperature.

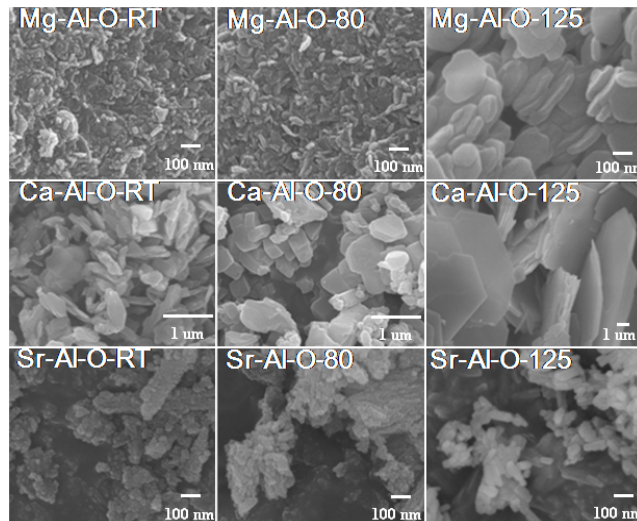


Figure A. 1. 2 The SEM images of metal oxide (M-Al-O, M = Mg, Ca, and Sr) precursors by hydrothermal coprecipitation method at a various temperature.

The PXRD patterns of the calcined metal oxide M-Al-O (M=Mg, Ca, and Sr) precursor prepared by hydrothermal temperature at 80 °C were shown in Figure A.1.3. When the Mg-Al-O with hydrocalcite structure was calcined at 600 °C, MgO, MgAl₂O₄, and γ -Al₂O₃ phases can be seen in the Mg-Al-O sample, which is similar to the report of a previous literature [9]. For the Ca-Al-O precursor calcined at 600 °C, the PXRD pattern of the calcined Ca-Al-O sample displayed the crystalline structures of Ca(OH)₂ (JCPDS No. 44-1481), CaCO₃ (JCPDS No. 23-1037), and Ca₁₂Al₂₂O₃₃ (JCPDS No. 09-0413). On the other hand, only SrCO₃ (JCPDS No. 05-0418) crystalline phase was indexed for the calcined Sr-Al-O. At a higher temperature above 850 °C, the SrCO₃ crystallite in Al₂O₃ matrix would be probably decomposed to react with Al₂O₃ to form metal oxide (Sr-Al-O). Therefore, this reaction of carbonation--calcination is very difficult to occur below 850 °C [10].

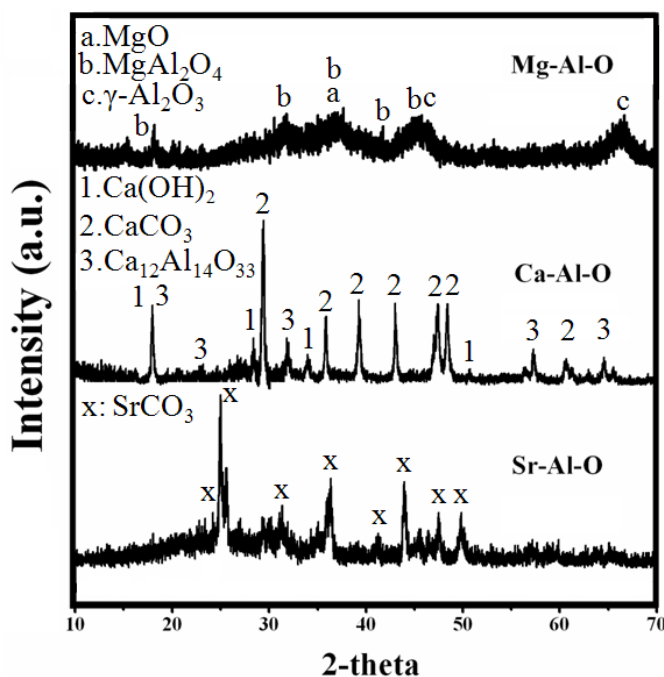


Figure A. 1. 3 The PXRD patterns of metal oxides (M-Al-O, M = Mg, Ca, and Sr) prepared by hydrothermal temperature at 80 °C, and calcined at 600 °C.

A.1-3.2 CO₂ adsorption property of metal oxides

The calcined metal oxides (M-Al-O, M=Mg, Ca, and Sr) could be used as CO₂ sorbents and their CO₂ adsorption capacity with hydrothermal treatment at RT, 25 °C, and 125 °C was showed in Figure A.1.4. It was found that the maximum CO₂ adsorption capacity appears in the M-Al-O samples prepared at room temperature, meaning with increasing hydrothermal temperature, CO₂ adsorption capacity decreased. The main reason is that the particle size of the metal oxide compounds varies with different treatment temperatures, which modify the reaction activity and active sites of the CO₂ adsorption. Moreover, it was also found that the CO₂ adsorption capacity of the metal oxides is not only dominated by the hydrothermal temperature, but also by the adsorption temperature as shown in Figure A.1.5.

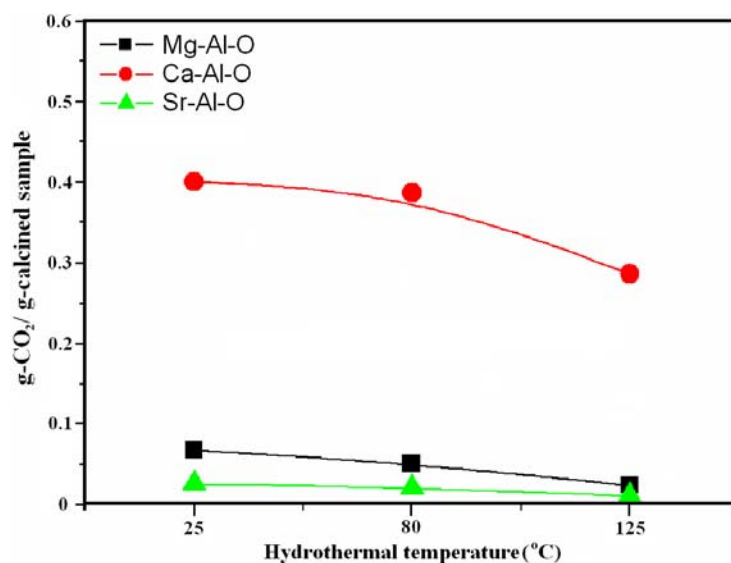


Figure A. 1. 4 CO₂ adsorption capacity of metal oxides (M-Al-O, M=Mg, Ca, and Sr) prepared by hydrothermal treatment at RT, 80 °C, and 125 °C, and calcined/adsorbed at 600°C.

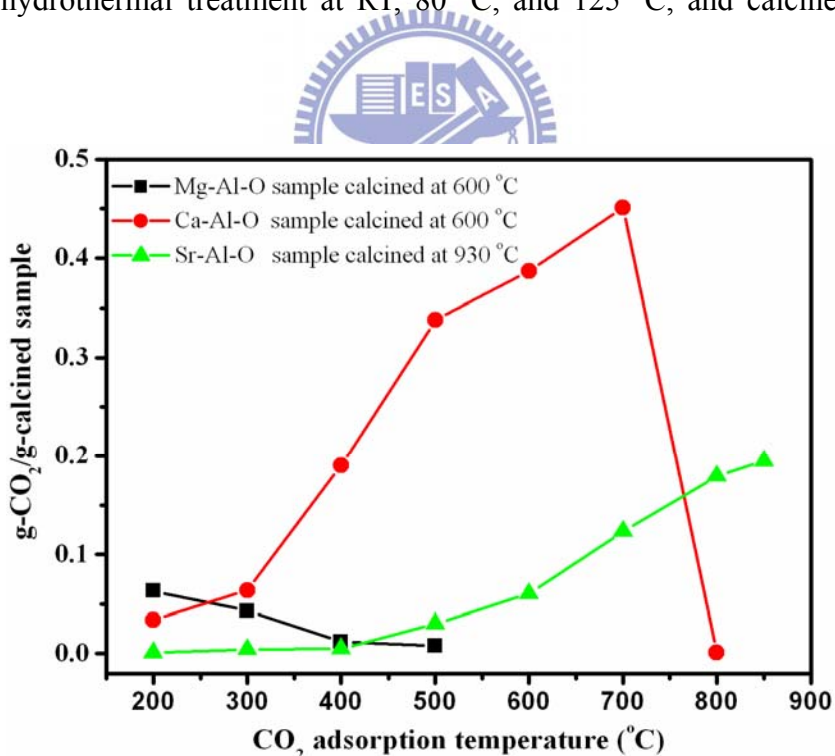


Figure A. 1. 5 CO₂ adsorption capacity of calcined metal oxides (M-Al-O, M=Mg, Ca, and Sr) prepared by hydrothermal temperature at 80 °C, and adsorbed at 200-850 °C.

The Mg-Al-O sorbent exhibited CO₂ adsorption capacity at the carbonation temperature in the range of 200 °C-500 °C, and the largest adsorption capacity (~0.06 g CO₂/g-sorbent) occurred at 200 °C, above that its capacity was decreased because MgCO₃ is probably calcined at high temperature. On the other hand, when the Ca-Al-O sorbent was

carbonated by CO₂ at 200 °C-800 °C, the obvious adsorption behavior of the sorbent started to appear at adsorption temperature of 300 °C and increased up to 700 °C where a maxima adsorption capacity (~0.45 g CO₂/g-sorbent) was detected. However, the adsorption capacity rapidly dropped to almost zero at 800 °C because of the decarbonation of CaCO₃ at higher temperature. In contrast, the Sr-Al-O sorbent clearly exhibited the adsorption behavior at 500°C-850°C, and its best adsorption capacity (~0.2 g CO₂/g-sorbent) was higher than that of Ca-Al-O sorbent at over 800 °C. Although Tanabe et al. studied the effect of CO₂ adsorption on the catalytic activity of alkaline earth metal oxides and revealed that the number of active (basic) sites follows the order MgO>CaO>SrO^[11], the CO₂ adsorption capability of metal oxides in the present study displayed in the order Mg-Al-O >Ca-Al-O>Sr-Al-O for adsorption temperature (200 °C), Ca-Al-O>Mg-Al-O>Sr-Al-O for 300 °C, Ca-Al-O>Sr-Al-O>Mg-Al-O for 500 °C, and Sr-Al-O>Ca-Al-O>Mg-Al-O for 800 °C. Due to these sorbents exhibited different carbonations at high temperature, those results of CO₂ adsorption suggested that metal oxides (Mg-Al-O, Ca-Al-O, and Sr-Al-O) may be selected and used as various CO₂ sorbents for low temperature (<200°C), middle temperature (300 °C-700 °C), and high temperature (>800 °C), respectively.

The high-performance CO₂ sorbents with longer cyclic life of CO₂ play an important role in the industrial application of CO₂ capture. Figure A.1.6 shows the capture capacity of three CO₂ sorbents as a function of cycle number onto metal oxides at 200 °C (Mg-Al-O), 700 °C (Ca-Al-O), and 850°C (Sr-Al-O). The results of Mg-Al-O and Ca-Al-O samples showed a best stable retention of cyclic life up to ~94% after 20 cycles. On the other hand, the ~6% of irreversible adsorption in the total 20 cycles is attributed to partial sorbent active decay because of the partial sintering between the MgO/MgCO₃ or CaO/CaCO₃ in the sorbents and strong chemical interactions between the sorbent and the CO₂ molecules^[12]. Moreover, MgAl₂O₄ or Ca₁₂Al₁₄O₃₃ crystallites from the PXRD results could play an important role in providing a stable support to inhibit the deactivation of MgO or CaO and

strengthen the adsorption performance. Additionally, according to the results of PXRD analysis, the Sr-Al-O sample composed of amorphous Al_2O_3 and crystalline SrCO_3 can be transformed into active SrO after calcined at $850\text{ }^\circ\text{C}$ [13]. The cyclic performance showed a stable cyclic life before 8 cycles but the cycle decay to the retention of 80% occurred after 20 cycles because multiple carbonation/calcination cycles at higher temperature ($850\text{ }^\circ\text{C}$ to $930\text{ }^\circ\text{C}$) easily caused the aggregation of active SrO particle. Therefore, depending on the CO_2 adsorption mechanism, metal oxides exhibit different adsorptive capacities of CO_2 , and optimal operation temperature range for CO_2 capture/separation and hydrogen gas production for power plants, which can be modified by controlling its composition, structure and particle size in vehicles.

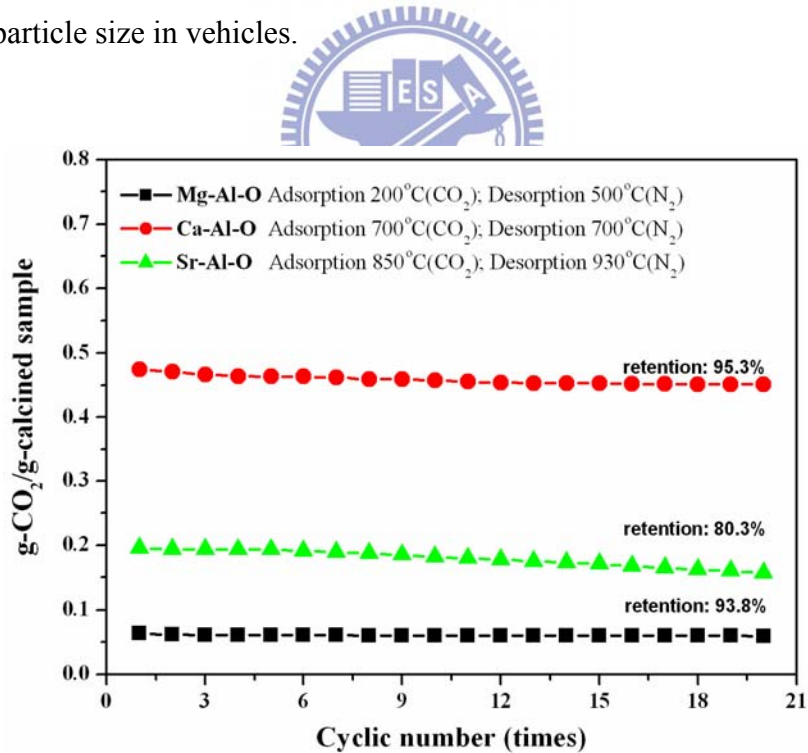


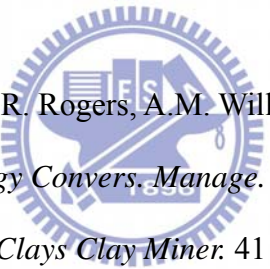
Figure A. 1. 6 CO_2 carbonation/calcination cycles of calcined metal oxides (M-Al-O, M=Mg, Ca, and Sr) and adsorbed/desorbed at $200\text{ }^\circ\text{C}/500\text{ }^\circ\text{C}$, $700\text{ }^\circ\text{C}/700\text{ }^\circ\text{C}$, and $850\text{ }^\circ\text{C}/930\text{ }^\circ\text{C}$, respectively.

A.1-4 Conclusion

The metal oxides (M-Al-O) of alkaline earth metal (M=Mg, Ca, and Sr) were investigated on their crystalline structure as a function of hydrothermal temperature and

chemical composition. Depending on the CO₂ adsorption mechanism, the material exhibits different CO₂ adsorption behavior by controlling the structure, composition, particle size and calcinations temperature. The CO₂ adsorption and regeneration of 80%-94% of its initial CO₂ adsorption capacity can be achieved after 20 cycles of carbonation and calcination. Such properties clearly reflect the potential of metal oxides as strong candidates for CO₂ adsorption and hydrogen gas production. Additionally, for the sorption-enhanced reaction process (SERP), the Ca-based metal oxide is attractive as a sorbent for CO₂ capture at high temperature (600-700 °C).

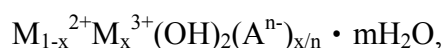
A.1-5 References

- 
- [1] T.D. Burchell, P.R. Judkins, M.R. Rogers, A.M. Williams, *Carbon* 35 (1997) 1279.
- [2] Z. Yong, A.E. Rodrigues, *Energy Convers. Manage.* 43 (2002) 1865.
- [3] G. Mao, M. Tsuji, Y. Tamaura, *Clays Clay Miner.* 41 (1993) 731.
- [4] Z. Yong, V. Mata, A.E. Rodrigues, *Ind. Eng. Chem. Res.* 40 (2001) 204.
- [5] J.L. Soares, G.L. Casarin, H.J. Jose, R. Moreira, A.E. Rodrigues, *Adsorption* 11 (2005) 237.
- [6] N.D. Hutson, S.A. Speakman, E.A. Payzant, *Chem. Mater.* 16 (2004) 4135.
- [7] W. Yang, Y. Kim, P.K.T. Liu, M. Sahimi, T.T. Tsotsis, *Chem. Eng. Sci.* 57 (2002) 2945.
- [8] Y. Zhao, F. Li, R. Zhang, D.G. Evans, X. Duan, *Chem. Mater.* 14 (2002) 4286.
- [9] J. Shen, M. Tu, C. Hu, *J. Solid State Chem.* 137 (1998) 295.
- [10] Y.L. Chang, H.I. Hsiang, *J. Am. Ceram. Soc.* 90 (2007) 2759.
- [11] K. Tanabe, Y. Fukuda, *React. Kinet. Catal. Lett.* 1 (1974) 21.
- [12] J. Wang, E.J. Anthony, *Ind. Eng. Chem. Res.* 44 (2005) 627.
- [13] R.L. Frost, W.N. Martens, M.C. Hales, *J. Therm. Anal. Calorim.* 95 (2009) 999.

Appendix-2

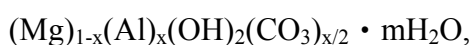
Crystal Structure of Layered Double Hydroxides (LDHs)

Layered double hydroxides (LDHs), also called hydrotalcites (HTCs) or Feitknecht compounds, belong to the family of anionic clays. Their general formula is



where M^{2+} and M^{3+} are divalent and trivalent metal ions respectively, and A^{n-} is an anion.

The value of x should be in the range 0.2-0.33. The metal ions and anions appear in different layers. The metal ion host layer has the brucite structure of $\text{Mg}(\text{OH})_2$, in which the metal ions are octahedrally coordinated by OH^- ions. Part of the divalent metal ions is replaced by trivalent ions, leaving the brucite structure intact. Consequently, this layer has a net positive charge which is compensated by the charge of the anion layer. The empty sites of the anion layer are filled with water molecules. The most common LDH (as shown in Figure A.2.1) is



occurring in nature as $\text{Mg}_{0.75}\text{Al}_{0.25}(\text{OH})_2(\text{CO}_3)_{0.125} \cdot 0.5\text{H}_2\text{O}$ (the mineral ‘hydrotalcite’) with which the above class of anionic clays is isostructural.

LDHs can be easily synthesized by coprecipitation from a solution of soluble salts containing the metal ions, usually at slightly elevated temperature and constant pH^[1]. By slow addition of a carbonate salt, a precipitate is formed. The precipitate is separated by filtration and dried. Thanks to the structure of LDH, the metals are well mixed and dispersed and thus, LDHs are ideal candidate catalyst precursors. When the LDH is calcined in air or N_2 , first it loses its interlayer water up to approximately 200 °C. In the range 200-400 °C, dehydroxylation and decarbonisation take place and the specific surface area increases strongly. The suitability of LDH as high temperature CO_2 sorbent stems from the plurality of strong basic sites at the surface this structure offers, which favours the

adsorption of the acidic CO_2 according to the Lewis acid-base theory [2]. When no further heating occurs, the thus obtained mixture of metal oxides can be transformed back into the original LDH structure by contacting it with a carbonate solution. This is the so-called memory-effect of LDHs.

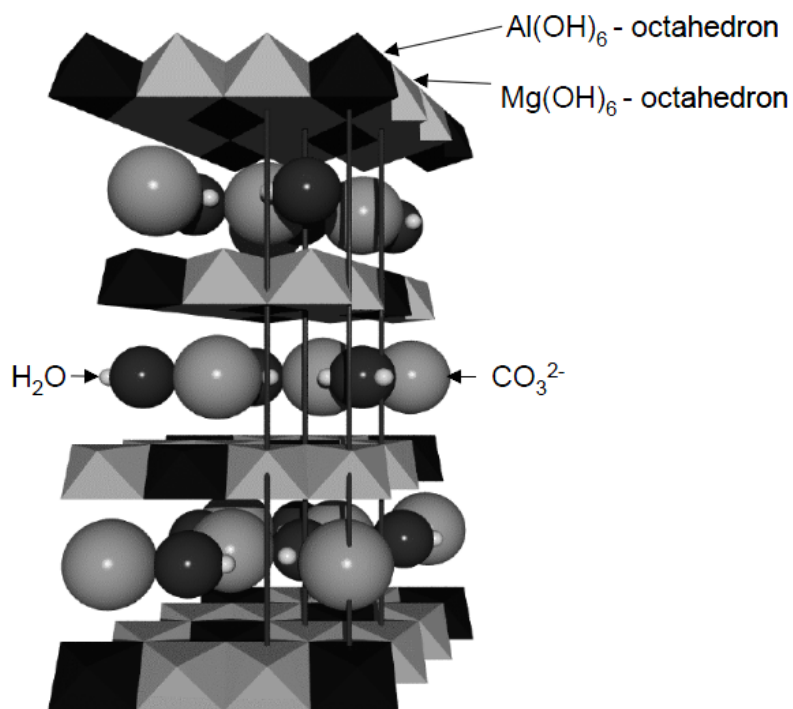


Figure A. 2. 1 Crystal structure of Mg-Al-CO₃-LDHs.

A.2 References

- [1] F. Cavani, F. Trifirò, A. Vaccari, *Cat. Today* 11 (1991) 173.
- [2] J.I. Di Cosimo, V.K. Diez, M. Xu, E. Iglesia, C.R. Apesteguia, *J. Cat.* 178 (1998) 499.

Appendix-3

Crystal Structure of Mayenite $\text{Ca}_{12}\text{Al}_{14}\text{O}_{33}$

$\text{Ca}_{12}\text{Al}_{14}\text{O}_{33}$ ($12\text{CaO}\cdot 7\text{Al}_2\text{O}_3$; C12A7) is a transparent insulator with a wide band gap of ~ 7 eV. The $\text{Ca}_{12}\text{Al}_{14}\text{O}_{33}$ cubic unit cell includes two chemical formulas and can be expressed as $[\text{Ca}_{24}\text{Al}_{28}\text{O}_{64}]^{4+}(2\text{O}^{2-})$ [1]. The $[\text{Ca}_{24}\text{Al}_{28}\text{O}_{64}]^{4+}$ component represents a lattice framework, involving 12 cages with an inner space, ~ 0.4 nm in diameter (Figure A.3.1). Each cage is connected directly to 12 other cages by sharing an oxide monolayer wall. The 2O^{2-} component is an extra framework of oxygen ions (hereinafter referred to as “free oxygen”) that occupy two of 12 cages to maintain charge neutrality of the crystal. It has been found that electrons can be substituted, partially, or entirely for free oxygen to form $[\text{Ca}_{24}\text{Al}_{28}\text{O}_{64}]^{4+}(\text{O}^{2-})_{2-x}(\text{e}^-)_{2x}$, ($0 \leq x \leq 2$) [2]. This class of materials are referred to as inorganic electrides, in which electrons act as anions engaged in framework cations [3]. $\text{Ca}_{12}\text{Al}_{14}\text{O}_{33}$ is the first room-temperature stable electride and has attracted much attention owing to its peculiar electronic properties originating from a unique nanoporous structure [4].

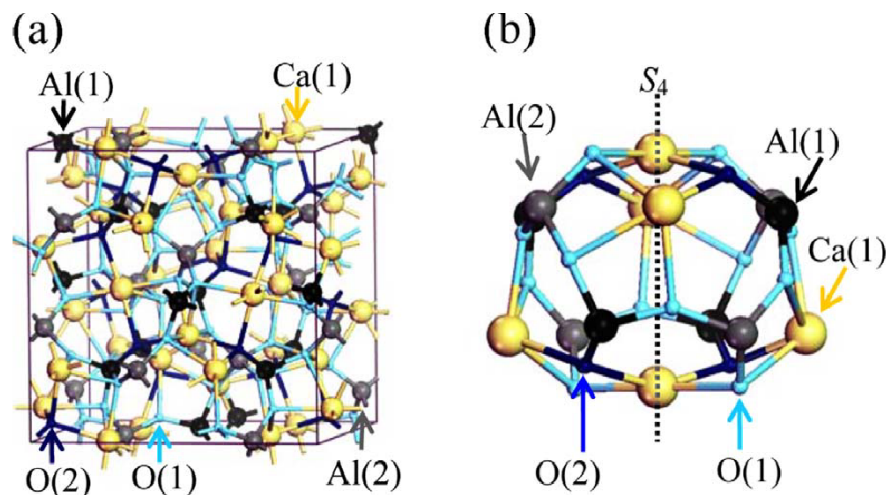
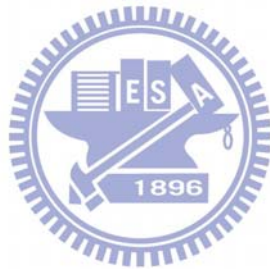


Figure A.3. 1 Crystal structure of mayenite $\text{Ca}_{12}\text{Al}_{14}\text{O}_{33}$ (Space group: $I-43d$). (a) Structure of the cage framework. Free oxygen in the cages is neglected for simplicity. The box shows a cubic unit cell containing 12 cages. (b) Structure of an empty cage of $\text{Ca}_{12}\text{Al}_{14}\text{O}_{33}$. The S_4 axis passes through two polar Ca ions and the cage center.

A.3 References

- [1] H. Bartl, T. Scheller, *Neues Jahrb. Mineral., Monatsh.* **35** (1970) 547.
- [2] S. Matsuishi, Y. Toda, M. Miyakawa, K. Hayashi, T. Kamiya, M. Hirano, I. Tanaka, H. Hosono, *Science* 301 (**2003**) 626.
- [3] J. L. Dye, *Science* 301(**2003**) 607.
- [4] H. Hosono, K. Hayashi, M. Hirano, *J. Mater. Sci.* 42 (**2007**) 187.



Curriculum Vitae

Chinese name: 張彥博

English name: Yen-Po Chang (Y.P. Chang)

Advisor: Prof. San-Yuan Chen

Department of Materials Science and Engineering

National Chiao Tung University, 1001 Ta Hsinchu, Taiwan 300

Email: ypchang1021@gmail.com

2007-2012 Ph.D. National Chiao Tung University, Hsinchu, Taiwan

Major: Department of Materials Science and Engineering

Prof.: San-Yuan Chen

Research Topic: Mesoporous Materials on CO₂ Capture and Drug Delivery.

2006-2007 Research Assistant, National Tsing Hua University, Hsinchu, Taiwan

Department: Department of Chemistry

Research Topic: Supercritical Extraction and CO₂ Sorbents

2005-2006 Associate Engineer, Industrial Technology Research Institute, Hsinchu, Taiwan

Department: Electronics & OptoElectro Labs

Research Topic: Preparation and Analysis of TEM specimen, Failure Analysis of PCB

2003-2005 M.S. National Tsing Hua University, Hsinchu, Taiwan

Major: Department of Chemistry

Prof.: Kuei-Jung Chao

Research Topic: Nanostructured Metal Incorporated Mesoporous Silica: Synthesis and Characterization.

1999-2003 B. S. Chung Yuan Christian University, Chung Li, Taiwan

Major: Department of Chemistry

Prof.: Jui-Ming Yeh

Research Topic: Synthesis and Characterization of Polymer-Clay nanocomposite materials.

Publications

SCI Journals:

1. **Y.P. Chang**, P.H. Chang; Y.T. Lee, S.Y. Chen*; C.T. Yu, Y.P. Chyou, “Structure Identification and CO₂ Adsorption Behavior of Hybrid Metal Oxides by Hydrothermal Coprecipitation Route”, (2012, Submitted to Journal of Alloys and Compounds)
2. **Y.P. Chang**, Y.C. Chen, P.H. Chang, S.Y. Chen*, “Synthesis, characterization, and CO₂ adsorptive behavior of order mesoporous AlOOH-Supported Ca-Al-LDHs”, Chemsuschem, 2012 to be published, DOI: 10.1002/cssc.201100617. (IF 2010 = 6.325, JR = 10%, 2010)
3. **Y.P. Chang**, K.H. Liu, C.S. Chao, S.Y. Chen* and D.M. Liu*, “Synthesis and characterization of mesoporous Gd₂O₃ nanotube and its use as a drug-carrying vehicle”, Acta Biomaterialia, 2010, 6, 3713. (IF 2010 = 4.824, JR = 4%, 2010)
4. C.S. Chao, K.H. Liu, W.L. Tung, S.Y. Chen, D.M. Liu* and **Y.P. Chang***, “Bioactive TiO₂ ultrathin film with worm-like mesoporosity for controlled drug delivery”, Microporous and Mesoporous Materials 2012, 152, 58. (IF 2010 = 3.22, JR = 7%, 2010)
5. P.H. Chang, **Y.P. Chang**, S.Y. Chen, C.T. Yu, and Y.P. Chyou, “Synthesis, characterization and CO₂ capture of in situ self-assembly nano-scale layered double hydroxide particles”, (2012, Submitted to Journal of Alloys and Compounds)
6. P.H. Chang, **Y.P. Chang**, S.Y. Chen*, C.T. Yu and Y.P. Chyou, “Ca-Rich Ca-Al-Oxide, high-temperature-stable sorbents prepared from hydrotalcite precursors: synthesis, characterization, and CO₂ capture capacity”, Chemsuschem, 2011, 4, 1844. (IF 2010 = 6.325, JR = 10%, 2010)
7. C.H. Wu, **Y.P. Chang**, S.Y. Chen*, D.M. Liu, C.T. Yu, B.L. Pen, “Characterization and structure evolution of Ca-Al-CO₃ hydrotalcite film for high temperature CO₂ adsorption”,

- Journal of Nanoscience and Nanotechnology, **2010**, 10, 4716. (IF 2010 = 1.352, JR = 42%, 2010)
8. K.C. Hsu, **Y.P. Chang** and K.J. Chao*, “The characterization of supported mesoporous thin films-Supercritical fluid extraction of surfactant templates”, Studies in Surface Science and Catalysis **2007**, 170, 1748. (IF 2005 = 0.307)
9. K.J. Chao*, **Y.P. Chang**, Y.C. Chen, A.S. Lo and T.H. Phan “Morphology of nanostructured platinum in mesoporous materials - Effect of solvent and intrachannel surface”, Journal of Physical Chemistry B **2006**, 110, 1638 (IF 2010 = 3.603, JR = 25%)
10. P.H. Liu, **Y.P. Chang**, T.H. Phan and K.J. Chao*, “The morphology and size of nanostructured Au in Au/SBA-15 affected by preparation conditions”, Materials Science & Engineering C, **2006**, 26, 1017 (IF 2010 = 2.178, JR = 60%)
11. H.S. Sheu, P.H. Liu, H.L. Cheng, K.J. Chao* and **Y.P. Chang**, “Structural characterization of porous film materials and the supported metal catalysts by synchrotron powder X-ray diffraction”, Catalysis Today, **2004**, 97, 55 (IF 2010 = 2.993, JR = 8%)
12. J.M. Yeh*, S.J. Liou, C.G. Lin and **Y.P. Chang**, Y.H. Yu, and C.F. Cheng, “Effective Enhancement of Anticorrosive Properties of Polystyrene by Polystyrene-Clay Nanocomposite Materials”, Journal of Applied Polymer Science, **2004**, 92, 1970 (IF 2010 = 1.24, JR = 47%)
13. Y.H. Yu, J.M. Yeh*, S.J. Liou and **Y.P. Chang**, “Organo-soluble polyimide (TBAPP-OPDA)/clay nanocomposite materials with advanced anticorrosive properties prepared from solution dispersion technique”, Acta Materialia **2004**, 52, 475 (IF 2010 = 3.791, JR = 1%,)

Conference Journals:

1. **Y.P. Chang**, P.H. Chang, T.J. Lee, Y.T. Lee and S.Y. Chen*, “Microwave Assisted In Situ Synthesis of Mesoporous $12\text{CaO} \cdot 7\text{Al}_2\text{O}_3$ Nanohybrids”, 19th ISMANAM Conference, 2012, Russia.
2. **Y.P. Chang**, P.H. Chang; Y.T. Lee, S.Y. Chen*; C.T. Yu, Y.P. Chyou, “Structure Identification and CO_2 Adsorption Behavior of Hybrid Metal Oxides by Hydrothermal Coprecipitation Route”, 19th ISMANAM Conference, 2012, Russia.
3. **Y.P. Chang**, C.S. Chao, D.M. Liu and S.Y. Chen*, “Sol-gel derived multi-functional mesoporous TiO_2 bioactive coating”, 1st Nano Today Conference, **2009**, Singapore.
4. **Y.P. Chang**, P.H. Chang, S.Y. Chen*, D.M. Liu, C.T. Yu, and Y.P. Chyou, “Structural characterization and CO_2 sorption behavior of IIA-based layered double hydroxide membranes”, TACT International Thin Films Conference, 2009, Taiwan.
5. **Y.P. Chang**, P.H. Liu, A.S. Lo and K.J. Chao*, “Incorporated Pt nanostructure on mesoporous silica: synthesis and characterization”, Chemical Society Located in Taipei Annual meeting **2004**, National Chung Hsing University, Taiwan.
6. P.H. Chang, **Y.P. Chang**, S.Y. Chen*, C.T. Yu, and Y.P. Chyou, “Synthesis, characterization and CO_2 capture of in situ self-assembly nano-scale layered double hydroxide particles”, 19th ISMANAM Conference, 2012, Russia.
7. C.H. Wu, **Y.P. Chang**, S.Y. Chen*, D.M. Liu, C.T. Yu, and B.L. Pen, “Characterization and structure evolution of Ca-Al- CO_3 hydrotalcite film for high temperature CO_2 adsorption”, 4th International Conference on Technological Advances of Thin Films and Surface Coating, **2008**, Singapore.
8. K.C. Hsu, **Y.P. Chang**, K.J. Chao*, “The characterization of supported mesoporous thin films-supercritical fluid extraction of surfactant templates”, Proceedings of the 15th International Zeolite Conference, **2007**, Beijing, P. R. China.

9. K.C. Hsu, **Y.P. Chang**, S.F. Chen and K.J. Chao*, “The Formation of Supported Mesoporous Film as Function of Preparation Conditions by Synchrotron X-ray Diffraction and Reflectivity”, Chemical Society Located in Taipei Annual meeting **2006**, Tamkang University, Taiwan.
10. L.C. Wang, C.Y. Huang, **Y.P. Chang** and K.J. Chao*, “Coassembly synthesis of mesoporous silica materials containing Pd nanoparticles”, Tokyo conference on Advanced Catalytic Science and Technology, TOCAT5 **2006**, Japan.
11. L.C. Wang, C.Y. Huang, **Y.P. Chang**, A.S. Lo and K.J. Chao*, “Mesoporous silica materials containing metal nanostructures, NTHU-KAIST **2006** Junior Chemists Workshop, National Tsing Hus University, Taiwan.
12. P.H. Liu, **Y.P. Chang** and K.J. Chao*, “The morphology and size of nanostructure Au and Pt in Au/SBA-15 and Pt/MCM-48 affected by preparation condition”, E-MRS **2005** Spring Meeting, France.
13. K.J. Chao*, **Y.P. Chang**, Y.C. Chen and T.H. Phan, “Effects of solvent and intrachannel surface properties on morphology of nanostructured Pt in mesoporous materials”, Division of Colloid and Surface Chemistry for the 230th ACS National Meeting **2005**, USA.
14. H.S. Sheu, P.H. Liu, H.L. Cheng, K.J. Chao*, **Y.P. Chang**, “Structural characterization of porous film materials and the supported metal catalysts by synchrotron powder X-ray diffraction”, IPCAT-3/TSCRE-21, **2003**, Taiwan.

Patents:

1. 陳三元, 張博學, 張彥博, 陳俞君, “多孔鈣鋁氧化物結構的製造方法, 中華民國專利 (申請中), 2011
2. 梁明侃, 蔡宗甫, 張彥博, “穿透式電子顯微鏡之電子元件結構的分析方法”, 中華民國專利 (證書號:I315397), 2009